ISSN number 0971 - 9709

The Journal of Indian Geophysical Union

VOLUME 23, ISSUE 3 I MAY 2019

AN OPEN ACCESS BIMONTHLY JOURNAL OF IGU

EDITORIAL OFFICE

Indian Geophysical Union, NGRI Campus, Uppal Road, Hyderabad- 500 007
Telephone: +91 -40-27012799; 27012734; Telefax:+91-04-27171564
E. mail: jigu1963@gmail.com, website: www.j-igu.in

The Open Access Journal with six issues in a year publishes articles covering
Solid Earth Geosciences; Marine Geosciences; and Atmospheric, Space and Planetary Sciences.

Annual Subscription

Individual ₹ 1000 per issue and Institutional ₹ 5000 for six issues

Payments should be sent by DD drawn in favour of "The Treasurer, Indian Geophysical Union", payable at Hyderabad, Money Transfer/NEFT/RTGS (Inter-Bank Transfer), Treasurer, Indian Geophysical Union, State Bank of India, Habsiguda Branch, Habsiguda, Uppal Road, Hyderabad- 500 007
A/C: 52191021424, IFSC Code: SBIN0020087, MICR Code: 500002318, SWIFT Code: SBININBBHO9.

For correspondence, please contact, Hon. Secretary, Indian Geophysical Union, NGRI Campus, Uppal Road, Hyderabad - 500 007, India; Email: igu123@gmail.com; Ph: 040 27012799, 272012734

ISSN: 0257-7968 (Clarivate Analytics)
ISSN: 0971-9709 (NISCAIR)
Approved as bimonthly ESCI journal by Clarivate Analytics
Cited in Indian Citation Index (ICI), New Delhi
Evaluated by NISCAIR, New Delhi

CONTENTS

Research Articles

J. Ind. Geophys. Union (May 2019)
v.23, no.3, pp: 201-213

Application of VLF data through transformation into apparent resistivity profiles for identification of fracture zones in hard rock terrain

R. Kumar[1]* and G.S. Yadav[2]

[1]Geological Survey of India, CR, Nagpur-440006 (Maharashtra)
[2]Department of Geophysics, Faculty of Science, Banaras Hindu University, Varanasi 221005.
*Corresponding author: rajan.08.ism@gmail.com

ABSTRACT
The transformation of VLF-EM data into apparent resistivity is generally used to locate lateral inhomogeneity in subsurface formations. Transforming the VLF-EM data into apparent resistivity profile (lateral variation of apparent resistivity), collected from the part of hard rock area of Ahraura region, Mirzapur district, Uttar Pradesh (India), has helped to delineate the fissures and fractures zones on the basis of resistivity range by visual interpretation technique, such as much higher value of resistivity indicate hard rocks, while the much lower value indicate the conductive body. The obtained result is comparable to the results obtained from electrical gradient profile survey of DC resistivity. Finally, the response of apparent resistivity curves through transformation of VLF-EM data is compared with the results obtained from Fraser linear, Karous Hjelt filtering, and gradient resistivity profiling. The interpretation of VLF-EM data through Fraser linear and Karous Hjelt filter is based on zero-cross over point, which is indirectly related to geoelectrical parameter (apparent resistivity), can give imprecise result and have ambiguity. However, the apparent resistivity profile through the transformation of VLF-EM data, reduces the ambiguity and give results directly related to geoelectrical parameters, thus VLF-EM can easily be interpreted on the basis of geoelectrical parameters.

Keywords: Apparent resistivity profile, VLF-EM, Fraser, Karous Hjelt filter, and Vindhyan fringe belt.

INTRODUCTION

The Very low frequency electromagnetic (VLF-EM) method is an inductive exploration method that measures the variation in EM field components, related to the electrical structure of the subsurface. The method utilizes source of EM signals, propagated by a remote transmitter (Vertical Electric Dipole) within the frequency range of 15 to 30 kHz. VLF transmitters, which are mainly established for submarines communication, radially, transmit primary EM fields that consist of a horizontal magnetic field component (H_ϕ) and a vertical electric field component (Ez) perpendicular to the direction of propagation. At large distances from the transmitter (> several free-space wavelengths), the primary EM fields can be regarded as plane waves. Due to the interaction with local subsurface conductivity, the primary horizontal magnetic field generates a horizontal electric field (Ex) in the direction of propagation. Any conductivity variations, whose strike is relatively parallel to the direction of propagation of the plane wave, will generate secondary magnetic fields either inductively or galvanically. The measured ratios of vertical secondary field to the total horizontal field, reflect the variation of conductivity structure, allowing this method to become widely used for prospecting conductive materials since 1960's (Paal, 1965), and effectively fast and powerful for the study of geological structures to a maximum depth of about 100 m (Fischer et al., 1983). Various examples of geological and hydro-geological application of this method have been discussed comprehensively by McNeill and Labson (1991).

On the basis of measured parameters, VLF-EM methods are grouped into two types. The first one, only measures the components of the elliptically polarized magnetic field, called as VLF-EM or simply VLF-EM method, while the second type deals with the horizontal electric field component and the orthogonal horizontal magnetic field, making it possible to calculate the apparent resistivity and phase of impedance at the surface. This type is called VLF-R or sometimes referred as VLF-MT method, since it applies the same formulations as used in magnetotelluric (MT) method (Cagniard, 1953). The ratio of vertical magnetic component normalized by the horizontal magnetic component, H_z/H_y (called as Tipper), has been the main indicator of the electrical discontinuity in interpretation of VLF-EM data. This ratio exhibits a peak over the contact of two electrically different blocks and shows a zero-crossing response over a thin, vertical conductive dyke embedded in a layered half-space. Several transformation techniques, based on linear filtering, have been developed to improve VLF data resolution and to make them easier to recognize (Collet and Becker, 1968; Fraser, 1969; Paterson and Ronka, 1971; Karous and Hjelt, 1983; Pedersen, 1989; Ogilvy and Lee, 1991; Tabbagh et

al., 1991; Pedersen et al., 1994; Bastani and Pederson, 1997; Benson et al., 1997; Sharma and Kaikkonen, 1999; Bastani, 2001; Pedersen and Oskooi, 2004; Pedersen et al., 2009). Pedersen et al. (1994) proposed a horizontal derivative of the tipper vector (called Peaker) that peaks directly over the conductor. All these above techniques try to improve the VLF data on basis of zero-crossing response by locating the conductors without information about the geoelectrical parameter of subsurface features. Although an air borne technique measures the ratio of the horizontal and vertical electric fields (wave tilt) to determine the apparent resistivity (Arcone, 1979; Herz, 1986), traditionally in airborne VLF surveys, only the three components of the total magnetic field are measured. Chouteau et al. (1996) proposed a transformation filter that transforms the real part of the tipper vector into profiles of apparent resistivities, by assuming that horizontal magnetic field does not vary along the profile.

In the present work, the priori information of the study area was done using satellite imagery to extract the surface lineament and give the appropriate locations for selecting the electromagnetic (VLF-EM) geophysical surveys in study area. Very low frequency electromagnetic (VLF-EM) survey was conducted along eleven traverse profiles and provided location of high priority for further detailed exploration. Three gradient profiling (GP) surveys of DC resistivity method were carried out at the position of the VLF-EM anomaly. The transformation of VLF-EM data into lateral variation of apparent resistivity from part of hard rock area of Ahraura region, Mirzapur district, Uttar Pradesh (India) is done for delineating the fissures and fractures zones and corroborating the result with the Fraser linear, Karous Hjelt filtering and Gradient resistivity profiling.

VLF-EM PARAMETERS

Many commercial instruments measure the changes in the different parameters of the total field. For example, some instruments measure the dip of the major axis and the ellipticity of the polarization ellipse whereas; other instruments measure the vertical and horizontal field components (Smith and Ward, 1974). Figure 1a describes the configuration of a preferred VLF survey. The survey lines are approximately parallel to the incident magnetic field (y-axis) and at right angles to the geological strike of conductor (transverse electric [TE] mode) and to the direction of transmitter location (x-axis). Due to the presence of conductive inhomogeneity, secondary fields generated by the induced current are superimposed on the primary field, resulting in a total field that is elliptically polarized (Figure 1b).

TRANSFORMATION OF VLF-EM DATA INTO APPARENT RESISTIVITY

Approximation Solution

Transformation of VLF-EM (Tipper) into apparent resistivity profiles was first introduced by Chouteau et al. (1996), with the assumption that the spatial derivatives of horizontal magnetic field can be neglected along the profile. Gharibi and Pedersen (1999) proposed an improvement to this method by using the fact that the secondary horizontal fields are of internal origin and form a Hilbert transform pair. This method enables one to obtain the impedance tensor from the magnetic field (Gharibi and Pederson, 1999). To develop a method to estimate the resistivity and phase information from the tipper, one must examine the relation at the earth's surface between electric field E_X, and magnetic field H_Y and the apparent resistivity. This relation in a uniform half-space is usually written as

$$\rho_a = \frac{1}{\mu\omega}\left|\frac{E_x}{H_y}\right|^2 = \frac{1}{\mu\omega}\left|Z_{xy}\right|^2 \quad (1)$$

$$\theta = \tan^{-1}\frac{\mathrm{Im}\left[E_x / H_y\right]}{\mathrm{Re}\left[E_x / H_y\right]} \quad \text{in degree} \quad (2)$$

where, u= u_o is the magnetic permeability of free air, ω is the angular frequency, and Z_{xy} is the surface impedance, ρ_a is apparent resistivity and θ is the phase angle in between the horizontal electric field (E_x) and magnetic field (H_y) (Cagniard, 1953; Vozoff, 1960).

The method is expressed in terms of relationship between the horizontal and vertical magnetic fields at the surface, which is governed by the Maxwell's equations. For a source free region within the Earth, negligible time varying displacement currents, and negligible the variations in electrical permittivies and magnetic permeabilities of rocks compared with variations in bulk rock conductivity, the equations take the forms of

$$\nabla \times E = -\frac{\partial B}{\partial t} \quad (3)$$

$$\nabla \times H = \sigma E \quad (4)$$

$$\nabla . B = 0 \quad (5)$$

$$\nabla . E = 0 \quad (6)$$

where, E is the electrical field (in V/m), B is the magnetic induction (in T), H is the magnetic intensity (A/m), and σ is the conductivity of the medium (in S/m) (Pedersen et al., 1994).

In a 2-D TE mode, there are no field variations along the x- axis so the eq. (3) is reduced to

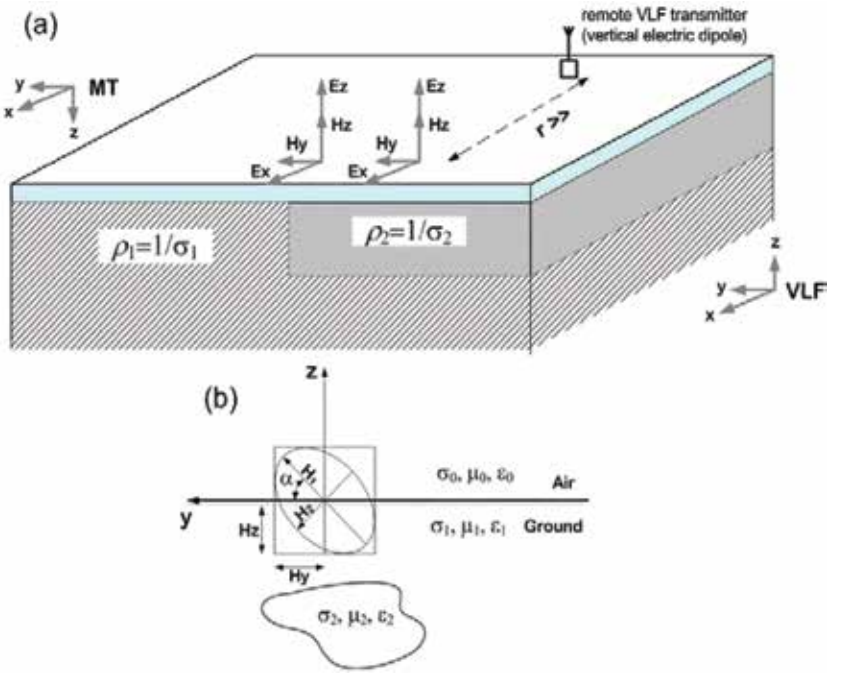

Figure 1. (**a**) Illustration of VLF-EM fields over inhomogeneous subsurface. (**b**) Polarization ellipse due to the presence of conductive inhomogeneity (Srigutomo et al., 2005).

$$\frac{\partial E_x}{\partial y} = \frac{\partial B_z}{\partial t} \tag{7}$$

or

$$\frac{\partial E_x}{\partial y} = i\omega\mu_o H_z \tag{8}$$

assuming a time dependence e^{iwt} of the magnetic induction. Integration of eq. (8) yields

$$E_x(y) = E_x(o) + i\omega\mu_o \int_0^y H_z(y')dy' \tag{9}$$

An approximate solution can be obtained by assuming the magnetic is constant along the y- axis (Chouteau et. al., 1996), i.e. $H_y(y) = H_o$. In this case eq. (9) can be expressed as

$$E_x(y) = E_x(o) + i\omega\mu_o H_0 \int_0^y T(y')dy' \tag{10}$$

where, T is tipper,

$$T(y') = \frac{H_z(y')}{H_y(y')} \tag{11}$$

Using the eq. (1) and (10), the surface impedance now can be given by-

$$Z_{xy}(y) = \frac{E_x(y)}{H_y(y)} = \frac{E_x(o) + i\omega\mu_o H_0 \int_0^y T(y')dy'}{H_0} \tag{12}$$

or

$$Z_{xy}(y) = Z_{xy}(o) + i\omega\mu_o \int_0^y T(y')dy' \tag{13}$$

$Z_{XY}(o)$ is the surface impedance at y = 0, that can called initial value of surface impedance, can be provided from either VLF-R or MT. Using eq.(1), the initial value of surface impedance at $y = 0$ can be calculated in term of initial value of apparent resistivity (Gharibi and Pedersen, 1999).

In actually, VLF-EM data acquired is sampled at interval of Δy then substituting eq. (1) in eq. (13) and expressing in term of apparent resistivity (Chouteau et al.1996, Srigutomo et al., 2005)

$$\left(\rho_{a\,j\,j+1}\right)^{1/2} = -(i\mu\omega)^{1/2} \sum_k^j \left(\frac{H_z}{H_y}\right)_k \Delta y + (\rho_a(o))^{1/2} \tag{14}$$

Equation (14), gives the apparent resistivity profile (lateral variation of apparent resistivity) through transformation of VLF-EM. In addition, Chouteau et al. (1996) also noted that omitting the imaginary part will not significantly change the transformed apparent resistivity due to its less reliability and smaller amplitude than the real part. In such case the eq. (14) becomes

$$\rho_{a\,j\,j+1}{}^{1/2} = -(\mu\omega)^{1/2} R_j \Delta y + \rho_a(o)^{1/2} \tag{15}$$

where, $j = 1, 2 \ldots n$, R is the real part of the VLF-EM data (in term of tipper). The computed apparent resistivity profile (lateral variation of apparent resistivity) is located half a sample interval ahead of point j and the initial value for apparent resistivity can be provided from a DC resistivity measurements.

Full Solution

Gharibi and Pedersen (1999) generalized the previous approximation such that the impedance can be expressed in its full form, i.e.

$$Z_{xy}(y) = \frac{E_x(y)}{H_y(y)} = \frac{E_x(o) + \int_0^y i\mu_o \omega H_z(y')dy'}{H_Y(Y)}$$

$$= Z_{xy}(o)\frac{H_y(o)}{H_y(y)} + \frac{i\omega\mu_o \int_0^Y H_z(y')dy'}{H_y(y)} \quad (16)$$

by making use the fact that secondary horizontal and vertical magnetic fields are of interval origin. The authors assumed the primary source of the horizontal magnetic field is constant along the y-axis, so that expressions of the magnetic field are

$$H_z = H_z^s \quad (17a)$$

$$H_y = H_y^p + H_y^s, \quad (17b)$$

and

where,

$H_Y^p = H_0$ is constant.

From the tipper formulation, the vertical magnetic field now can be expressed as

$$H_z(y) = H_y^s(y) = T(y)\,H(y)$$

$$= T(y)H_o + T(y)H_i\{H_z^s\}' \quad (18)$$

where, the Hilbert transform that relates the secondary vertical and horizontal magnetic fields is in the form of (Nabighian 1972).

$$H_i\{H_z^s\} = \frac{1}{\pi}\int_{-\infty}^{+\infty} \frac{1}{y' - y} H_y^s(y')dy' = H_y^s \quad (19)$$

Gharibi and Pedersen (1999) proposed an iterative the scheme to solve the full solution. First step is to calculate the following relation:

$$H_z^s(n+1) = T(y) + T(y)H_i\{H_z^s\}, \quad (20)$$

Where $H_0 = 1$ and $H_z(y) = T(y)$ are set as the initial values in the first iteration. Secondly, eq. (19) and eq. (17b) are applied to obtain H_y. Finally, H_y and H_z are substituted into eq. (16). The initial value $Z_{xy}(0)$ can be supplied at any location along the profile in the forms of either impedance or a pair of apparent resistivity and phase.

Application to VLF data analysis through transformation into apparent resistivity profiles in hard rock areas

METHODOLOGY AND STUDY AREA

The groundwater exploration projects had higher success rates when sites for drilling or detailed geophysical survey were guided by lineament mapping based on satellite images (Teme and Oni, 1991; Gustafsson, 1993). VLF-EM data were acquired using WADI instrument manufactured by ABEM. The procedure first consists of selecting a transmitter station which provides a field approximately parallel to the traverse direction, i.e. approximately perpendicular (or within ±20°) to the expected strike of a conductor. The instrument measured the real (in-phase) and imaginary (out-of-phase) components of the vertical to horizontal magnetic ratio. The VLF-EM data acquired along eleven VLF traverses at operating frequencies 18.2 and 19.7 kHz, were used for the entire VLF survey. The distance between measurement points along the line was 10 m, and the distance between profile lines along profile direction was 50 m, while the profile length varies between 250 and 500 m. Terrameter SAS 1000 (ABEM, Sweden), was used to conduct electrical resistivity survey and acquire gradient profiling data from the study area. The response of gradient profiling survey data was analyzed using software M.S. Excel (Kumar and Yadav, 2014). The qualitative interpretation of VLF-EM was done using Fraser and Karous-Hjelt filtering technique on the basis of zero-cross over point and transforming VLF-EM data into lateral variation of apparent resistivity on the basis of resistivity range by visual interpretation tecqunice. Finally, the response of apparent resistivity curves through transformation of VLF-EM data is corroborated with the result of Fraser linear, Karous Hjelt filtering, and result of resistivity survey (gradient resistivity profiling).

The area chosen for the study is the part of hard rock area of Vindhyan fringe belt, which is located in Mirzapur district of Uttar Pradesh, India (Figure 2). The study area partly falls in Survey of India toposheet No. 63O/4 and 63P/1 at 1:50,000 scales. The Vindhyan Supergroup is composed mostly of low dipping formations of sandstone, shale and carbonate, with a few conglomerate and volcaniclastic beds, separated by a major regional and several local unconformities (Bhattacharyya, 1996). The regional unconformity occurs at the base of the Kaimur Group and divides the sequence into two units: the Lower Vindhyans (Semri Group) and the Upper Vindhyans (Kaimur, Rewa and Bhander groups). The outcrop pattern of the Supergroup resembles a simple saucer-shaped syncline. It is generally believed that the Vindhyan basin was a vast intra-cratonic basin formed in response to intra-plate stresses (Bose et al. 2001). The bedrock (Vindhyan Super Group of rocks) is expected below the surface soil cover since the study area is lying in close vicinity of the Vindhyan exposures. The area is mainly flat and gently undulating terrain except in few parts. The occurrence and movement of groundwater are mainly restricted within the weathered and fractured sandstone/sandshale (Amaresh and Prakash, 2003; Kumar and Yadav, 2013; Kumar and Yadav, 2014).

RESULTS AND DISCUSSION

The Fraser filter to transform zero cross over into anomalous peaks are shown as solid arrow in Figure 3(a), whereas the transformed apparent resistivity from real component of VLF data in Figure 3(b) are shown as solid triangle (low apparent resistivity). Profile 1 (P1) is 500 m long and has two anomalies with little accumulation of current density at the position approximately 25 and 170 m. Profile 2 (P2) is parallel to profile P1, having two

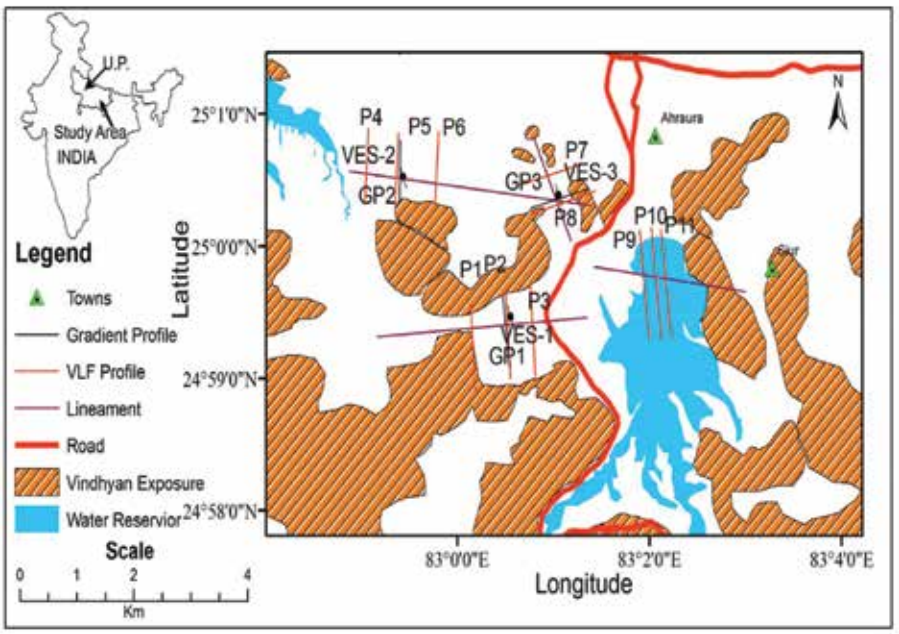

Figure 2. Location map of the study area

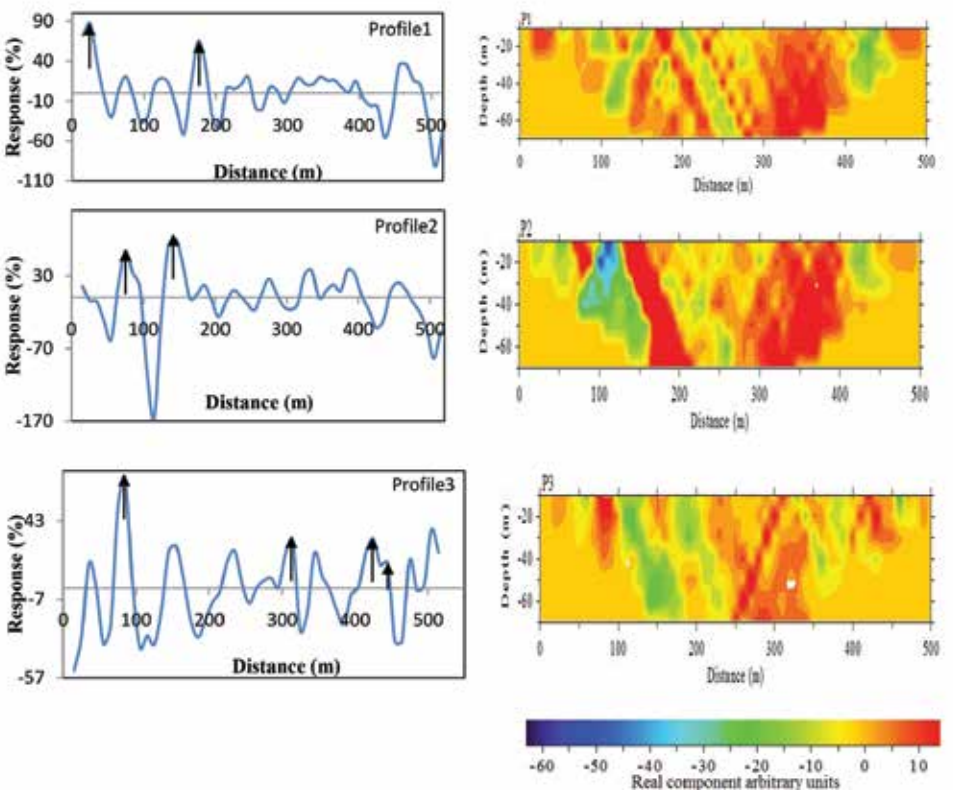

Figure 3(a). Fraser-filtered real data curves for profiles P1, P2, and P3 with their respective pseudo current density cross section.

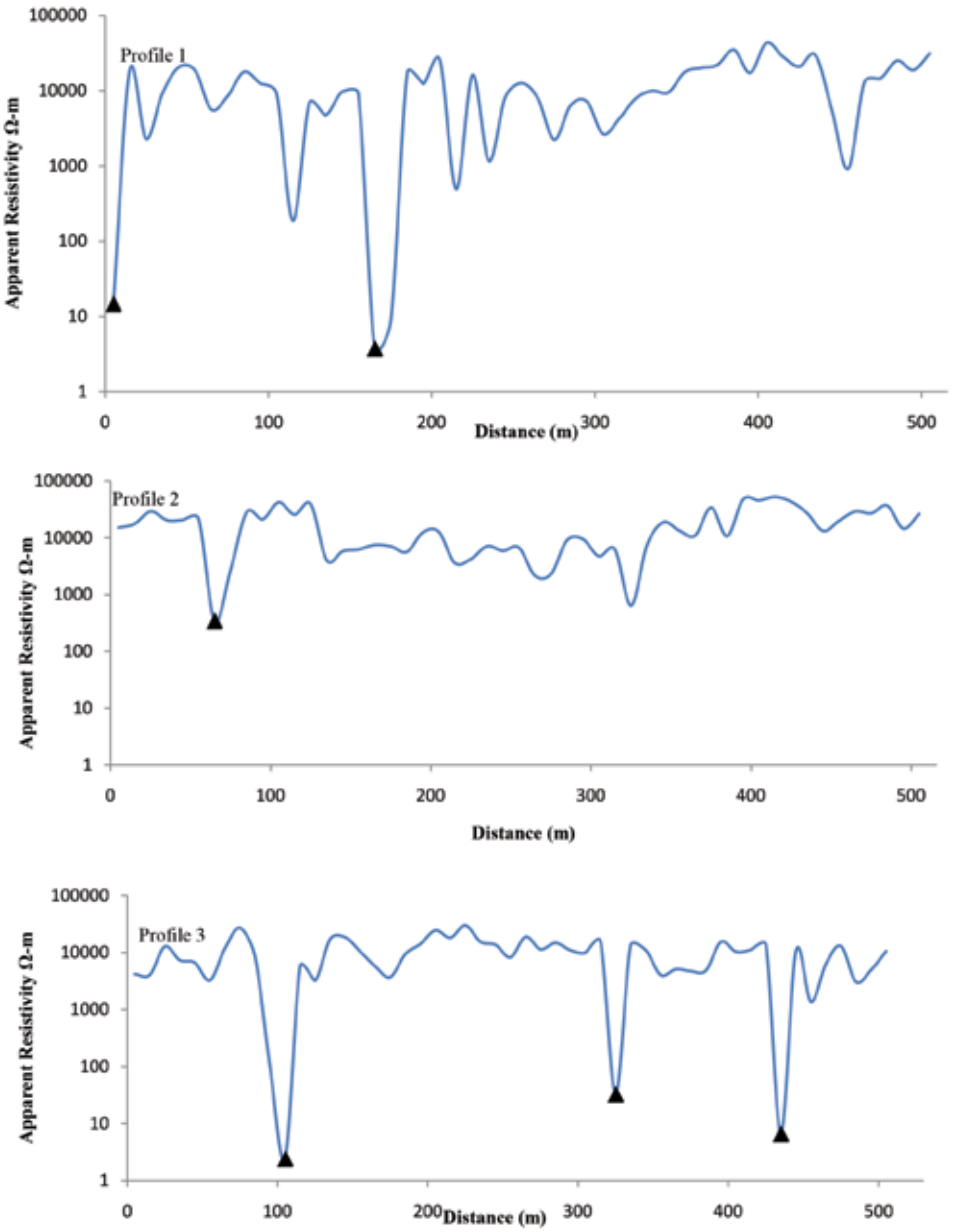

Figure 3(b). Response of apparent resistivity curves from transformation of VLF- EM data for profiles P1, P2, and P3.

anomalies with large magnitude and more accumulation of current density at the position approximately 70 and 140 m. Similarly, the profile 3 (P3), which is parallel to profiles P1 and P2, has four anomalies. One anomaly has a large magnitude with more accumulation of current density at the position approximately 80 m, and other three anomalies have low magnitude with less accumulation of current density. Transformation via the approximate solution was applied using initial value of apparent resistivity as obtained from the DC resistivity measurement. The lower value of apparent resistivity is observed at position approximate 25 and 170 m in Profile 1 (P1), at position approximate 70 m in Profile 2 (P2) and at position approximate 95, 330 and 430 m in Profile 3 (P3). Higher value of apparent resistivity indicates the presence of higher resistivity body such as that hard rock formation which can be seen in the field, where outcrops of country rocks are Vindhyans as shown in Figure 2. The lower apparent resistivity occurring in hard rock formation may indicate presence of fracture zone. Figure 3(c) shows the apparent resistivity response along the gradient profile GP1, with centre coinciding with the position of 70 m in VLF-EM profile (P2), having a high current density at the same position. The apparent resistivity value that increases at the beginning of the profile up to a distance of 10 m indicates the presence of hard rock formation. The apparent resistivity value

decreases to a value lower than 400 Ω m after 10 m. A low apparent resistivity value that occurs at the position of 25 m indicates the presence of low resistive body (probably fractured rocks) in hard rock formation. Again, the apparent resistivity value increases up to a distance of 50 m and a high apparent resistivity which occurs at the position of 50 m indicate the presence of hard rock formation. A low apparent resistivity value occurs after 70 m distance up to the ending of profile.

The Fraser filter to transform zero cross over into anomalous peaks is shown as solid arrow in Figure 4(a), whereas the transformed apparent resistivity from real component of VLF data that gives the anomalous zone in Figure 4(b), is shown as solid triangle (low apparent resistivity). Profile 4 (P4) is 250 m long and has four anomalies. The three anomalies have less accumulation of the current density, while the last anomaly has more accumulation of current density at the position approximately 200 m. Profile 5 (P5), which is parallel to profile P4 and has three anomalies in which the last anomaly has a large magnitude and more accumulation of current density at the position approximately 165 m. In comparison the profile 6 (P6), which is 160 m long and parallel to profiles P4 and P5, has two anomalies. The first

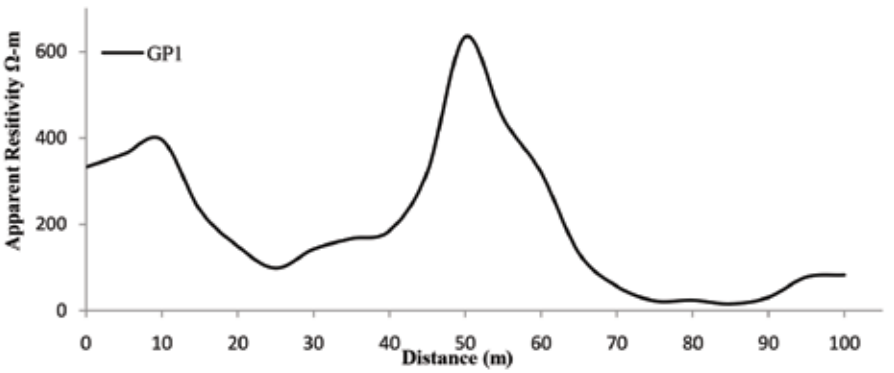

Figure 3(c). Response of gradient profiling along GP1.

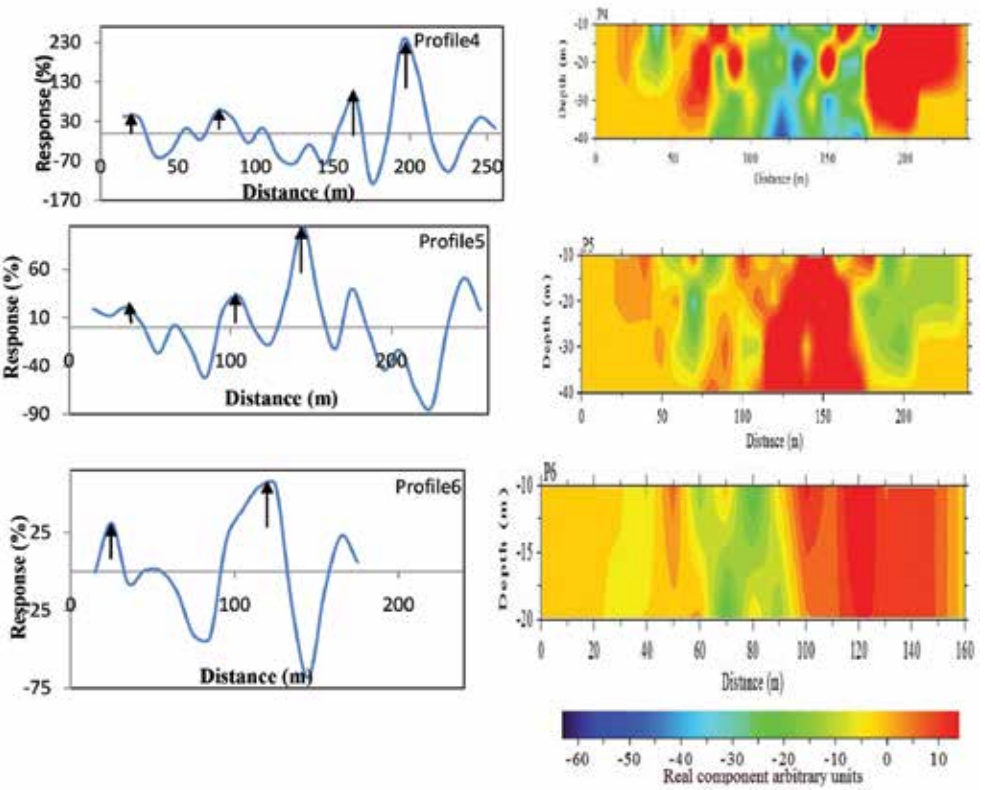

Figure 4(a). Fraser-filtered real data curves for profiles P4, P5, and P6 with their respective pseudo current density cross section.

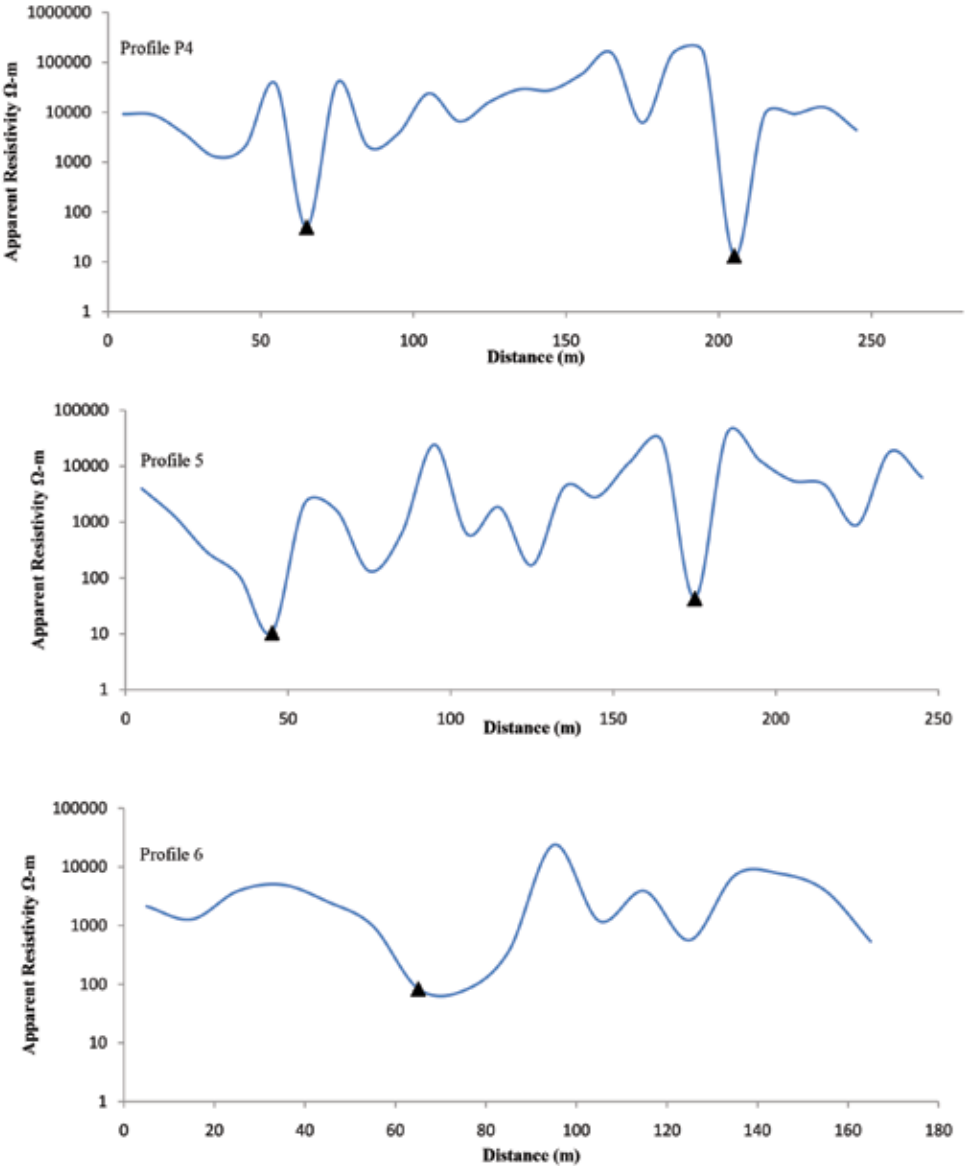

Figure 4(b). Response of apparent resistivity curves from transformation of VLF- EM data for profiles P4, P5, and P6.

anomaly has a low magnitude with less accumulation of the current density in comparison to the last one. To apply transformation by the approximate solution the initial value of apparent resistivity obtained from the DC resistivity measurement is used to transform the VLF-EM data into apparent resistivity profile. The lower value of apparent resistivity is observed at position approximate 70 and 200 m in Profile 4 (P4), at position approximate 50 and 170 m in Profile 5 (P5) and at position approximate 60 m in Profile 6 (P6). Higher value of apparent resistivity indicates the higher resistivity body such as hard rock formation. The lower apparent resistivity that occurs in hard rock formation may indicate presence of a fracture zone.

Similarly, Figure 4(c) shows the apparent resistivity response along the gradient profile GP2, with centre coinciding with the position of 165 m of VLF-EM profile (P5), having a high current density at the same position. The apparent resistivity value that increases at the beginning of the profile up to a distance of 30 m indicates the presence of hard rock formation. The apparent resistivity value suddenly decreases after 30 m up to a distance of 35 m and suddenly increases after the 35 m distance up to the ending of profile. A low apparent resistivity value that occurs at the position of 35 m indicates the presence of low resistive body (probably fractured rocks) in hard rock formation. The beginning of the profile up to 30 m and the distance from 40 m to the ending of profile indicate the presence of hard rock formation.

The Fraser filter to transform zero cross over into anomalous peaks is shown as solid arrow in Figure 5(a),

whereas the transformed apparent resistivity from real component of VLF data gives the anomalous zone in Figure 5(b) is shown as solid triangle (low apparent resistivity). Profile 7 (P7) is 300 m long and has two sharp anomalies with large magnitude and more accumulation of current density at the position approximately at 90 and 225 m. Profile 8 (P8) is parallel to the profile P7 and has only one anomaly with large magnitude and more accumulation of current density at the position approximately at 70 m. The lower value of apparent resistivity is observed at position approximate 70 and 270 m in Profile 7 (P7) and at position approximate 65 m in Profile 8 (P8). Higher value of apparent resistivity indicates the higher resistivity body such that hard rock formation which can be seen in the field (Outcrops of country rocks as Vindhyan exposure). The lower apparent resistivity occurs in hard rock formation that may indicate fracture zone in hard rock formation.

Figure 5(c) shows the apparent resistivity response along the gradient profile GP3, with centre coinciding

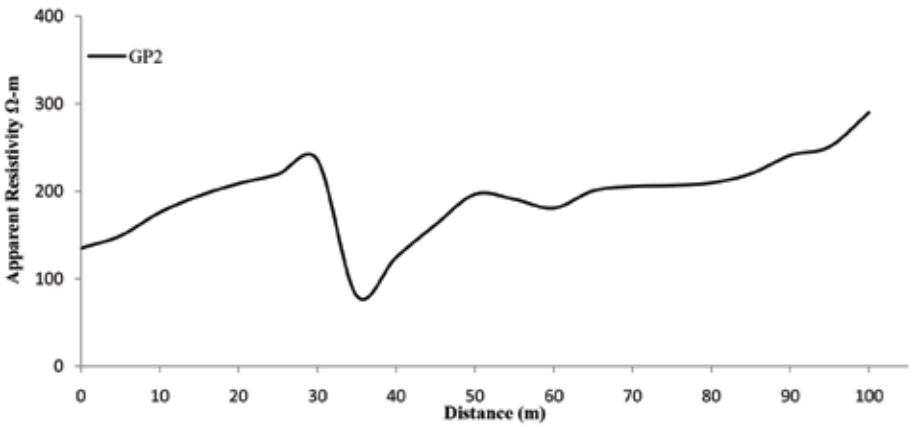

Figure 4(c). Response of gradient profiling along GP2.

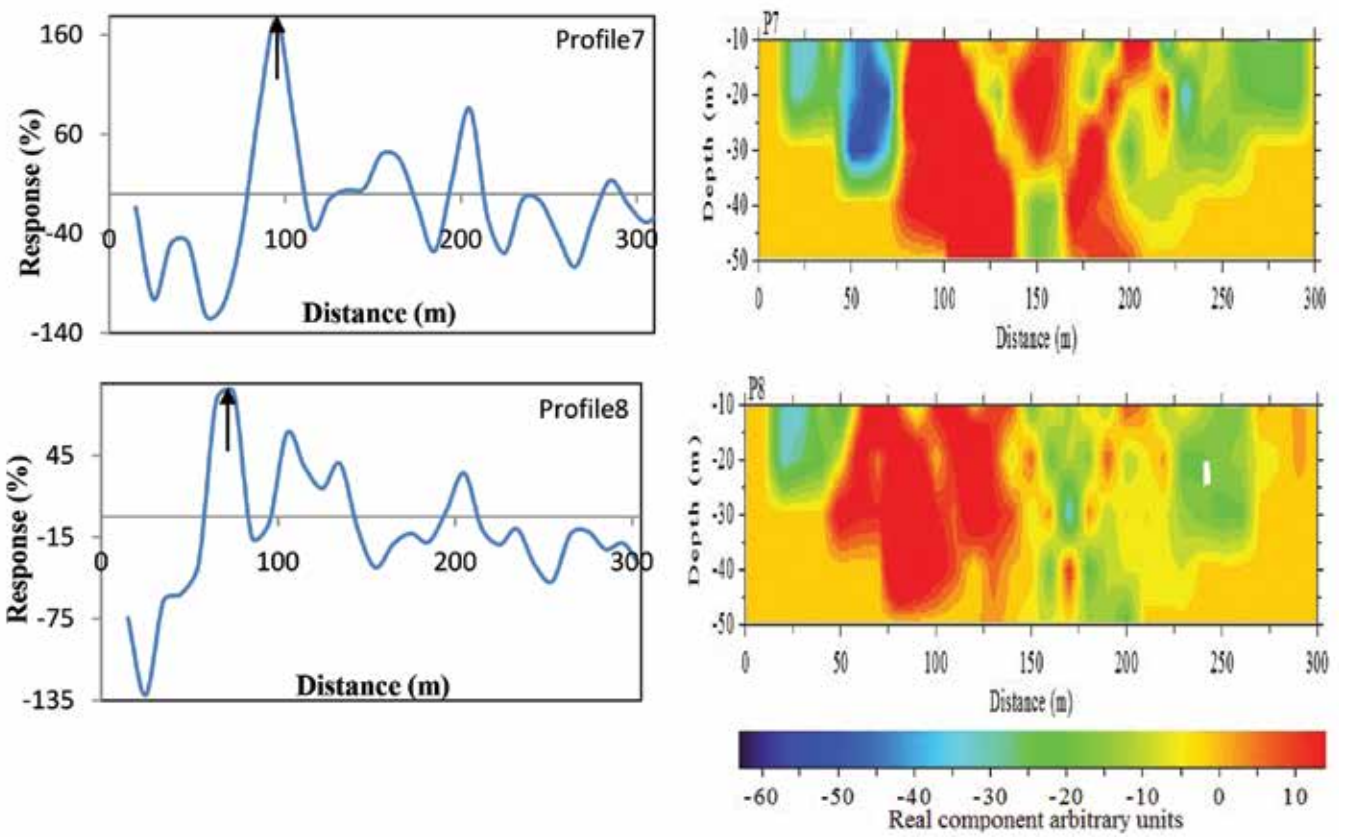

Figure 5(a). Fraser-filtered real data curves for profiles P7and P8 with their respective pseudo current density cross section.

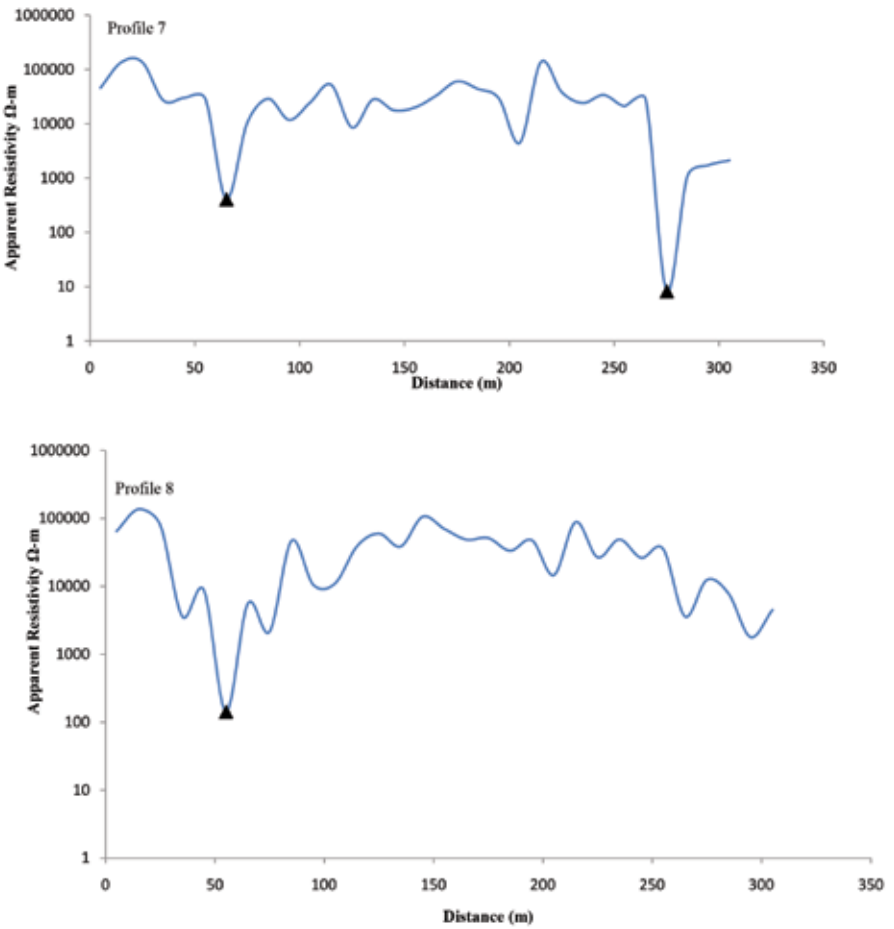

Figure 5(b). Response of apparent resistivity curves from transformation of VLF- EM data for profiles P7 and P8.

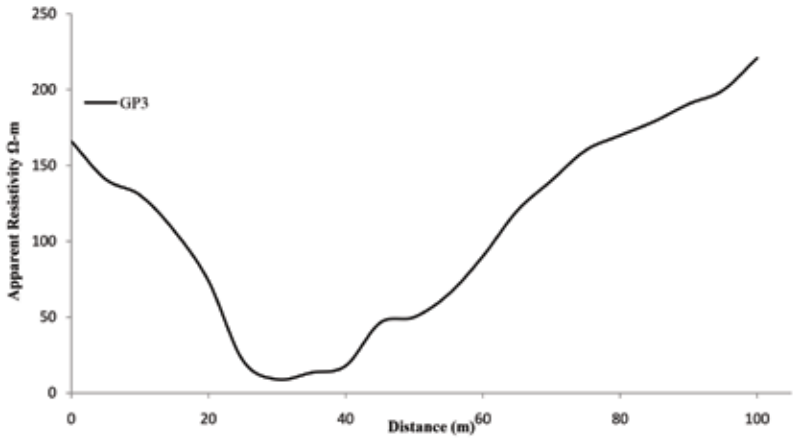

Figure 5(c). Response of gradient profiling along GP3.

with the position of 70 m in VLF-EM profile (P8), having a high current density at the same position. The apparent resistivity value that decreases at the beginning of the profile up to a distance of 20 m indicates the presence of hard rock formation. A low apparent resistivity value observed between positions 25 and 40 m indicates the presence of low resistive body (probably fractured rocks) in hard rock formation. Again, the apparent resistivity value increases after 40 m distance up to the ending of profile.

In an another site, which is located surrounding the Ahraura dam, only VLF-EM survey could be done because digging holes for electrode and also reaching of vehicle at that site was not possible. The Fraser filter to transform zero cross over into anomalous peaks is shown

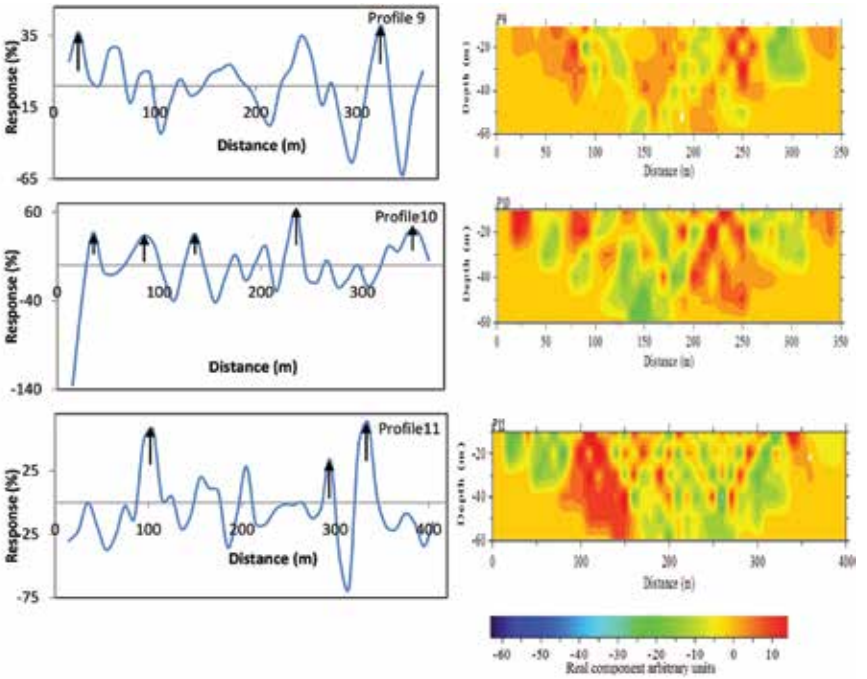

Figure 6(a). Fraser-filtered real data curves for profiles P9, P10, and P11 with their respective pseudo current density cross section.

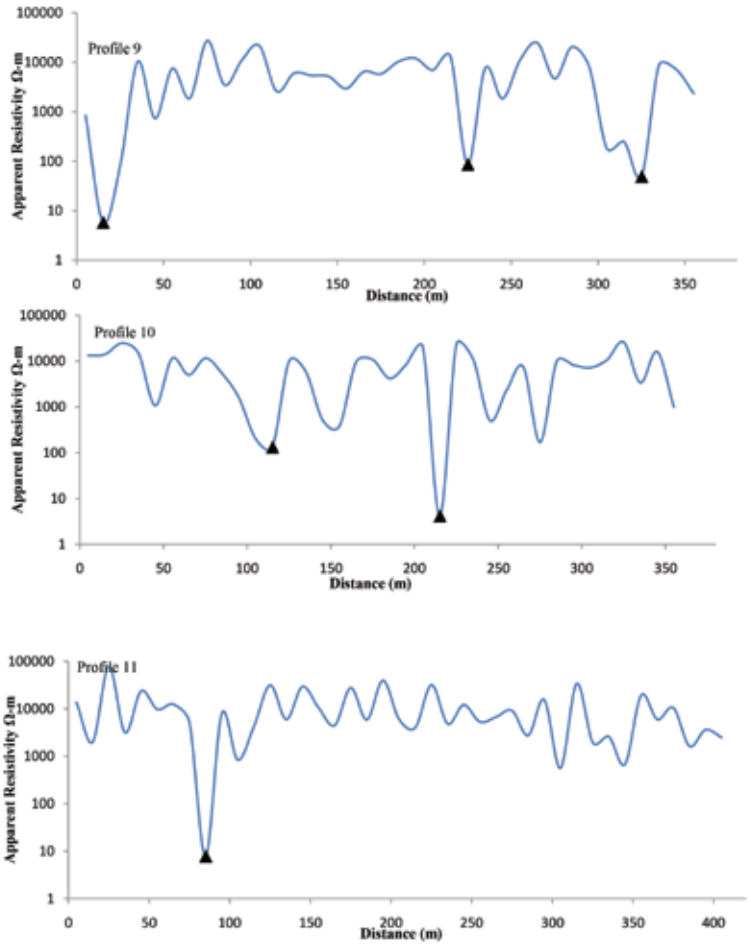

Figure 6(b). Response of apparent resistivity curves from transformation of VLF-EM data for profiles P9, P10, and P11.

as solid arrow in Figure 6(a), whereas the transformed apparent resistivity from real component of VLF data gives the anomalous zone in Figure 6(b) is shown as solid triangle (low apparent resistivity). Profile 9 (P9) is 350 m long and has two anomalies with little accumulation of current density at the position approximately 25 and 325 m. Profile 10 (P10) is parallel to profile P9, having five anomalies with low magnitude and little accumulation of current density. Profile 11 (P11), which is parallel to profiles P9 and P10, has three anomalies, in which only two anomalies have a large magnitude with more accumulation of current density at the position approximately 100 and 350 m, and other one anomaly has low magnitude with less accumulation of current density. Transformation via the approximate solution was applied using initial value of apparent resistivity as obtained from the DC resistivity measurement. The lower value of apparent resistivity is observed at position approximate 25, 225 and 325 m in Profile 9 (P9), at position approximate 110 and 220 m in Profile10 (P10) and at position approximate 95 m in Profile 11 (P11). Higher value of apparent resistivity indicates the higher resistivity body such that hard rock formation (outcrops of country rocks as Vindhyan exposure). The lower apparent resistivity occurs in hard rock formation that may indicate fracture zone in hard rock formation.

CONCLUSIONS

In this article, the transforming real component of VLF-EM response into apparent resistivity along the profile of measurements have been carried out. The transformation is based on the formulation of approximate solution and full solution proposed by Chouteau et al. (1996) and Gharibi and Pedersen (1999). The identified location of anomalous zone from transforming the VLF-EM data into apparent resistivity profile is fitted well to its identified location from Fraser linear, Karous Hjelt filter and gradient profile (GP) of DC resistivity. The apparent resistivity profile through the transformation of VLF-EM data reduces the ambiguity, as compared to those observed in Fraser linear and Karous Hjelt filtering, VLF-EM data can be easily interpreted on the basis of geoelectrical parameters like apparent resistivity.

ACKNOWLEDGEMENT

The authors are grateful to the Department of Geophysics, Banaras Hindu University for providing the necessary facilities required for geophysical survey. We are thankful to the reviewers and editor of the journal who have given critical and thoughtful suggestions.

Compliance with Ethical Standards

The authors declare that they have no conflict of interest and adhere to copyright norms.

REFERENCES

Amaresh, K.S. and Prakash, S.R. 2003. An integrated approach of remote sensing, geophysics and GIS to evaluation of groundwater potentiality of Ojhala subwatershed, Mirzapur district, U.P., India. Map India Conference, 2003. http://www.GISdevelopment.net. Accessed 29 Oct 2012.

Arcone, S.A. 1979. Resolution of studies in airborne resistivity surveying at VLF. Geophysics 44, 937-946.

Bastani, M. and Pedersen, L.B. 1997. The reliability of aeroplane attitude determination using the main geomagnetic field with application to tensor VLF data analysis. Geophys. Prosp. 45, 831-841.

Bastani, M. 2001. EnviroMT- A New Controlled Source/Radio Magnetotelluric System. Ph. D. Thesis. Acta Universitatis Upsaliensis, Uppsala Dissertations from the Faculty of Science and Technology 32.

Benson, A.K., Payne, K.L. and Stubben, M.A. 1997. Mapping groundwater contamination using DC resistivity and VLF geophysical methods- a case study. Geophysics, 62, 80-86.

Bhattacharyya, A. 1996. Recent advances in Vindhyan geology. Geol Soc India Mem. 36:331.

Bose, P.K., Sarkar, S., Chakrabarty, S. and Banerjee, S., 2001. Overview of Mesoto Neoproterozoic evolution of the Vindhyan basin, Central India. J. Sediment Geol 142:395–419.

Cagniard, L., 1953. Basic theory of the magneto-telluric method of geophysical prospecting. Geophysics 18, 605-635.

Chouteau, M., Zhang, P. and Chapellier, D., 1996. Computation of apparent resistivity profiles from VLF-EM data using linear filtering, Geophys. Pros. 44, 215-232.

Collet, L.S. and Becker, A., 1968. Radiohm method for earth resistivity mapping. Canadian Patent No. 795919.

Fischer, G., Le Quang B.V. and Muller I., 1983. VLF ground surveys, a powerful tool for the study of shallow two-dimensional structures, Geophys. Prosp., 31, 977-991.

Fraser, D.C., 1969. Contouring of VLF-EM data. Geophysics, 34, 958-967.

Gharibi, M. and Pedersen, L.B., 1999. Transformation of VLF data into apparent resistivity and phases, Geophysics, 64, 1393-1402.

Gustafsson, P., 1993. Satellite data and GIS as a tool in groundwater exploration in semi-arid area. Publication A 74. Chalmers University of Technology, Gothenburg.

Herz, A., 1986. Airborne E.M. instruments operating at VLF and higher frequencies, in Palacky, G.J, Ed., Airborne resistivity mapping Geological survey Canada, 55-61.

Karous, M. and Hjelt, S.E. 1983. Linear filtering of VLF dip-angle measurements. Geophys. Prosp. 31, 782-794.

Kumar, R. and Yadav, G.S., 2014. Delineation of fracture zones in the part of Vindhyan fringe belt of Ahraura region, Mirzapur district, Uttar Pradesh, India using integrated very low frequency electromagnetic and resistivity data for groundwater exploration. Arabian J. Geosciences, DOI: 10.1007/s12517-014-1283-4.

Kumar, R. and Yadav, G.S., 2014. Geohydrological Investigation using Schlumberger sounding in part of Hard Rock and Alluvial Area of Ahraura Region, Mirzapur District, Uttar Pradesh, India. Arabian J. Geosciences, DOI: 10.1007/s12517-014-1447-2.

Kumar, R. and Yadav, G.S., 2013. Forecasting of Rain Fall in Mirzapur District, Uttar Pradesh, Feed-Forward Artificial Neural Network. Int. J. Engineering Sci. Invention, 2(8): 87-93, ANED-DDL: 26.6718/0281087093.

McNeill, J.D. and Labson, V.F., 1991. Geological mapping using VLF radio fields in Nabighian, M.N., Ed., Electromagnetic methods in applied geophysics II. Soc. Expl. Geophysics 521-640.

Nabighian, M.N. 1972. The analysis signal of two-dimensional magnetic bodies with polygonal cross-section: Its properties and use for automated interpretation, Geophysics, 37, 507-517.

Ogilvy, R.D. and Lee, A.C., 1991. Interpretation of VLF-EM in-phase data using current density pseudo-sections. Geophys. Prosp., 39, 567-580.

Paal, G. 1965. Ore prospecting based on VLF-radio signals. Geoexploration 3, 139-145.

Paterson, N.R. and Ronka, V., 1971. Five years of surveying with the very low frequency electromagnetic method. Geoexploration 9, 7-26.

Pedersen, L.B., 1989. Relation between horizontal and vertical gradients of potential fields Geophysics 54, 662-663.

Pedersen, L.B., Qian, W., Dynesius, L. and Zhang, P., 1994. An airborne tensor VLF system, from concept to realization. Geophys. Pros. 42, 863-883.

Pedersen, L.B. and Oskooi, B., 2004. Airborne VLF measurements and variations of ground conductivity, a tutorial. Surveys in Geophys. 25, 151-181.

Pedersen, L.B., Persson, L., Bastani, M. and Bystrom, S., 2009. Airborne VLF measurements and mapping of ground conductivity in Sweden, J. Appl. Geophys., 67, 250-258.

Sharma, S.P. and Kaikkonen, P., 1999. Appraisal of equivalence and suppression problems in 1D EM and DC measurements using global optimization and joint inversion. Geophys. Prosp. 47, 219-249.

Smith, B.D. and Ward, S.H., 1974. On the computation of polarization ellipse parameters. Geophysics, 39, 867-869.

Srigutomo, W., Harja A., Sutarno, D. and Kagiyama T., 2005. VLF data analysis through transformation into resistivity value: Application to Synthetic and field data, Indonesia J. Physics, 16(4), 127-136.

Tabbagh, A., Benderitter, Y., Andrieux, P., Decriaud, J.P. and Guerin, R., 1991. VLF resistivity mapping and verticalization of the eiectric freld. Geophys. Prosp. 39, 1083-1097.

Teme, S.C. and Oni, S.F., 1991. Detection of groundwater flow in fracture media through remote sensing technique-some Nigerian cases, J. Afr. Earth Sci. 12(3), 461–466.

Vozoff, K., 1960. Numerical resistivity interpretation: General inhomogeneity. Geophysics, XXV (6), 1184-1194.

Received on: 1.11.18; Revised on: 25.3.19; Accepted on: 12.4.19

J. Ind. Geophys. Union (May 2019)
v.23, no.3, pp: 214-222

Subsurface structure of the offshore Trincomalee, NE of Sri Lanka

Shantha S.N. Gamage[1*], K.C.C. Silva[1], and D.A. Weerasinghe[2]

[1]Department of Physics, Faculty of Applied Sciences, University of Sri Jayewardenepura, Sri Lanka
[2]Petroleum Resources Development Secretariat, Ceylinco House, Colombo, Sri Lanka
*Corresponding author: shanthagamage@sci.sjp.ac.lk

ABSTRACT

Lanka basin of Sri Lanka, is an ultra-deep-water basin, which is now in focus due to economic importance, thus needed further exploration. This region consists of a prominent northeast –southwest trending gravity anomaly in the offshore Trincomalee region, which is known as a seismically virgin area. In this study, an attempt was made to generate a subsurface model using the freely available satellite and ship-borne gravity and ship track bathymetry data. An iterative algorithm was developed to calculate the gravity anomaly, caused by a two dimensional polygonal body having a density contrast with the surrounding, constrained further by available seismic data. The gravity anomaly caused by the upper mantle was obtained by arithmetic operations of the calculated gravity anomalies and the satellite derived free air gravity anomaly. Conventional trial and error method was finally employed to determine the structure of upper mantle that indicates the depth of Mohorovićič discontinuity. The lowest thickness of the oceanic crust in the basin is 2 km and the average sedimentary thickness is about 6 to 8 km. The Mohorovićič discontinuity was found to be around 12-14 km along the chosen profile. The results are of significance, as they can be used to interpret the evolution of the basin and depict the interested regional areas for further seismic surveys and oil and gas explorations.

Keywords: Density contrast, Gravity studies, Lanka basin, Mohorovičić discontinuity, Upper mantle, Seismic velocity.

INTRODUCTION

Sri Lanka occupies a unique geologic position in Gondwana land. Its location is of particular significance since Sri Lanka acts as a bridge across the main East African and Antarctica crustal fragments. Sri Lanka has a rich sedimentary base in sea area. Early Miocene age is the period where the two plates collided, Himalayan mountain range was formed and major rivers like Ganges started supply of sediments to this region (Kularathna et al., 2015a). Since then, large amount of sediments have been accumulating in the passive margins of this region. Earlier, extensive exploration work has been carried out in both Cauvery (Baillie et al., 2002; Chandra et al., 1991) and Mannar (Kularathna et al., 2015b); Ratnayake et al., 2014; Premarathne et al., 2013) basins. Though, the interest in exploration for hydrocarbon in the ultra-deep Lanka Basin has only recently been started and still not much data is available over this region (Gamage et al., 2018; Ratnayake et al., 2017). Further exploration may establish presence of hydrocarbons in the Lanka basin for future energy needs. Sri Lanka had been a part of the East Gondwana super continent and has undergone at least two prominent rifting phases during the Gondwana breakup time. The first rifting phase which is less prominent, initiated around 165 Ma ago, has resulted in the formation of NE-SW and NW-SE discontinuities in the Mannar Basin (Figure 1). The second rifting phase, which was more prominent, has commenced around 142 Ma ago and had resulted in the formation of Cauvery and Lanka Basins (Kularathna et al., 2015), the latter opening up to Bay of Bengal (Rao et al., 1997; Rao et al., 1994). Locations of the basins around offshore Sri Lanka are shown in the Figure 1.

METHODOLOGY AND DATA

For the present study, we use satellite gravity and the bathymetry data. Selected area for the study includes onshore as well as off shore areas in eastern side of offshore Trincomalee. The gravity data in a 1- minute grid was obtained from the TOPEX project web site. ESRI ArcGIS software was used to create necessary shape files and for the purpose of coordinate conversions. Sedimentary Thickness map of Lanka basin and sedimentary thickness variation along the A-A1 line (Figure 3), as acquired from a previous research work in Lanka basin (Silva et al., 2018) are shown in Figures 2 and 3 respectively.

Talwani et al., (1959) had put forward an algorithm to compute the gravity anomaly caused by a two-dimensional body in the subsurface, based on iterative modelling. The boundary of the two-dimensional body is approximated closely to a polygon, by marking the number of sides of the polygon sufficiently large. This method assumes that the anomalous body is infinitely long and parallel to the strike of the structure. The cross section of the body is replaced by countless thin rods or line elements aligned parallel to the strike (Talwani et al., 1959; Lowrie, 2007). Mathematical expression has been obtained for both the vertical and horizontal components of the gravitational attraction due to this polygon at any given point.

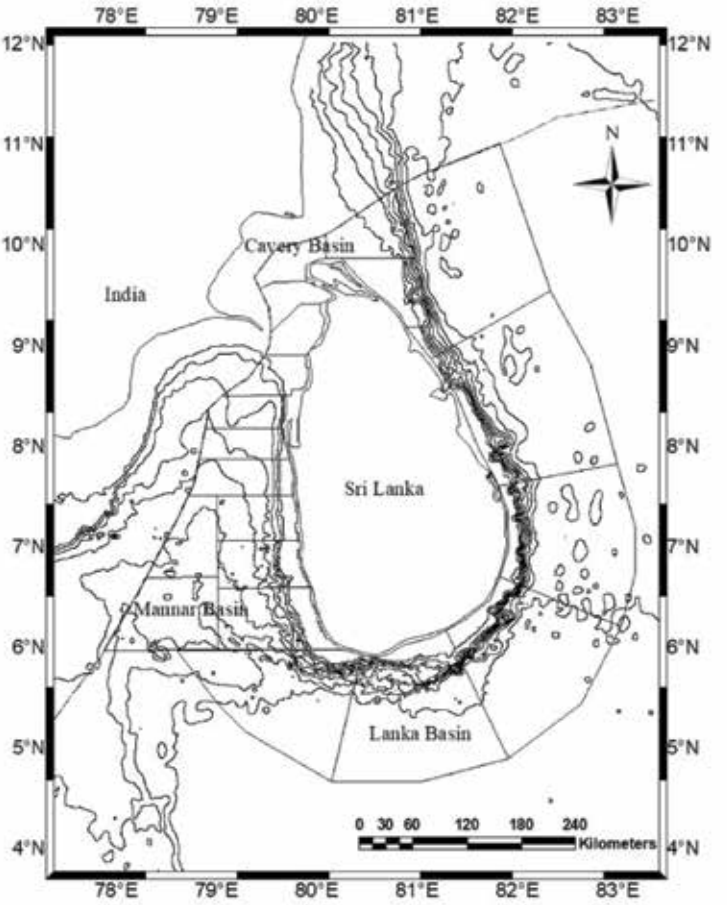

Figure 1. Basins of Sri Lanka (WGS 1984).

A simplified equation for the vertical component of given in the equation is given in the equation 1.

$$\Delta g = 2G\rho \{[z_1 \mathrm{Cos}\phi + \mathrm{Sin}\phi][(\theta_1 - \theta_2)\mathrm{Cos}\phi - \ln(r_1/r_2)\mathrm{Sin}\phi] + z_2\theta_2 - z_1\theta_1\} \quad -(1)$$

In order to execute this algorithm, a wolfram Mathematica program was written. The x- and z-coordinates of the vertices of the polygonal body (in km) in a counter clockwise sense were introduced in the program. The density contrast (in g/cm^3), number of vertices in the polygonal body, number of field points for the calculation of the anomaly and the interval between adjacent field points (in km), were given as inputs. Density contrast was calculated as the difference between the density of the material that had replaced the originally existed material and the density of the originally existed material.

The output of the program provides a table of calculated gravity anomaly caused by the polygonal body at each field point along the mean sea level. The variation of the gravity anomaly caused by the polygonal body along a horizontal axis on the mean sea level was plotted on a graph. Figure 4 shows the parameters used by the equation 1.

The tabulated data for each subsurface horizon were arranged in an order, such that two adjacent horizons including the free water surface, were coupled together to form different subsurface bodies or polygons. Starting from the Bengal Bay end (oceanic end), the x and z coordinates were ordered such that they defined the polygon in a counter clockwise sense.

The densities of the sedimentary column and oceanic water were taken as 2.40 and 1.03 g/cm^3 (Reddy, 2002). The density of the basement was taken as 2.65-2.8 g/cm^3, since the basement in this region was assumed to be composed of metamorphic rocks of the north-eastern area and the densities of common metamorphic rocks range from 2.65g/cm^3 to 3.03 g/cm^3(Smithson, 1971). Figure 5 shows the gravitational image of the onshore and offshore regions around Sri Lanka. Summary of the densities of subsurface layers are given in Table 1.

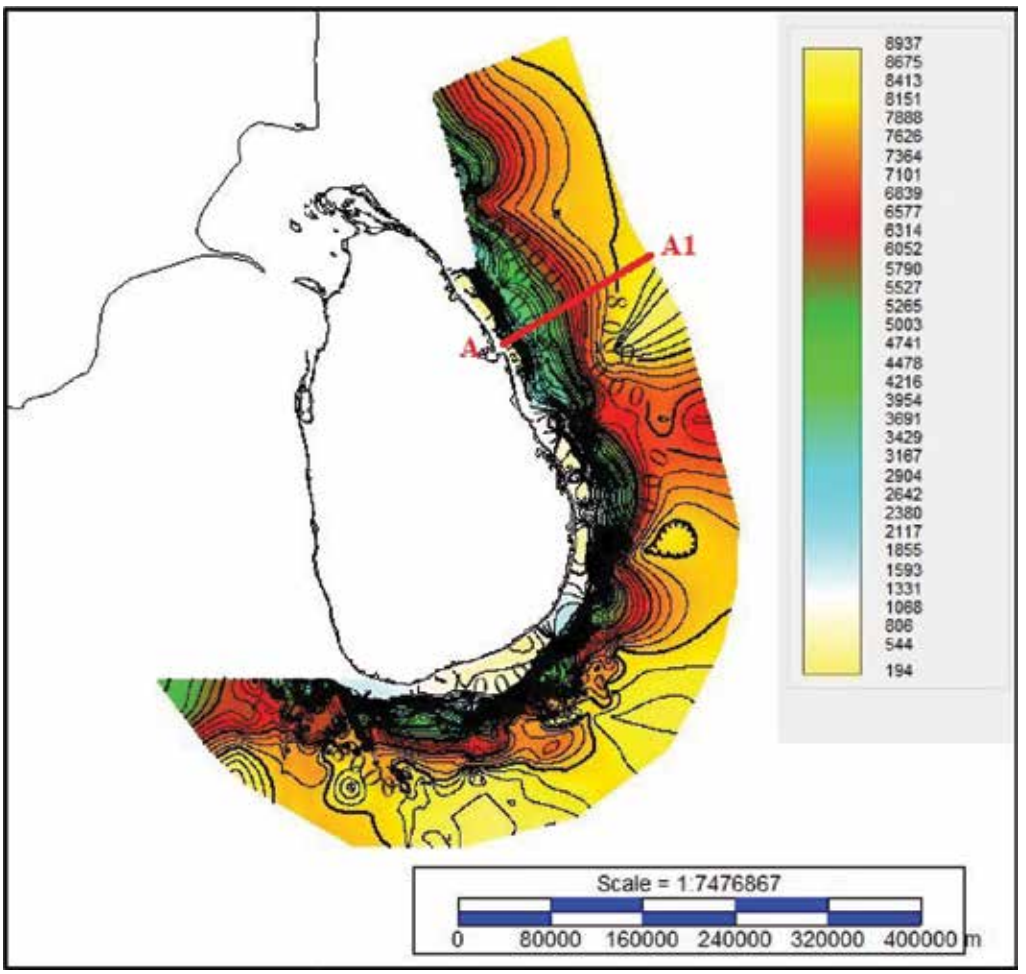

Figure 2. Sedimentary Thickness map of Lanka Basin (Silva et al., 2018)

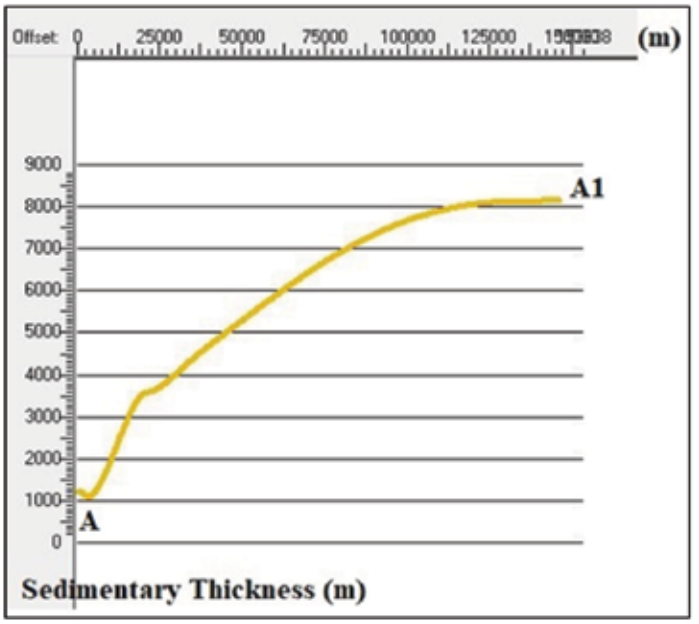

Figure 3. Sedimentary thickness along the line A-A1 (Silva et al., 2018)

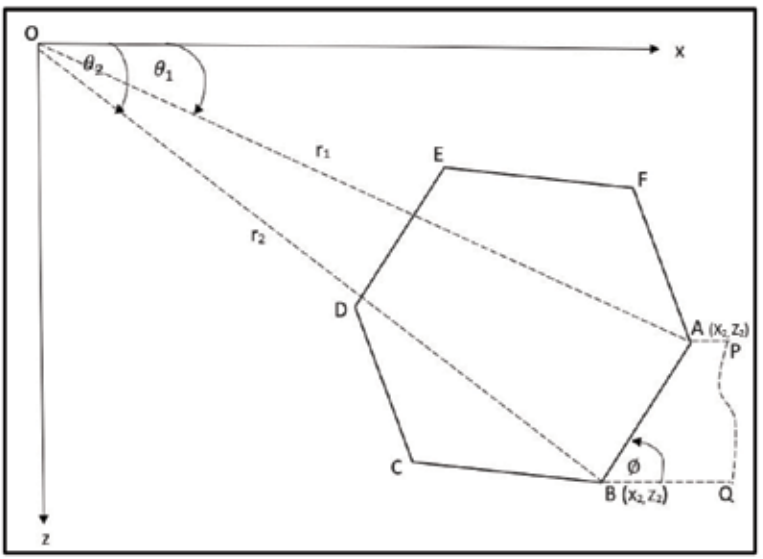

Figure 4. Geometrical elements involved in the gravitational attraction of an n-sided polygon (modified after Talwani et al., (1959))

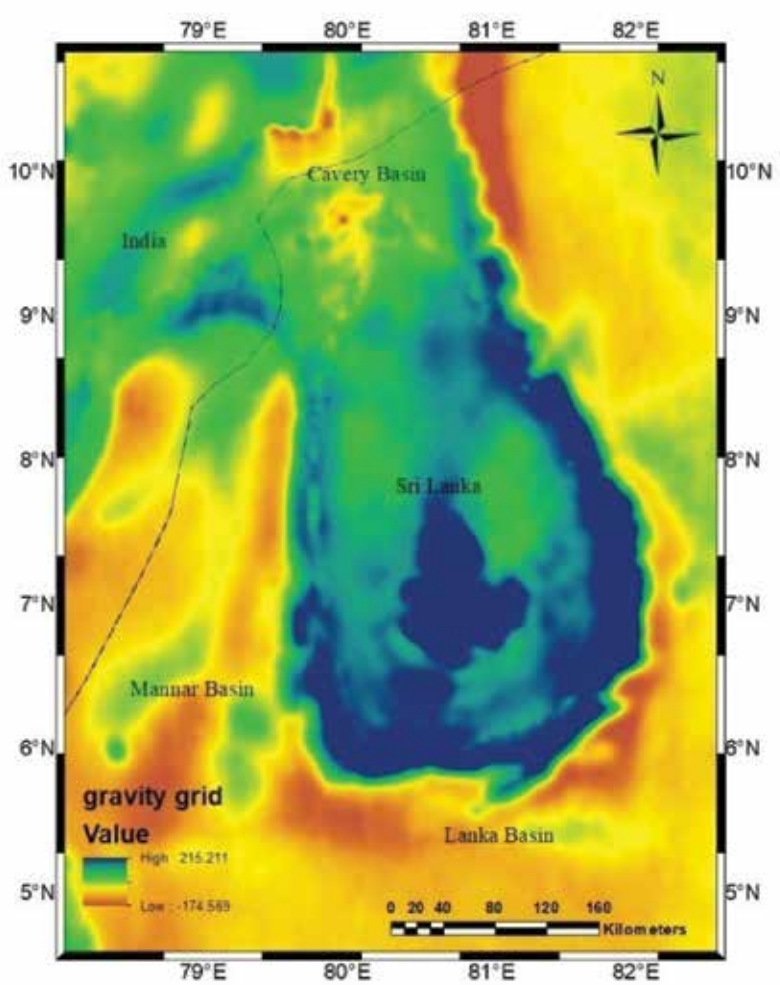

Figure 5. Gravity image map of Sri Lanka and its surrounding regions (WGS 1984)

Table 1. Summary of the densities of subsurface layers

Layer	Average Density(g/cm^3)
Water Column	1.03
Sedimentary Column	2.40
Average crust density	2.65-2.8
Mantle density	3.2-3.4

Calculated gravity anomalies for each subsurface layer were added together. Addition was then subtracted from the observed free air gravity anomaly to obtain the residual gravity anomaly. The residual gravity anomaly was assumed to be caused by the upper mantle in this region as the gravity anomaly measurements are made relative to the crust/basement. Thereafter, a model for the upper mantle was produced with the trial and error approach, such that the gravity anomaly calculated for the model with a suitable density contrast between the upper mantle and the basement, matched with the residual gravity anomaly of the upper mantle. Furthermore, the summation of all the calculated gravity anomalies including that by the model of the upper mantle was compared with the observed free air gravity anomaly. The subsurface horizons and the model of the upper mantle were combined together to represent the lithological and structural arrangement of the subsurface of the Lanka basin.

RESULTS AND DISCUSSION

Gravity profile along the section A1-A is shown in Figure 6. Along this profile, two crustal Models, A and B, have been generated, as discussed below.

(i) Model A

The gravity anomalies calculated using the mathematical program for each subsurface layer is shown from figures 7.1-7.5 for the Model A. Besides, the computed gravity anomalies and corresponding subsurface structure in the Lanka basin in case of model A, that also depicts the depth to the Mohorovićič discontinuity is, are shown in Figure 8.

(ii) Model B

Similarly, the observed free air gravity anomaly and the derived shallow structure along the Profile A1-A, in case of Model B, is shown in below.

From the two models proposed in the study, model A seems to be more realistic than the model B. Density contrast of the model A was set at 0.60 g/cm^3.The average thickness of the crust in model A came to be around 4.5 km. The value of 3.38 g/cm^3 for density of the upper mantle in the oceanic region is considered appropriate. Density contrast in model B was set at 0.55g/cm^3. In model B, crustal thickness was found to be about 7 km in most of the region which was rather unrealistic. Therefore model A is

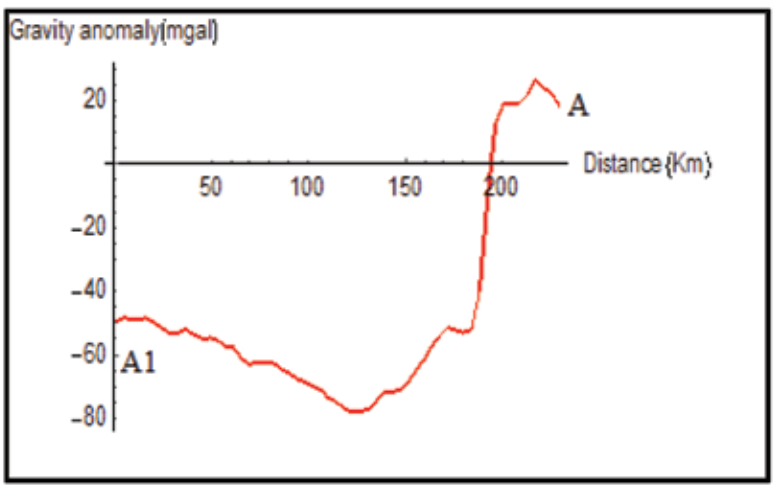

Figure 6. Observed gravity anomaly along the section A1-A.

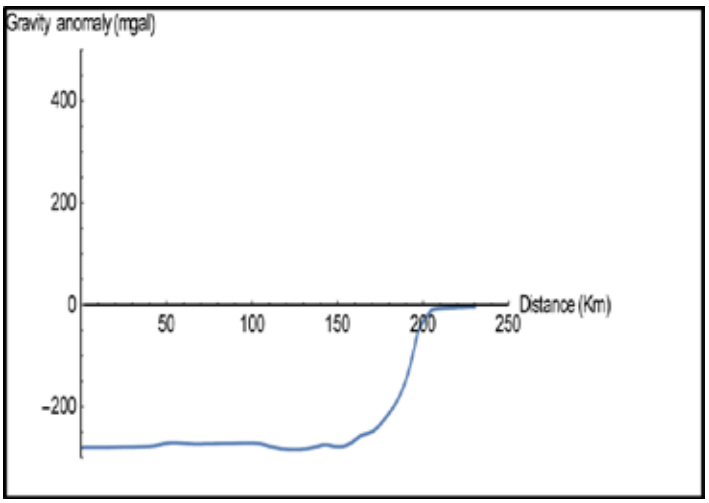

Figure 7.1. Gravity anomaly caused by water column

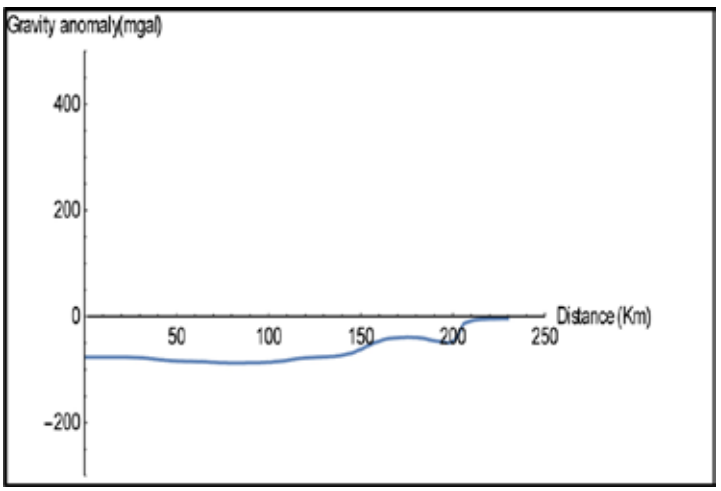

Figure 7.2. Gravity anomaly caused by Sedimentary column

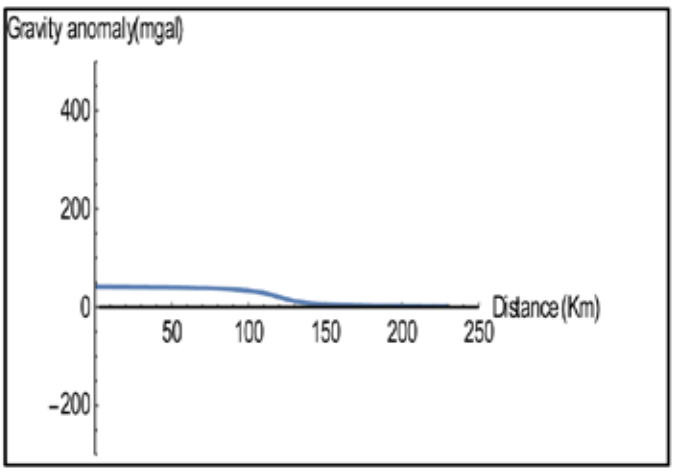

Figure 7.3. Gravity anomaly caused by crust column 1

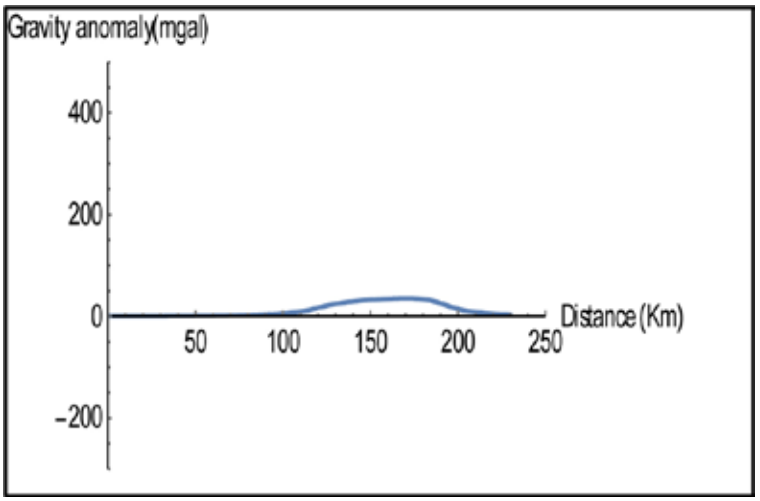

Figure 7.4. Gravity anomaly caused by crust column 2

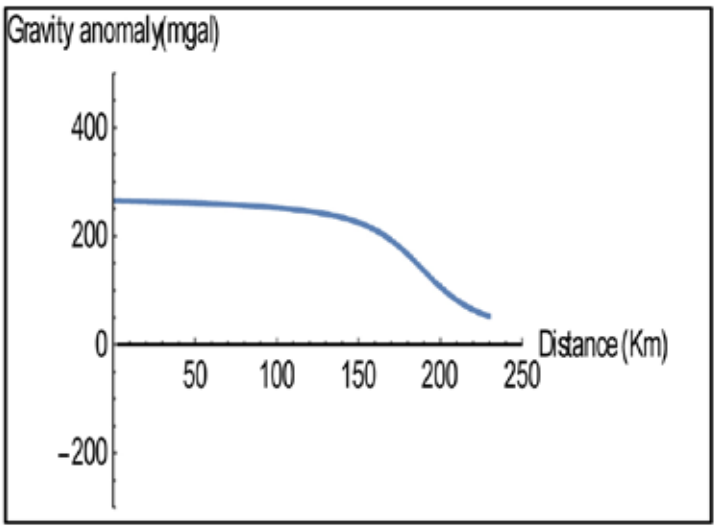

Figure 7.5. Gravity anomaly caused by mantle column.

more acceptable than the model B. The weight of overlying rocks would have cause an increase in the density of the basement rocks at greater depths. Values for the average density of basement lies between 2.6 g/cm^3 and 2.8 g/cm^3 which could be higher in the far oceanic region. In this study, we use the average densities. However, in the reality, there could be lateral density variations in the subsurface layers that yield localized gravity anomalies in the gravity anomaly profiles. This issue could have been minimized, if the densities of subsurface rock layers were available from several exploratory wells along the profile. Since the exploratory wells were not available, such localized gravity anomalies were assumed to be negligible. The horizontal components of gravitational acceleration as assumed to be negligible in this study, since it has a very minimum influence compared with the vertical component.

It can be observed from model A, that the calculated gravity anomaly and the observed free air gravity anomaly show a drastic difference at the distances between 200 km and 250 km (Figure 8(a)). At those distances, the landmasses of Sri Lanka was emerging from the sea and therefore, Bouguer gravity anomaly has to be used instead of free air gravity anomaly in such regions. Since the study was highly focused on the region occupied by the anomalous gravity which was overlain by oceanic water, free air gravity anomaly was better suited for those regions.

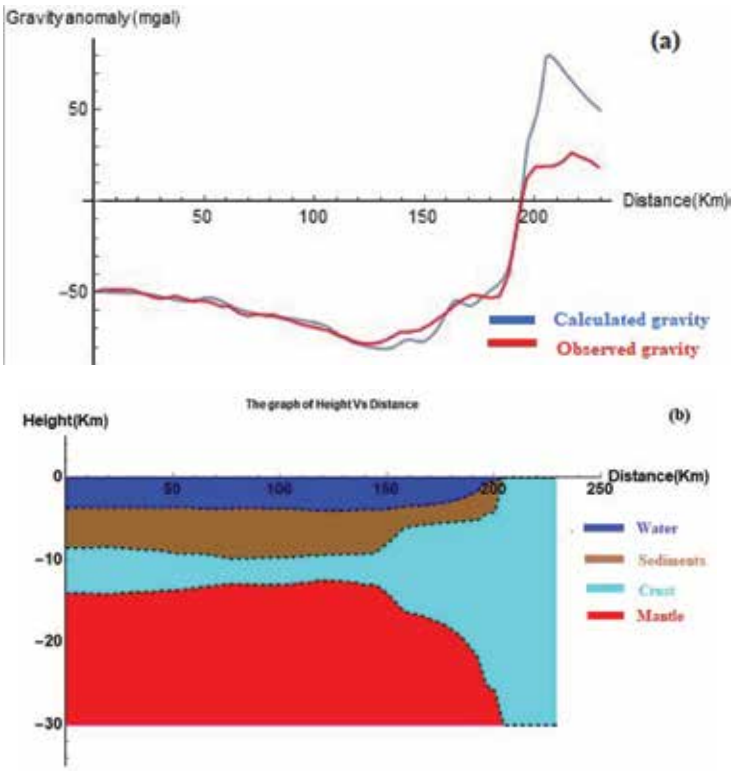

Figure 8. (a) Comparison between the observed free air gravity anomaly and the calculated gravity anomaly along the Profile A1-A for the Model A, using the densities of basement and mantle as 2.78g/cm^3 and 3.38g/cm^3 respectively. (b) Derived shallow structure in Model A.

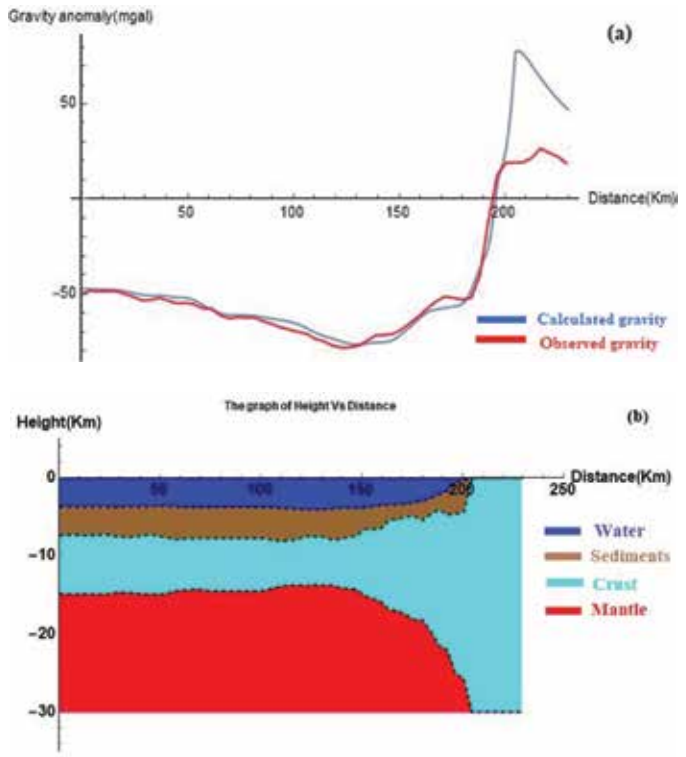

Figure 9. (a) Comparison between the observed free air gravity anomaly and the calculated gravity anomaly along the profile A1-A for the Model B, using the densities of basement and the mantle as 2.75 g/cm^3 and 3.3 g/cm^3. (b) Derived shallow structure in Model B.

CONCLUSIONS

Observing the structure of the Mohorovićič discontinuity and the sedimentary thickness, the primary conclusion that can be made is that off shore north eastern area are in rich in sediments accumulation, with average thickness around 6-8 Km. The Mohorovićič discontinuity below the water surface was found to be around 12-14 km along the A-A1 line, with an average crustal thickness of about 4.5 km.

ACKNOWLAEDGMENT

Authors wish to acknowledge The University of Sri Jayewardenepura for providing financial support under the research grant no. ASP/01/RE/SCI/2018/16. Special Gratitude to Petroleum Resources Development Secretariat for providing required data and facilities to conduct the research successfully.

Compliance with Ethical Standards

The authors declare that they have no conflict of interest and adhere to copyright norms.

REFERENCES

Baillie, B., Liyanaarachchi, D. and Jayaratne, M., 2002. A new Mesozoic sedimentary basin, offshore Sri Lanka. Petromin, 28(4), 53-57.

Chandra, K., Philip, P., Sridharan, P., Chopra, V., Rao, B. and Saha, P., 1991. Petroleum source-rock potentials of the Cretaceous transgressive-regressive sedimentary sequences of the Cauvery Basin. J. Southeast Asian Earth Sciences, 5(1-4), 367-371.

Gamage, S.S.N., Ratnayake, R.M.T.S., Senadhira, A.M.A.D.M., Weerasinghe, D.A. and Waduge, V.A., 2018. Radioactive and non-radioactive element analysis of Dorado gas discovery of Sri Lanka and their influence on natural environment. J. Tropical Forestry and Environment, 8(1), 55-63.

Kularathna, E.K.C.W., Pitawala, H.M.T.G.A. and Senarathne, A., 2015a. Gondwana Breakup and Development of Sedimentary Basins in Sri Lanka.Proceedings of the 31st technical session of Geol. Soc. of Sri Lanka, p.6.

Kularathna, E.K.C.W., Pitawala, H.M.T.G.A., Senaratne, A., Senevirathne, B.S.M.C.K. and Weerasinghe, D.A., 2015b. Forced-fold structures in the Mannar Basin, Sri Lanka: modes of occurrence, development mechanism and contribution for the petroleum system. J. Geol. Soc. Sri Lanka, 17, 53-63.

Lowrie, W., 2007. Fundamentals of geophysics.2nd ed. Cambridge University press.

Premarathne, D.M.U.A.K., Suzuki, N., Ratnayake, N.P. and Kularathne, E.K.C.W., 2013. A petroleum system in the Gulf of Mannar Basin, offshore Sri Lanka.Proceedings to 29th Technical Sessions of Geological Society of Sri Lanka, 9, p.12.

Rao, D.G., Bhattacharya, G.C., Ramana, M.V., Subrahmanyam, V., Ramprasad, T., Krishna, K.S., Chaubey, A.K., Murty, G.P.S., Srinivas, K., Desa, M. and Reddy, S.I., 1994. Analysis of multi-channel seismic reflection and magnetic data along 13 N latitude across the Bay of Bengal. Marine geophysical researches, 16(3), 225-236.

Rao, D.G., Krishna, K.S. and Sar, D., 1997. Crustal evolution and sedimentation history of the Bay of Bengal since the Cretaceous. Journal of Geophysical Research: Solid Earth, 102(B8), 17747-17768.

Ratnayake, A.S., Sampei, Y. and Kularathne, C.W., 2014. Stratigraphic responses to major depositional events from the Late Cretaceous to Miocene in the Mannar Basin, Sri Lanka.Journal of Geological Society of Sri Lanka, 16(1), 5-18.

Ratnayake, R.M.T.S., Gamage, S.S.N., Senadhira, A.M.A.D.M., Weerasinghe, D.A. and Waduge, V.A., 2017. NORM analysis of the reservoir sand section in the Dorado natural gas discovery, Mannar basin offshore Sri Lanka. J. Geol. Soc. India, 89(6), 683-688.

Reddy, M., 2001. Descriptive physical oceanography. Oxford and IBH Publishing Company, p.440.

Silva, K.C.C, Gamage, S.S.N. and Weerasinghe, D.A., 2018. Digitizing scanned seismic sections of the southern and North Eastern Indian Ocean Regions Adjoining Sri Lanka. In: 34th Technical Sessions of Institute of Physics Sri Lanka. Colombo: Institute of Physics Sri Lanka, 51-57. http://www.ipsl.lk/index.php/publications/technical-sessions/18-publications/technical-sessions/241-volume-34-2018.)

Smithson, S.B., 1971. Densities of metamorphic rocks.Geophysics, 36(4), 690-694.

Talwani, M., Worzel, J.L. and Landisman, M., 1959. Rapid gravity computations for two-dimensional bodies with application to the Mendocino submarine fracture zone. J.Geophys. research, 64(1), 49-59.

Received on: 11.12.18; Revised on: 5.2.19; Accepted on: 20.3.19

J. Ind. Geophys. Union (May 2019)
v.23, no.3, pp: 223-237

The scenario based seismic risk assessment in Gandhinagar city (Gujarat), India

Akash Solanki* and Kapil Mohan

Institute of Seismological Research, Knowledge Corridor, Raisan, Gandhinagar-382007, Gujarat, India
*Corresponding author: akash.solanki21@gmail.com

ABSTRACT

The quantification of the seismic risk and the loss has to be prioritized in important cities of India for future structural planning. The present study has been conducted to estimate the seismic loss, using different seismic scenarios, in the economically important sector 21 of the Gandhinagar city, Gujarat. Attenuation relation based four hazard scenarios (magnitudes of Mw 6.0 and Mw 6.5 at a focal depth of 15 km and 10 km each) and an IS code based hazard scenario are used for loss estimation. A significant increase of seismic loss (maximum increase of 47% in total losses) when magnitude alone is increased from Mw 6.0 to Mw 6.5, while only a slight increment is seen (maximum increase of 13.39% in total losses), when focal depth alone is decreased from 15 km to 10 km. The present study concludes that the variation in earthquake magnitude alone shows a significant effect in terms of damage probabilities on Masonry buildings, as compared to reinforced concrete frame buildings.

Keywords Seismic Risk assessment, SeisVARA, Seismic Hazard, Seismic Loss assessment, Vulnerability, Gandhinagar (Gujarat)

INTRODUCTION

The earthquakes are amongst the dangerous hazards, which are difficult to predict and control. They incurred substantial losses to life and property from time to time. Buildings, especially those present in the urban areas of India, have demonstrated their vulnerability to past earthquakes, which is a major concern considering the serious impact it can have on the lives of the occupants. The need for better risk estimation and disaster mitigation strategies have been highlighted by these events.

In the past, several seismic risk and loss assessment studies have been done around the globe. Such studies have been conducted in the Boston City (Brookshire et al., 1997), Alfama district of Lisbon (D'Ayala et al., 1997), Schmölln town in central Germany (Schwarz et al., 2002), Barcelona city (Lantada et al., 2009; Marulanda et al., 2013), Israel (Levi et al., 2010), 3 Municipalities in Kathmandu valley (Chaulagain et al., 2016), Cap-Haitien and Port-au-Prince in Haiti (Torres et al., 2016) and Manizales in Colombia (Salgado-Gálvez et al., 2017). In India too, such studies have been conducted for Mumbai (Sinha et al., 2008), Dehradun (Lang et al., 2012; Haldar et al., 2013) and Kolkata (Nath et al., 2014).

Globally, several seismic risk estimation tools have been developed. The National Institute of Building Sciences (NIBS), in collaboration with Federal Emergency Management Agency (FEMA), developed HAZUS software to facilitate earthquake hazard risk and loss estimation in the United States in 1997 (HAZUS-MH MR2, 2006). Hazus uses Capacity Spectrum Method (CSM) for calculating the fragility functions to enable loss estimation in case of earthquakes as a hazard. It was developed keeping in mind the U.S. building inventory and would require calibration for use in other countries.

Prasad et al., (2009) explored the use of socioeconomic clustering of urban habitat for seismic risk assessment of Dehradun city, India. Data obtained from satellite imagery and field surveys were used to develop building stock database. Based on the economic status of the occupants, they have defined 10 different classes of clusters which were indicative of the prevalent construction materials/ type/methods and were assumed to be affecting the overall seismic risk in Indian cities. They defined 34 different types of building for classification of the available building stock, based on the type of lateral load resisting system, the material of construction, no. of floors, roof type etc. and estimated their damage probabilities based on different intensity scales. They adopted the hazus methodology for loss estimation.

In collaboration with NORSAR (Norway) and the University of Alicante (Spain), the International Centre for Geohazards (ICG) developed Seismic Loss Estimation, using a Logic Tree Approach (SELENA) - a software which uses CSM for seismic risk estimation (Molina et al., 2010). The core of HAZUS methodology is adapted in SELENA, while also making use of a logic tree based computational approach enabling its user to account for uncertainties by assigning weightage factors to different input parameters. SELENA can be easily adjusted to suit the area of study by providing site specific inputs.

Haldar et al., (2013) have created a spreadsheet-based tool named 'SeisVARA' which can be used for comparison of different methodologies (in terms of hazard and vulnerability) available for seismic loss estimation on identical building inventory. SeisVARA is simple to

implement as it requires minimum inputs in terms of built-up area, building type, no. of floors etc. enabling greater adaptability to any region. In Indian conditions, this tool is very useful since the input requirements in other softwares are not easily available in the desired formats to enable wider applications. SeisVARA – Spectrum uses coefficients (ASCE-41, 2007) to modify the capacity curve for a Model Building Type (MBT). This enables direct calculation of target displacements eliminating the need for iterations while accounting for the non-linear behavior of that MBT. Hazus methodology is used in SeisVARA for seismic loss estimation.

Daniell et al., (2014) have reviewed over 80 open access softwares/tools available for risk assessment worldwide for different types of hazards, in order to provide guidance to users on selecting appropriate risk assessment tools for a specific purpose. This review highlights the strengths of about 31 open access softwares and also the challenges associated with their usage. It is noted from this review that many of these softwares do not possess easy to use interface and have difficult installation process. Most of these softwares were commonly using deterministic analysis. It was suggested in their review that, by enabling user-defined exposure and vulnerability, the applicability of these softwares could be improved. Also, only 3 such tools (Risk.iitb, SeisVARA and RADIUS) were found to be available specifically for Indian conditions.

Nanda et al., (2015) have reviewed some of the available seismic loss estimating tools while proposing a new methodology for seismic hazard scenario generation. In their review, the emphasis was on highlighting the underlying differences in the methodologies of these tools. From their review, it can be concluded that hazard and vulnerability models used in different seismic loss estimating tools vary in their methodologies which lead to varying estimates. They have proposed a seismic risk estimating software, 'SRAI.SA', which computes the response spectra based on attenuation relationships for a specific scenario earthquake. SRAI.SA is used to estimate losses on NIT Durgapur campus and ward 7 of Bhubaneshwar city, India. In comparison with losses computed using SeisVARA, a significant difference in their results is observed which may be due to the differences in hazard definition of these two softwares.

From the available literature, it is clear that many open access earthquake risk assessment tools are available globally which require some form of calibration for application in the Indian context. These freely available tools have their limitations in terms of applicability in areas where the critical inputs may not readily be available in the desired format. Since very few softwares were available for direct application in India, the spectrum based approach of the open source tool 'SeisVARA' was chosen for its simplicity, requirement of input information, and most importantly the vulnerability and hazard modules which are better suited for construction practices and building typologies generally found in India. Also, SELENA software is chosen for comparison of the loss methodology.

STUDY AREA

Gandhinagar (23.2156° N, 72.6369° E) is the state capital of Gujarat, India. While being India's second planned city after Chandigarh, Gandhinagar is proposed to be developed as one of the first few smart cities in Gujarat. Located at around 23 km from Ahmedabad City, the city of Gandhinagar covers approximately 182.3 km^2 area (including Gandhinagar Municipal Corporation area of 57 km^2 as per Census 2011). With the expansion and increase in the number of multi-storey buildings and important engineering structures in and around the city, population is on the rise and since Gandhinagar lies in seismic zone III, where the expected magnitude of earthquake is 6 (Sairam et al., 2011), single or multi-storey buildings in the city may be vulnerable to future earthquakes. Sector 21 of Gandhinagar city is one of the oldest sectors, apart from being one of the oldest commercial hubs in the city, consisting of buildings with different usage like a library, theatre, community center, residential, commercial and religious buildings which have different structural configurations, day and night time occupancy etc. Hence, Sector 21 (Figure 1) has been chosen for this study.

METHODOLOGY

The present work followed the methodology proposed by SeisVARA (Haldar et al., 2013) and the seismic risk is estimated for sector 21 of Gandhinagar City in order to compare the effects of magnitude, focal depth and spectral shape on the estimated losses by considering different hazard scenarios (IS code based and NDMA attenuation relationship based). Four different hazard scenarios (Mw 6.0 at a focal depth of 15 km and 10 km; Mw 6.5 at a focal depth of 15 km and 10 km) have been considered to construct the demand spectra using NDMA (2010) attenuation relationship. An IS code based demand spectra with site-specific surface Peak Ground Acceleration (PGA) of 0.20g is also constructed to study the variation in loss estimates with the change in the spectral shapes. The inputs required in SeisVARA-Spectrum include the hazard scenario, building stock information, day and night time population, replacement cost and cost of contents. The structural losses for the IS code based scenario using SeisVARA and SELENA are also compared where the input parameters are kept the same.

Model Building Types (MBTs)

The descriptions of the different MBTs based on which the buildings in the study area were classified are given in Prasad et al., (2009) and Haldar et al., (2013). MC3L1,

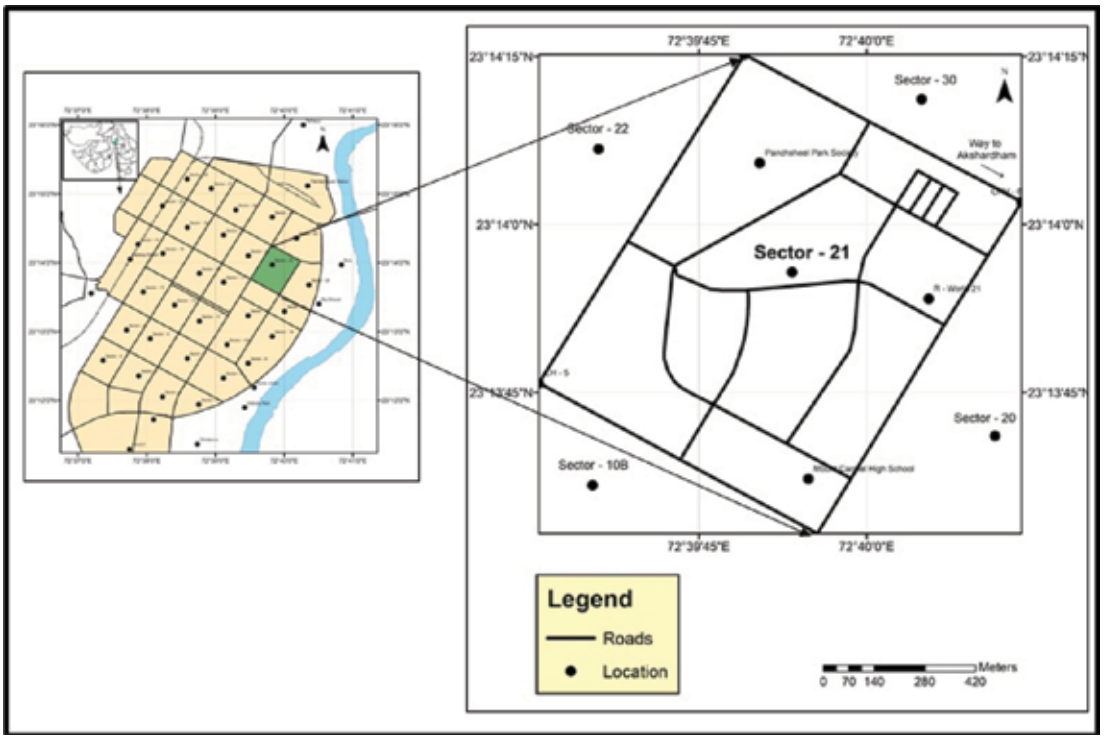

Figure 1. Location Map of sector 21, Gandhinagar City, Gujarat (India).

MC3L2, MC3M are considered to be load bearing masonry structures with flat RC roof and varying no. of floors (1, 2, and 3+ respectively). RC2L (LC) and RC2M (LC) are considered to be RC frame buildings with masonry infills where earthquake forces may have been considered in design but may not have been properly executed consisting of 1-3 floors for RC2L (LC) and 4-7 floors for RC2M (LC). RC3L (MC) and RC3M (MC) are considered to be RC frame buildings with masonry infills where design and execution are as per codal requirements consisting of 1-3 floors for RC3L (MC) and 4-7 floors for RC3M (MC). MC21 is considered to be a single floor load bearing structure having light sloping roof consisting of Galvanised Iron (GI) sheet.

Estimation of Direct Economic Losses

The direct economic loss consists of losses due to structural damage, non-structural damage, and contents damage. The total direct economic loss (structural and non-structural loss) due to damage to building of a given occupancy class was estimated using the following equation: (modified after HAZUS-MH MR2, 2006)

$$CBDC_i = \sum_{MBT=1}^{N}[PBA_{MBT,i} \times BAT_i \times \sum_{j=1}^{5}(P(PDG_j)_{MBT} \times LRB_j) \times BRC_{MBT}] \ldots\ldots (1)$$

Where, *CBDCi* = Cumulative Building Damage Cost in ith Occupancy Class,
$PBA_{MBT,i}$ = Percentage Built-up Area of an MBT in ith Occupancy Class,
BATi = Built-up Area Total of ith Occupancy class,
$P(PDG_j)_{MBT}$ = Probability of Probable Grade of Damage j in a MBT,
LRB_j = Loss Ratio of Building for Probable Grade of Damage j, (structural and non-structural damage),
BRC_{MBT} = Building Replacement Cost for an MBT.

Similarly, the total loss due to damage of contents in a given occupancy class was estimated as per the following: (modified after HAZUS-MH MR2, 2006)

$$CCCD_i = \sum_{MBT=1}^{N}[PBA_{MBT,i} \times BAT_i \times \sum_{j=1}^{5}(P(PDG_j)_{MBT} \times LRC_j) \times CC_i] \ldots\ldots (2)$$

Where, $CCCD_i$ = Cumulative Cost of Contents Damage in ith Occupancy Class,
$PBA_{MBT,i}$ = Percentage Built Area of a MBT in ith Occupancy Class,
BAT_i = Built-up Area Total of ith Occupancy,
$P(PDG_j)_{MBT}$ = Probability of Probable Grade of Damage j in a MBT,
LRC_j = Loss Ratio of Contents for Probable Grade of Damage j,
CC_i = Contents Cost of a MBT in ith Occupancy Class.

Estimation of Life Loss and Injuries

The probability of a Severity Level due to different damage states for a building type was calculated using the following equation: (modified after HAZUS-MH MR2, 2006)

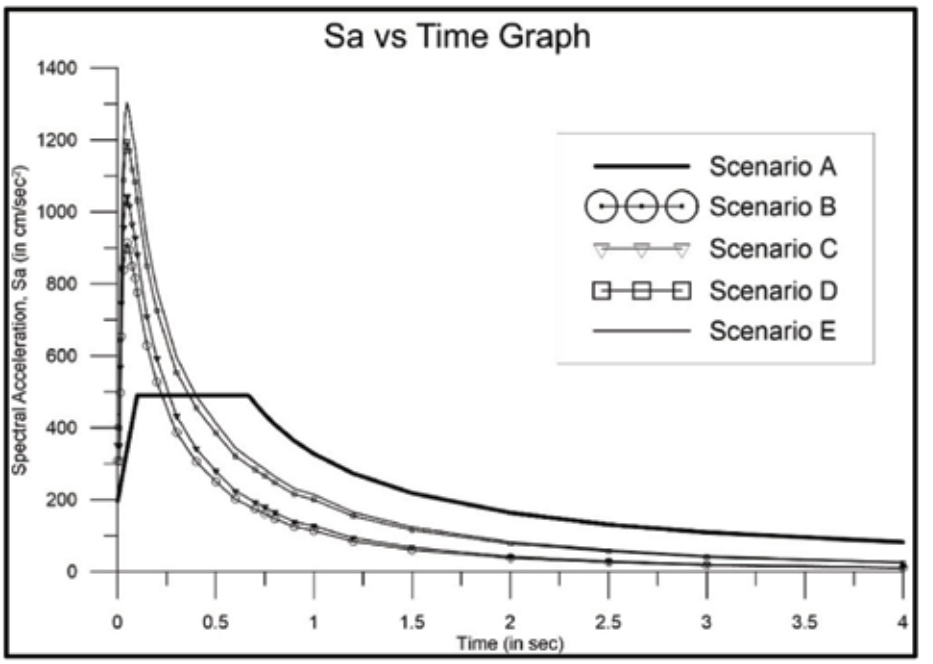

Figure 2. Response Spectra constructed for different hazard scenarios.

$$P(SL_i)_{MBT} = \sum_{j=1}^{n}[P(SL_i|PDG_j) \times P(PDG_j)_{MBT}] \ldots\ldots (3)$$

Where, $P(SL_i)_{MBT}$ = Probability of Severity Level i in an MBT,
$P(SL_i|\text{PDG}_j)$ = Indoor Casualty Rate of Severity Level i for Probable Damage Grade j, and
$P(PDG_j)_{MBT}$ = Probability of occurrence of Probable Damage Grade j in an MBT.

For an MBT, the total expected life loss or number of expected injuries is obtained by multiplying this probability with the total day and night time occupancy.

Seismic Hazard Scenarios

Determination of soil type is a major factor in the risk estimation. The Institute of Seismological Research (ISR) has conducted the Seismic Microzonation of Gandhinagar City and presented the detailed soil classification based on shear wave velocity (Sairam et al., 2011). The shear velocity in the study area ranges from 180-360 m/s which was classified as Type D (Stiff Soil) in accordance with the National Earthquake Hazard Reduction Program (NEHRP) provision and treated equivalent to the Medium soil as per IS 1893:2002. Hence, for this study, Type - II: Medium Soil was assumed for the entire study area.

The PGA values proposed by ISR, Gandhinagar for sector 21 through seismic microzonation (0.20g) is used in the current study (Mohan et al., 2018). The PGA was calculated for the scenario earthquake of magnitude Mw 6.0 along the East Cambay Fault. The IS code based demand spectra was calculated using this PGA (0.20g) and the IS 1893:2002 spectral shape for Type II: Medium Soil. Additionally, four different scenario earthquakes of magnitude Mw 6.0 and 6.5 along the East Cambay Fault with a Focal Depth (FD) of 10 km and 15 km with site coordinates 23.231578°, 72.664619° were considered to construct the response spectra on A-type rock based on attenuation relationship (Eq. 4) given by NDMA (2010).

$$\ln\left(\frac{S_a}{g}\right) = C_1 + C_2M + C_3M^2 + C_4r + \ln(r + C_6e^{C_7M}) + C_8\log(r)\,f_0 + \ln(\varepsilon) \ldots\ldots (4)$$

Where, Sa is the spectral acceleration, M is the moment magnitude and r is the hypocentral distance in km. The values of the coefficients C_1, C_2, C_3, C_4, C_5, C_6, C_7, C_8 and $\sigma(\varepsilon)$ for the Gujarat Region (NDMA, 2010) have been used in the present study. Since sector - 21 consists of soil class type D (Sairam et al., 2011), an amplification factor is needed to account for this change in soil class type. The Amplification Factor (AF) has been calculated using site coefficients given in BSSC (2009). For the sake of simplicity, the different hazard scenarios will be referred to in this paper as follows (See Figure 2):

IS code based spectral shape with site-specific surface PGA (0.20g) – Scenario A,
Mw = 6.0 with FD= 15 km and AF = 1.8179 – Scenario B,
Mw = 6.0 with FD= 10 km and AF = 1.7321 – Scenario C,
Mw= 6.5 with FD= 15 km and AF = 1.6169 – Scenario D,
Mw = 6.5 with FD = 10 km and AF = 1.510 – Scenario E.

Replacement Cost and Cost of Contents

In the present study, the structural and non-structural elements have been considered jointly in the estimation of

Figure 3. (**a**) The available Masonry buildings in the study area (**b**) The available RC buildings in the study area

losses due to building damage, since the data regarding the participation and effects of non-structural elements on the behavior of a structure subjected to earthquake forces are not yet available in the Indian context. Prasad et al., (2009) suggested a builder survey to estimate the replacement cost per square meter of the building floor area. In the present work, a similar approach was undertaken. It was found that the cost of construction for Reinforced Concrete (RC) frame building was approximately 10,000 INR/m^2 on an average while for Masonry building, this cost was approximately 12,500 INR/m^2 on an average in and around the study area and the same costs have been used in this study. The uncertainty about additional costs could not be incorporated in this study. Prasad et al., (2009) suggested that the different classes of occupancy have different cost of content in relation to the replacement cost. The same have been used in the present study.

BUILDING INVENTORY

In order to create the building footprint map of the study area, the satellite imagery available from Google Earth Pro (Satellite imagery date: 27/02/2016) was used. City Development Plan of sector 21, Gandhinagar and population data of the entire city was made available for this research by Gandhinagar Urban Development Authority (GUDA), which was useful in the creation of building inventory. Figure 3 (a) and (b) show some of the available buildings in the study area.

POPULATION ESTIMATION

As all buildings in the study area were not surveyed for population data, these details were extrapolated using the field survey data of 125 buildings in the study area. Building occupancy was found to increase with an increase in the number of floors. The government agency (GUDA) data shows that total population of sector 21, Gandhinagar is 6738 while the estimated night time population by extrapolation using the field survey data is 6264.

DAMAGE STATES

For Masonry construction, the damage state thresholds proposed by Kappos et al., (2006) while for RC construction, the damage state thresholds are defined based on HAZUS-MH MR2 (2006) have been used. Conditional probability equation (Eq. 5) proposed by Kircher et al., (1997) has been used to calculate the damage probabilities for different damage grades for respective MBTs.

$$P[ds|S_d] = \emptyset\left[\frac{1}{\beta_{ds}}\ln\left(\frac{S_d}{S_{d,ds}}\right)\right] \ldots\ldots\ldots\ldots (5)$$

where, $\overline{S}_{d,ds}$ is the median value of spectral displacement at which the building reaches the threshold of damage state, ds, β_{ds} is the standard deviation of the natural logarithm of spectral displacement for damage state, ds, S_d is the performance point for the considered MBT and ϕ is the standard normal cumulative distribution function.

RESULTS AND DISCUSSION

Based on the data collected on the field, a database comprising 650 buildings was created with information on the number of stories, MBT, latitude, longitude, occupancy class etc. Some buildings such as the MLA quarters were not made part of this database. Details of the building inventory in sector 21, Gandhinagar are given in Table 1. The capacity curve parameters (Lang et al., 2012; Haldar et al., 2013) and the calculated Performance Point for the considered MBTs and hazard scenarios are given in Table 2.

When comparing the results obtained for various Scenarios using SeisVARA (see Table 3 and figure 5), it is observable that the Scenario E shows the highest amount

Table 1. Details of Building Inventory in sector 21, Gandhinagar

MBT Label	No. of Buildings	Total Floor Area (m^2)	No. of Occupants at day time	No. of Occupants at night time
MC3L1	61	7329	351	194
MC3L2	247	72779	1479	2551
MC3M	98	62309	1289	2454
RC2L (LC)	153	65678	3869	769
RC2M (LC)	76	48354	2996	229
RC3L (MC)	10	26823	2997	54
RC3M (MC)	3	11128	650	13
MC21	2	3557	550	0
Total	650	297958	14181	6264

Table 2. Capacity Curve parameters (Lang et al. 2012; Haldar et al. 2013) and the calculated performance points for differezt hazard scenarios.

MBT Label	Capacity Curve Parameters					Performance point S_{dp} (m) for different Hazard Scenarios				
	S_{ay}	S_{au}	S_{dy}	S_{du}	T_e	A	B	C	D	E
	m/sec²	*m/sec²*	*m*	*m*	*sec*					
MC3L1	1.962	2.453	0.001	0.008	0.16	0.006	0.011	0.013	0.025	0.025
MC3L2	1.57	2.158	0.003	0.015	0.256	0.014	0.014	0.016	0.025	0.029
MC3M	1.57	2.158	0.003	0.015	0.256	0.014	0.014	0.016	0.033	0.029
RC2L (LC)	0.981	2.207	0.003	0.034	0.35	0.027	0.018	0.021	0.037	0.038
RC2M (LC)	0.814	1.844	0.007	0.05	0.566	0.052	0.022	0.024	0.033	0.041
RC3L (MC)	0.981	2.207	0.003	0.034	0.35	0.027	0.018	0.021	0.037	0.038
RC3M (MC)	0.814	1.844	0.007	0.05	0.566	0.052	0.022	0.024	0.02	0.041
MC21	1.962	2.453	0.001	0.008	0.162	0.006	0.011	0.013	0.025	0.025

S_{ay} - Spectral acceleration at yield point, in meter per second squared
S_{au} - Spectral Acceleration at ultimate point, in meter per second squared
S_{dy} - Spectral displacement at yield point, in meters
S_{du} - Spectral Displacement at ultimate point, in meters
T_e - Effective fundamental period of the single degree of freedom model of the structure, in seconds

of losses (249.24 crores) while the Scenario B shows the lowest (159.5 crores). For comparison of the estimated total direct economic losses, if Scenario A results are kept as a benchmark, scenario B shows a decrease of 22.61%, Scenario C shows a decrease of 12.25%, Scenario D shows an increase of 13.76% and Scenario E shows an increase of 20.93%.

From Table 3 it is observed that for scenario A, losses are estimated at INR 206.1 crores, while the usage of NDMA attenuation relationship based spectra estimate the losses at INR 159.5 crores (scenario B), INR 180.85 crores (scenario C), INR 234.45 crores (scenario D) and INR 249.24 crores (scenario E). The results indicate that an increase in the earthquake magnitude alone from Mw 6.0 to Mw 6.5 significantly increase the total loss estimates (maximum increase of 47%). A small increase (maximum increase of 13.39%) in total losses can also be observed when only the focal depth is decreased from 15 km to 10 km.

To obtain parity of results, structural losses are computed using SELENA software considering the same input parameters for Scenario A which estimate the losses at 148.1 crores. SeisVARA estimated the structural losses

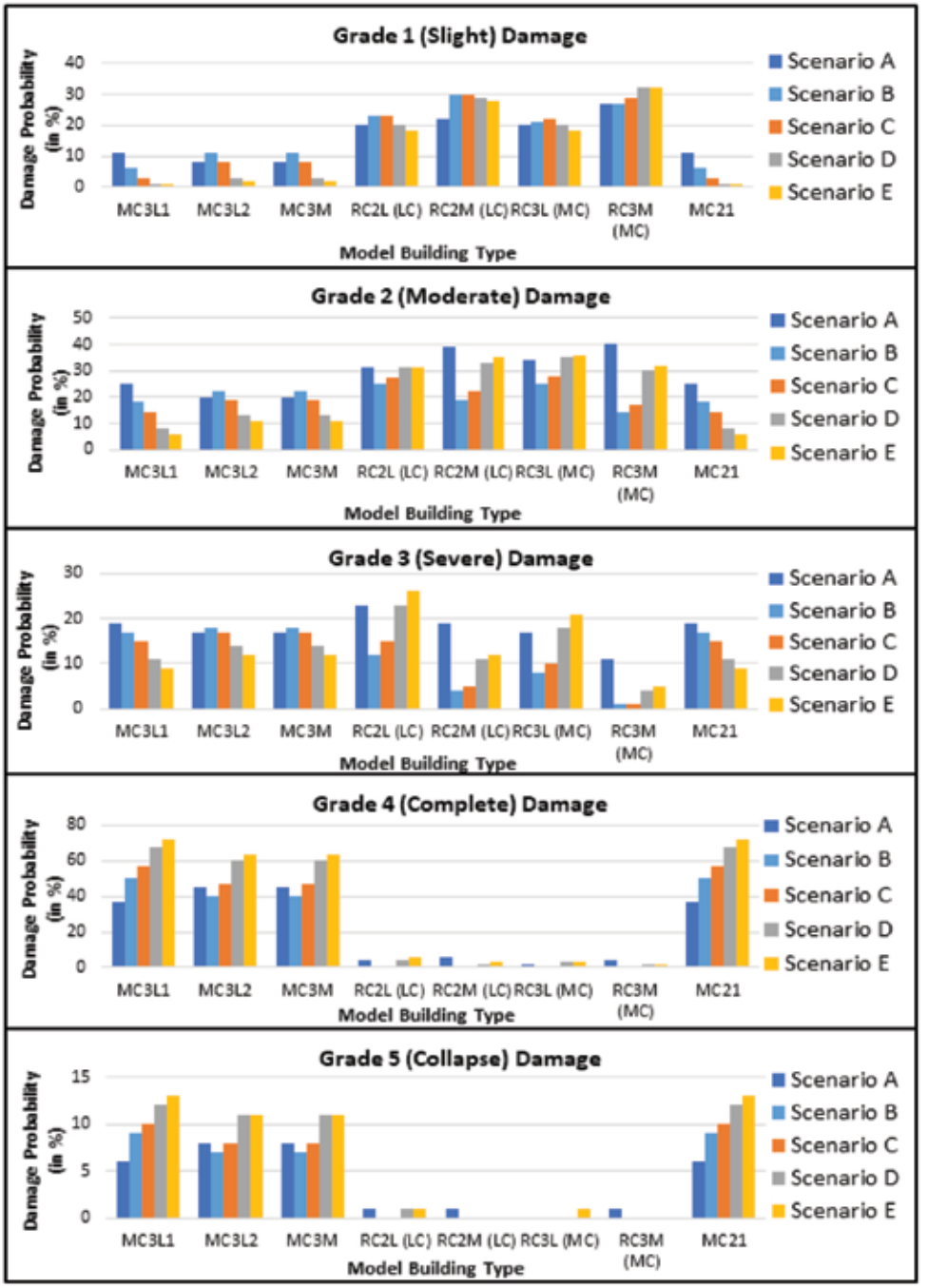

Figure 4. Comparison of Damage Grade Probabilities for different hazard scenarios

at 145.8 crores for Scenario A which shows that there is only 1.58% variation between the results obtained using the two different softwares.

In the case of masonry buildings, an increase in the magnitude of earthquake from Mw 6.0 to Mw 6.5 leads to significant increase (up to 34.84%) in losses due to these buildings while a decrease in the focal depth from 15 km to 10 km yields slight increase (up to 12%) in losses due to masonry buildings.

When considering the effects of magnitude alone, it is observed from fig. 4 that the damage probabilities decrease for Masonry buildings for damage grades 1, 2, and 3, while they increase significantly for damage grade 4 (maximum increase of 20%) when the magnitude is increased from Mw 6.0 to Mw 6.5. Grade 5 damage shows a slight increase with an increase in magnitude from Mw 6.0 to Mw 6.5 for masonry buildings. Considering the effects of focal depth alone, it is observable from fig. 4 that for masonry

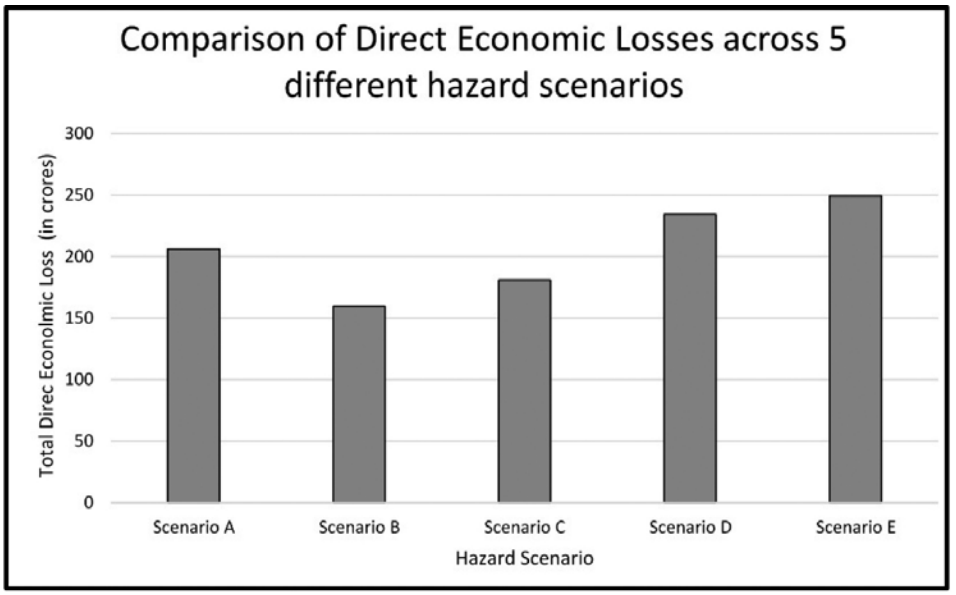

Figure 5. Comparison of Losses using different hazard scenarios.

Table 3. Comparison of estimated losses based on different hazard scenarios

Loss	Scenario A	Scenario B	Scenario C	Scenario D	Scenario E
Direct Economic Loss (in INR/m^2)	128672.25	107676.63	120572.88	152387.63	161881.25
Total Direct Economic Loss (in crores)	206.1	159.5	180.85	234.45	249.24
No. of Homeless People	3911	3517	3906	4688	4840
Day time Casualties	53	43	47	69	76
Night Time Casualties	64	56	64	87	88
Day time injuries	478	393	446	604	652
Night Time Injuries	565	505	576	750	776
Total day time population	14181	14181	14181	14181	14181
Total night time population	6264	6264	6264	6264	6264
Total losses due to Masonry buildings (in crores)	144.08	135.43	151.65	182.61	189.13
Total losses due to RC buildings (in crores)	62.02	24.13	29.2	51.84	60.11

buildings the damage probabilities tend to decrease slightly for damage grades 1, 2, and 3 while a small increase is observable in damage probabilities of grades 4 and 5 when the focal depth is decreased from 15 km to 10 km.

In the case of RC frame buildings, when the effects of magnitude alone are considered, it is observed from figure 4 that the damage probabilities of damage grade 1, do not show much variation. However, for damage grades 2 and 3, an increase in damage probabilities is observable (maximum increase of 15%) when the magnitude is raised from Mw 6.0 to Mw 6.5. Grade 4 and 5 damage probabilities remain negligible for RC frame buildings across all hazard scenarios. Considering the effects of focal depth alone, it is observable from fig. 4 that for RC frame buildings the damage probabilities of damage grade 1 are similar across all hazard scenarios, while they tend to show a small increase in damage grades 2 and 3 (maximum increase of 3%) when focal depth is decreased from 15 km to 10 km. Damage probabilities of damage grades 4 and 5 remain negligible across all hazard scenarios for RC frame buildings.

It can be concluded that magnitude of earthquake alone can have significant effects on the damage probabilities, especially for masonry buildings. Variation in focal depth alone does not yield conclusive results.

The maps generated showing the distribution of damage probabilities of Grade 4 damage for all 5 scenarios are given in Figuress 6-10.

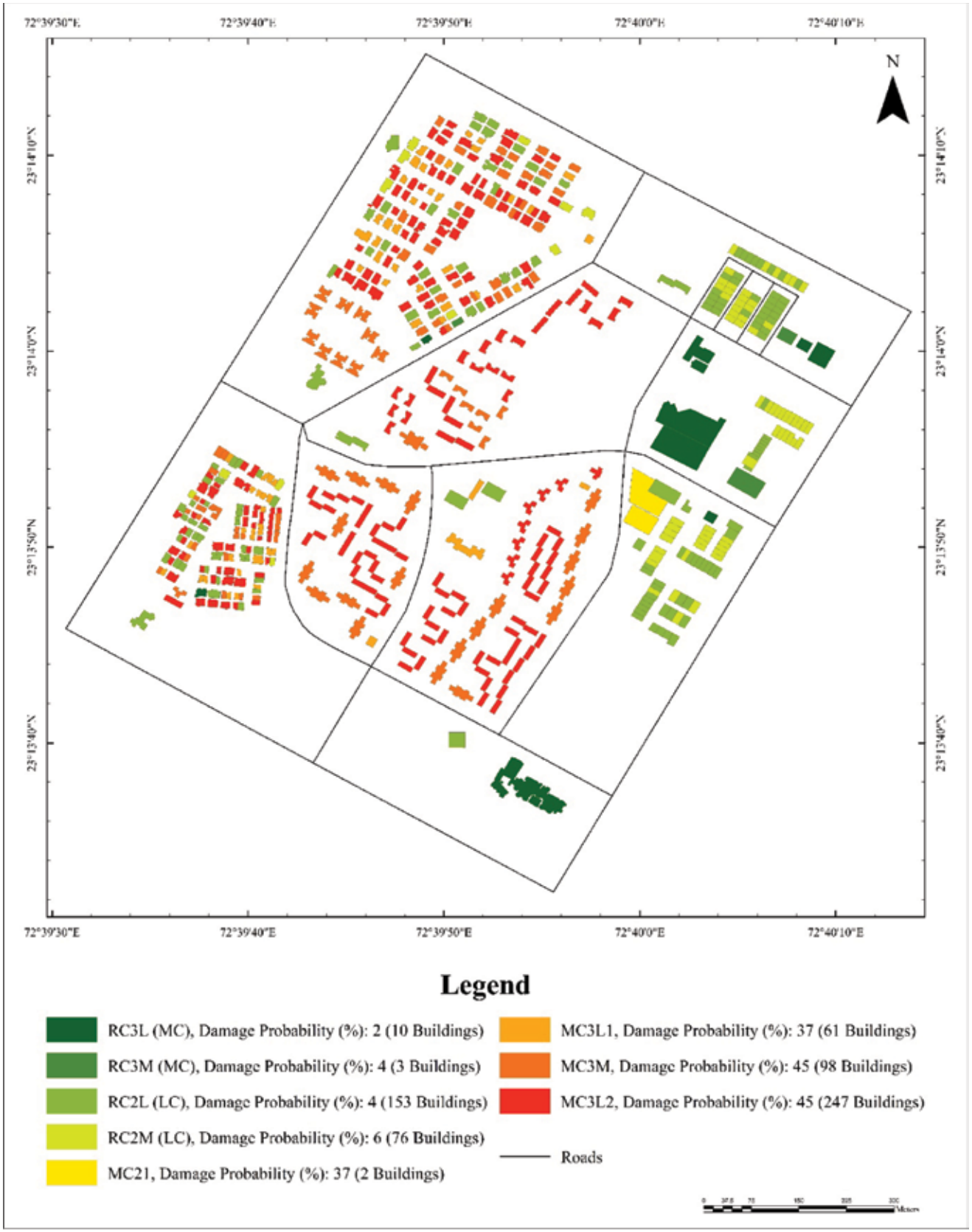

Figure 6. Grade 4 Scenario A

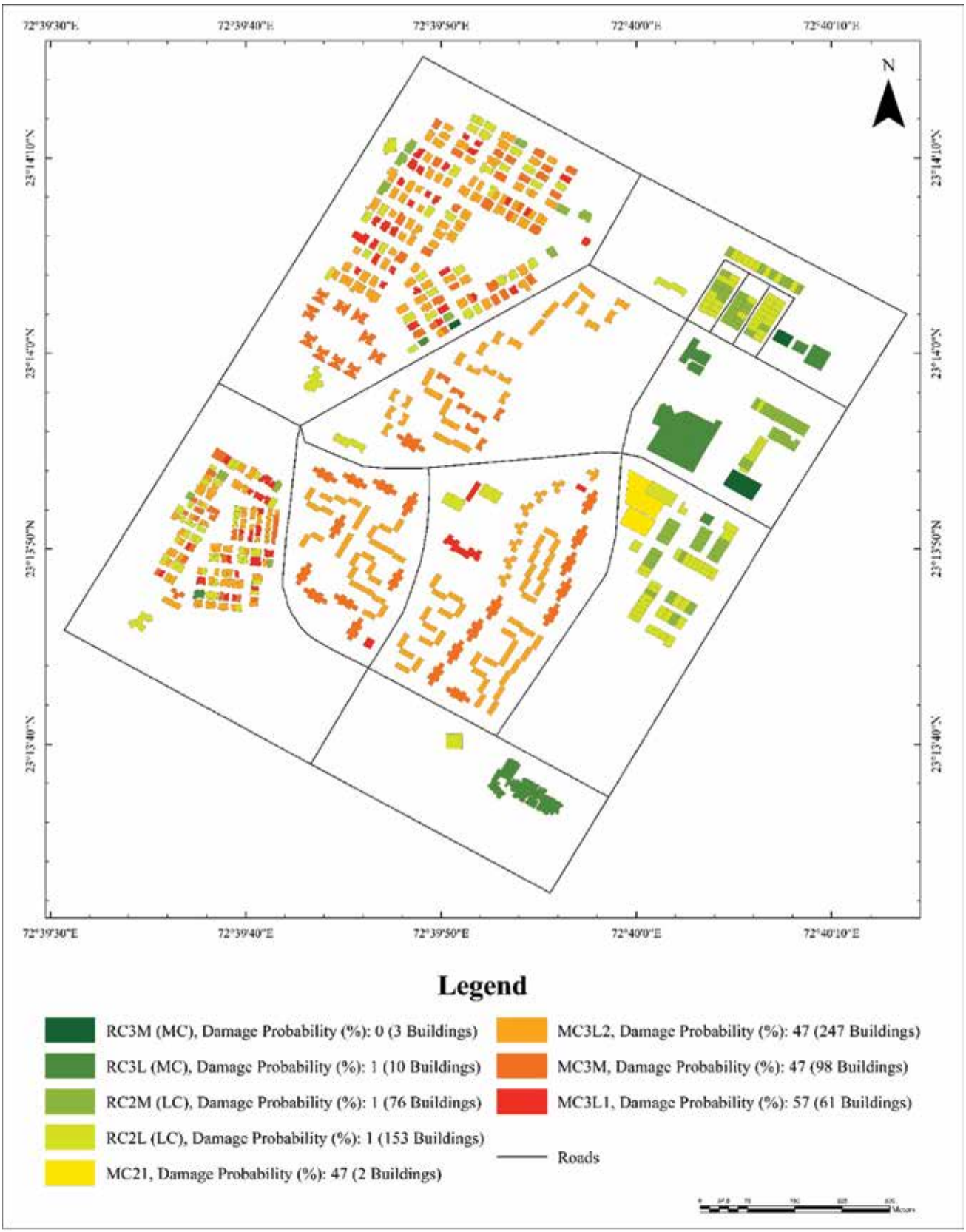

Figure 7. Grade 4 Scenario B

Figure 8. Grade 4 Scenario C

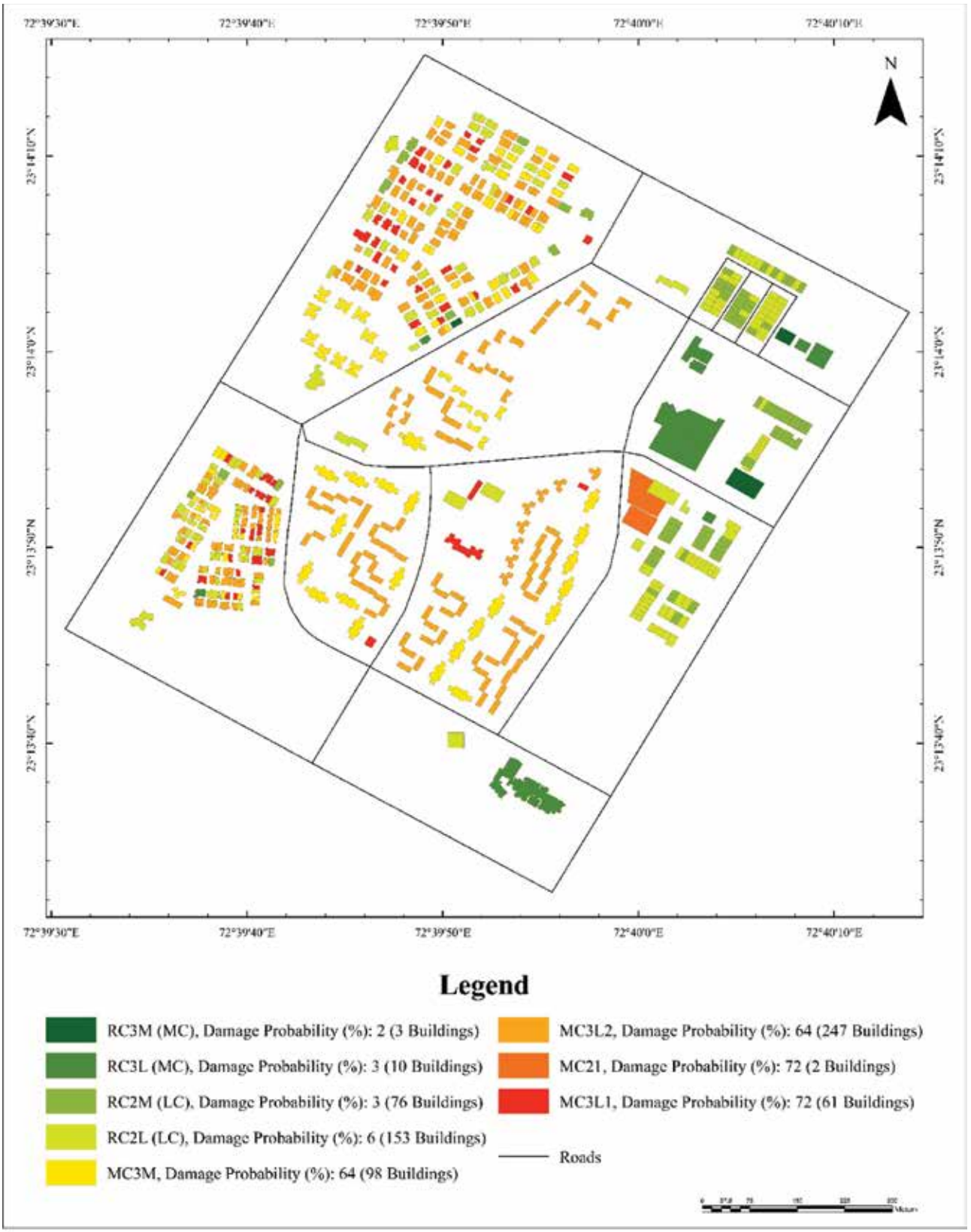

Figure 9. Grade 4 Scenario D

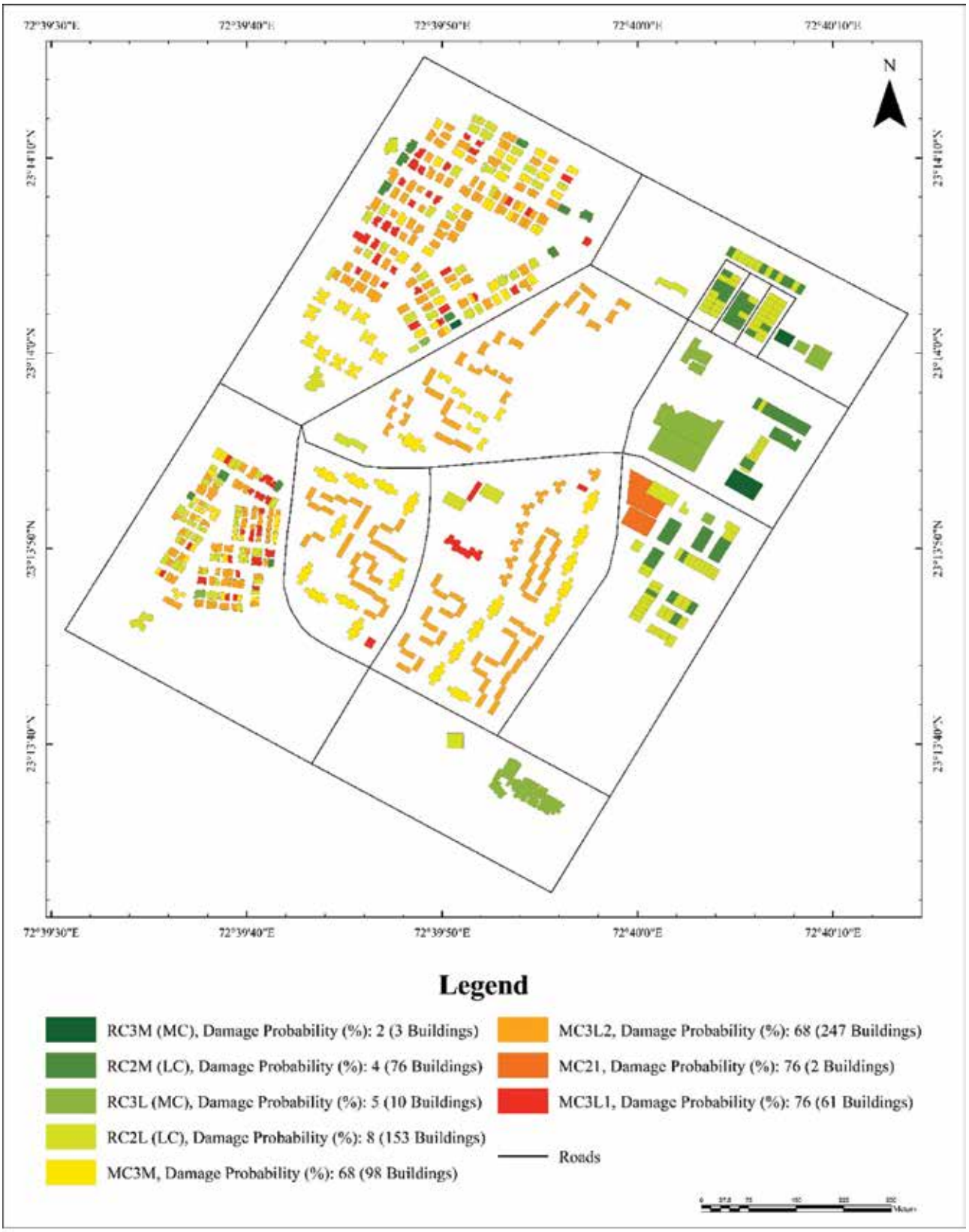

Figure 10. Grade 4 Scenario E

CONCLUSION

An attempt has been made in this study to estimate the seismic risk posed to the building stock and the population of sector 21, Gandhinagar, in order to compare the effects of magnitude, focal depth, and spectral shape on the estimated losses by considering 5 different hazard scenarios. Most of the buildings found in the study area were either G+1 or G+2. The results clearly indicate that the selected hazard scenario parameters can significantly affect the seismic risk in an area even for the same loss estimation methodology especially if the area under study comprises of mostly similar building typologies. The present study concludes that for sector 21 (Gandhinagar), a significant increase is observed in the losses when the earthquake magnitude is increased from Mw 6.0 to Mw 6.5 (total losses increased by 47% at 15 km focal depth and 37.82% at 10 km focal depth) and focal depth is reduced from 15 km to 10 km (total losses increased by 13.39% for Mw 6.0 and and 6.31% for Mw 6.5), indicating that the effects of change in earthquake magnitude on the total losses is more at 15 km focal depth in comparison to 10 km depth. The SeisVARA software also obtains parity with the estimates given by SELENA for the IS code based hazard scenario A. The present study also concludes that for Sector 21, Gandhinagar, variations in earthquake magnitude show a greater effect in terms of damage probabilities on masonry buildings as compared to RC frame buildings (even though both types of building contribute almost equally to the building footprint area), which in turn largely govern the overall losses. Such studies can help in disaster mitigation by identifying and quantifying the risk and potential losses.

ACKNOWLEDGEMENT

Authors are thankful to the Director General and Director, ISR for their permission and encouragement to publish this work.

Compliance with Ethical Standards

The authors declare that they have no conflict of interest and adhere to copyright norms.

REFERENCES

ASCE-41 (American Society of Civil Engineering), 2007. Seismic rehabilitation of existing buildings (ASCE/SEI 41-06). American Society of Civil Engineers Reston, Virginia.

Brookshire, D.S., Chang, S.E., Cochrane, H., Olson, R.A., Rose, A. and Steenson, J., 1997. Direct and indirect economic losses from earthquake damage. Earthq. Spectra 13, 683–701.

BSSC (Building Seismic Safety Council), 2009. NEHRP Recommended Seismic Provisions for New Buildings and Other Structures (FEMA P-750), 2009 edition, Report prepared for the Federal Emergency Management Agency (FEMA), National Institute of Building Sciences, Washington, D.C.

Census of India, 2011. Office of Registrar General and Census Commissioner, New Delhi, India.

Chaulagain, H., Rodrigues, H., Silva, V., Spacone, E. and Varum, H., 2016. Earthquake loss estimation for the Kathmandu Valley. Bull. Earthq. Eng. 14, 59–88.

Daniell, J., Simpson, A., Murnane, R., Tijssen, A., Nunez, A., Deparday, V., Gunasekera, R., Baca, A., Ishizawa, O. and Schäfer, A., 2014. Review of open source and open access software packages available to quantify risk from natural hazards. Wash. DC World Bank Glob. Facil. Disaster Reduct. Recovery.

D'Ayala, D., Spence, R., Oliveira, C. and Pomonis, A., 1997. Earthquake loss estimation for Europe's historic town centres. Earthq. Spectra 13, 773–793.

Haldar, P., Singh, Y., Lang, D.H. and Paul, D., 2013. Comparison of seismic risk assessment based on macroseismic intensity and spectrum approaches using 'SeisVARA.' Soil Dyn. Earthq. Eng. 48, 267–281.

HAZUS-MH MR2, 2006. Multi-hazard loss estimation methodology. Earthquake model. Federal Emergency Management Agency, Washington, DC.

Indian Standard: 1893, 2002. Criteria for earthquake resistant design of structures - General provisions and buildings (Part - 1). Bureau of Indian Standards, New Delhi

Kappos, A.J., Panagopoulos, G., Panagiotopoulos, C. and Penelis, G., 2006. A hybrid method for the vulnerability assessment of R/C and URM buildings. Bull. Earthq. Eng. 4, 391–413.

Kircher, C.A., Nassar, A.A., Kustu, O. and Holmes, W.T., 1997. Development of building damage functions for earthquake loss estimation. Earthq. Spectra 13, 663–682.

Lang, D.H., Singh, Y. and Prasad, J., 2012. Comparing empirical and analytical estimates of earthquake loss assessment studies for the city of Dehradun, India. Earthq. Spectra 28, 595–619.

Lantada, N., Pujades, L.G. and Barbat, A.H., 2009. Vulnerability index and capacity spectrum based methods for urban seismic risk evaluation. A comparison. Nat. Hazards 51, 501.

Levi, T., Tavron, B., Katz, O., Amit, R., Segal, D., Hamiel, Y., Bar-Lavi, Y., Romach, S. and Salamon, A., 2010. Earthquake loss estimation in Israel using the new HAZUS-MH software: preliminary implementation. Minist. Natl. Infrastruct. Geol. Surv. Isr. Jerus. Isr.

Marulanda, M.C., Carreno, M.L., Cardona, O.D., Ordaz, M.G. and Barbat, A.H., 2013. Probabilistic earthquake risk assessment using CAPRA: application to the city of Barcelona, Spain. Nat. Hazards 69, 59–84.

Mohan, K., Rastogi, B.K., Pancholi, V. and Gandhi, D., 2018. Seismic hazard assessment at micro level in Gandhinagar (the capital of Gujarat, India) considering soil effects. Soil Dyn. Earthq. Eng. 109, 354–370.

Molina, S., Lang, D. and Lindholm, C., 2010. SELENA–An open-source tool for seismic risk and loss assessment using a logic tree computation procedure. Comput. Geosci. 36, 257–269.

Nanda, R.P., Paul, N.K., Chanu, N.M. and Rout, S., 2015. Seismic risk assessment of building stocks in Indian context. Nat. Hazards 78, 2035–2051.

Nath, S., Adhikari, M., Devaraj, N. and Maiti, S., 2014. Seismic vulnerability and risk assessment of Kolkata City, India. Nat. Hazards Earth Syst. Sci. Discuss. 2, 3015–3063.

NDMA (National Disaster Management Authority), 2010. Development of probabilistic seismic hazard map of India (Technical Report).

Prasad, J., Singh, Y., Kaynia, A.M. and Lindholm, C., 2009. Socioeconomic clustering in seismic risk assessment of urban housing stock. Earthq. Spectra 25, 619–641.

Sairam, B., Rastogi, B., Aggarwal, S., Chauhan, M. and Bhonde, U., 2011. Seismic site characterization using Vs30 and site amplification in Gandhinagar region, Gujarat, India. Curr. Sci. 754–761.

Salgado-Gálvez, M.A., Bernal, G.A., Zuloaga, D., Marulanda, M.C., Cardona, O.D. and Henao, S., 2017. Probabilistic seismic risk assessment in Manizales, Colombia: Quantifying losses for insurance purposes. Int. J. Disaster Risk Sci. 8, 296–307.

Schwarz, J., Raschke, M. and Maiwald, H., 2002. Seismic risk studies for Central Germany on the basis of the European Macroseismic Scale EMS-98. Presented at the Proc. 12th European Conference on Earthquake Engineering.

Sinha, R., Aditya, K. and Gupta, A., 2008. GIS-based urban seismic risk assessment using RISK. iitb. ISET J. Earthq. Technol. 45, 41–63.

Torres, Y., Molina, S., Martínez-Cuevas, S., Navarro, M., Martínez-Díaz, J., Benito, B., Galiana-Merino, J. and Belizaire, D., 2016. A first approach to earthquake damage estimation in Haiti: advices to minimize the seismic risk. Bull. Earthq. Eng. 14, 39–58.

Received on: 14.10.18; Revised on: 19.2.19; Accepted on: 12.3.19

J. Ind. Geophys. Union (May 2019)
v.23, no.3, pp: 238-248

Mount Kailas (Trans-Himalaya), Mantle plumes and Leucogranites

U. Raval

2-1-19/C St. 11, Surya Nagar Colony, Uppal, Hyderabad – 500 039, India
upen0106@gmail.com

ABSTRACT

Mt. Kailas, situated in theTrans-Himalayan region, stands close to the central part of the northernmost margin (NMM) on the northern side of Indian subcontinent. The NMM consists of high Himalaya (HH), Tethyan Himalaya (TH), Indus-Tsangpo Suture (ITS) and the Gangdese Batholith (GB) mountain series. The last one lies just north of the ITS margin and forms part of the southern Tibet. Mt. Kailas conglomerate, a term used by Gansser, also consists of a major leucogranite intrusion of early Miocene age (~10.1±1.4 Ma). From the study of paleo-positions of India, relative to the Kerguelen (Kg) and Reunion (Ru) mantle plumes, and mafic magmatic occurrences in the eastern and western sectors of the NMM, it is suggested that (a) Mt. Kailas seems to lie in the common zone of influence of the two plumes, and (b) thermal input from these mantle plumes, might also act as one of the prominent heat sources suggested earlier for the crustal anatexis or generation of the two-mica leucogranites. Leucogranite plutons are present in all these corridors, but their ages differ significantly, although they are associated with nearly similar process of generation. It further appears that the crust and mantle of the lithosphere under the NMM, has traversed over both of these mantle plumes, Kg in the east and Ru in the west, during their pre-outburst phases. Besides, the domal topography in and around the Mt. Kailas, seems to be a nodal point for the nearly radial drainage pattern over this region, consisting Indus, Satlej, Brahmputra, Karnali (or Ghagra) and Ganga rivers.

INTRODUCTION

In the central part of the northern most margin (NMM) of the Indian subcontinent and over a swell/uplift, stands the majestic Mt. Kailas with its entire splendor (Figure 1). It lies almost on the northern flank of the Indo-Tsangpo suture (ITS) and is considered to be one of the major domes of the Gangedese mountain chain or batholith. Mt. Kailas is located at 31.0675°N; 81.3119°E, which is close to Manasarovar (at a distance of ~47 km) and the Rakshastal (at a distance of ~45km) lakes, in the vicinity of central part of the NMM. Prof. A. Gansser, a well known Himalayan geologist, had made an interesting observation earlier about the Mt. Kailas, "While travelling from the Tethys Himalaya of the Kumaun to further northwards into the Tibet, we have so far not met with the northern border of the Himalaya, but got involved in the more intriguing problems of the huge exotic thrust masses. Only on reaching the Kailas ranges in the Trans –Himalaya, it became possible to find some conclusive evidence for the northern limit." This would imply that he considered Mt. Kailas as the northern most end of the Himalaya.

Kailas and Indus headwater area is characterized by extensively faulted and metamorphosed late Cretaceous to mid-Cenozoic metasediments, which have been intruded by Cenozoic granitic rocks. The Paleozoic rocks represent offshore marine limestones, deposited before the subduction of the Tethys oceanic crust. Mt. Kailas thus appears to be a metasedimentary pendent, supported by massive granite at the base. It has further been intruded by young Cenozoic leucogranites of about ~10.1±1.4 Ma in age. As a result of anatexis and partial crustal melting, these discontinuos plutons occur in all the three corridors (High Himalaya, Tethys Himalaya and Gangdese mountain series) of the northern margin, but ages of these plutons generally increase as one move northward. Actually in this collision-subduction tectonic system, an interesting dynamics is in play due to underthrusting of the Indian continental lithosphere under Tibet upto ~ 31° N (Nabelek et al., 2009). Over the past 50 Ma, nearly 200-300 km of the Indian plate, has slipped beneath the Tibetan lithosphere. Thus, in order to understand the geological/geophysical/geodynamical evolution of this region, one may have to gradually retract (i.e. move backward in time) the position of the Indian plate to the further south. Since Mt. Kailas is a major domal (or uplifted) structure, it would require thermal input also at the depth. Using the paleo-positions and mafic magmatic occurances as stated above, this study shows that there is a strong plausibility of Kg and Ru plumes thermally affecting the northern most margin of the Indian subcontinent and would have also contributed to the doming of Mt. Kailas and other nearby regions. As will be discussed later, the doming of Kailas possibly resulted into the radial drainage pattern of streams emanating from near the ITS and high Himalaya regions.

PALEO-POSITION OF THE STUDIED REGION

It is well known that the outbursts of the (i) Kerguelen mantle plume (Kg) resulted in the Large Igneous Province (LIP), consisting of the Rajmahal-Sylhet-Bengal traps at around 117 Ma (Baksi, 1994), and (ii) Reunion mantle

Figure 1. The magnificent Mount Kailas located over a major domal upwarp (uplift/swell).

plume near Broach, gave rise to the Deccan flood basalts (DFB) at ~ 65.5 Ma (Baksi, 1995). Further, the post-outburst phases of these two mantle plumes respectively caused the 90°E ridge in the Bay of Bengal, and the Laccadive-Maldive volcanic chain in the Arabian Sea. Period before the plume outburst has been termed as the pre-outburst phase, which is of main interest in this study and whether these pre-outburst phases were thermally active before the formation of these LIPs.

Studies of Klootjwick (1979) and Klootjwick et al. (1994) have given the paleopositions of the India for the past ~ 160 Ma and its northward journey. (see Figure 2 in Klootjwick et al., 1994), during which it first passed over the Kg mantle plume (49°S, 69°E) and then over the Ru mantle plume (21°S , 56°E). For the Kg plume, Curray et al., 1982 while discussing the origin of the 90° E ridge, have given the pre-outburst trace (or phase) of the Kg plume It trends in nearly WNW-ESE direction, which is also the approximate orientation of the NMM, and covers a distance from ~77°E to 90°E (Figure 2a). This study indicates that a large part of the eastern side of the NMM of Indian subcontinent has traversed over the Kg plume. On the western Indian side, Storey (1995) has given the paleopositions (at 200, 160, 130 and 100 Ma) of the Ru plume, with respect to India (Figure 2b). These paleoreconstructions of Storey (1995) imply that a significant part of the western side of NMM has 'effectively' straddled over the Ru plume. While considering the paleo-positions, one also needs to keep in mind that during its northward movement, India has also rotated first anticlockwise and then clockwise. Thus, both the eastern as well as the western sectors of the NMM, both have been affected by the Kg and Ru plume respectively, and there would be a central zone common to both the plumes. Mt. Kailas lies in this central zone and with regard to this location, it is interesting to note from the INDEPTH seismic study, that the Indian crust has underthrusted below the Tibet upto about 31°N. The issue whether the pre-outburst phases of the plumes were thermally effective, could be answered, if the signatures of the mafic magmatism of appropriate ages (i.e. during the pre-outburst phase), exists over the NMM.

PRE-OUTBURST PHASES AND MAFIC MAGMATISM

Some evidences of mafic magmatism attributable to the mantle plume activity in and around the northernmost margin of the Indian subcontinent, are discussed below.

Reunion Plume (Ru) and Western part of the NMM

On the basis of geochemical analysis (Nb/y and Zr/p) of the tectonized oceanic lithosphere (ophiolites) in an area between Kargil and Leh (Figure 3a, b), Sinha and Mishra (1992) have shown that most of these samples exhibit within-plate- basalt (WPB) characters (Figure 3b). They further infer that their results support the plume activity and consequent presence of seamounts. Plume activity seems to have apparently affected the Neo-Tethys between 75 and 100 Ma. From the petrophysical and geochemical analyses of the Maastrichtian Parh formations of Pakistan along the Tethys suture, McCormick (1991) found that a part of the volcanics belongs to ocean island basalt (OIB) category. The Nb-Zr discrimination plots strongly

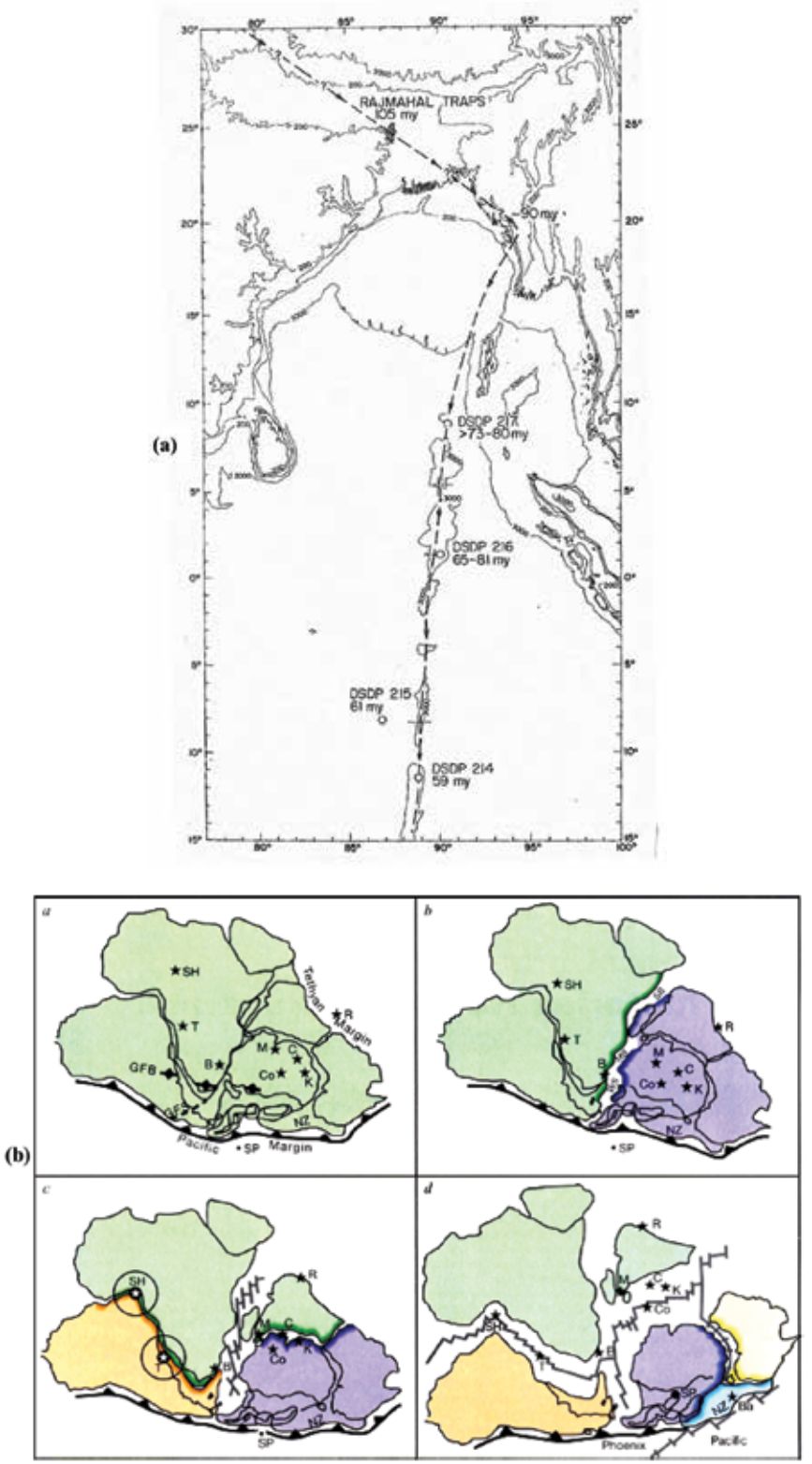

Figure 2. (a) Approximate. Pre-, syn-, and post- outburst traces of the Kerguelen mantle plume (after Curray et al., 1982). It is evident from this diagram that during the pre –outburst phase, the northern margin has traversed over the Kerguelen Plume affecting in particular the eastern side of the margin. (b) Paleopositions of the Reunion (Ru) mantle plume at 200 Ma (Figure a), 160 Ma (Figure b), 130 Ma (Figure c), and 100 Ma (Figure d) (after Storey, 1995). From these reconstructions it seems that the northern most margin (NMM) has passed over the Reunion.

corroborated their WPB nature and comparison of these volcanics with the Reunion and Deccan trap basalts, reveals that these were generated during the traverse of the Tethys slab over the Reunion plume. Further, from the analysis of the marine volcanic rocks (geochemical characteristics, Nd-Pb and Sr isotopic ratios and patterns of their incompatible elements) in the south Tethys suture zone in the Baluchistan province of Pakistan, Mahoney et al. (2002) suggested the WPB nature of their affinity, which may be related to the Ru mantle plume. Using the Ar-Ar method, their age was estimated to be ~ 73.5 – 72 Ma, which is much older than that of the Deccan traps. Hence, Mahoney et al. (2002) concluded that the 'Ru mantle plume was active much before the eruption of the Deccan traps. Shrivastava (1988) and Basu et al. (1993) have also confirmed the presence of pre-Deccan trap volcanic/alkaline formations in Rajasthan and Gujarat. In conformity, a significant disturbance at about 70 Ma in the region has also been reported by Sivaraman and Raval (1995).

Kerguelen Plume (Kg) and eastern part of the NMM

Zhu et al. (2005) have geochemically analysed the Mid-Cretaceous sandstones in the TIANBA region of the eastern Tethyan Himalaya. From the melt inclusions in the detrital Cr-rich spinels, Zhu et al. (2005) were also able to infer the magma composition and their source parameters, which strongly indicated that the plume activity would have been responsible for these Cr-rich spinels (Figure 3c). Further, from the paleo-reconstructions, he also concluded that interaction of the Kg plume with the region lying between southeast Tibet and Higher Himalaya, may have been the primary cause. Such observations obviously imply that the NMM may have been thermally affected by the Kg plume.

Besides, petrogenesis of the earliest Cretaceous mafic rocks of the CONA region (see Figure 1 in Zhu et al., 2008), which are widely exposed in the eastern Tethyan Himalaya in the southern part of Tibet, indicates an interaction between a mantle plume and the overlying lithosphere. Although association of the Kg plume and east Gondwanaland has been a matter of some conjecture, geochemical similarities between the basalts of the CONA region and those from the Kg-plume, suggest that for the generation of the CONA mafic rocks, an incubating Kg-plume model seems to be the main plausibility, which may have begun early i.e. during late Jurrasic or early Cretaceous. It is understood that a progressive thinning of the lithosphere under the East Gondwana land, could be associated with CONA formation. While discussing the interaction between Kg plume and overlying continental lithosphere, Kent et al., 2002 have indicated that beneath the continent, melting of a plume head may be inhibited by the presence of a thick (~ 125 km) mechanical boundary layer, which must be thinned and removed by conductive heating and melt injection, before significant basalt production.

In an another study Zhu et al. (2007) have brought attention to the SANGXUI mafic rocks in the eastern part of the central segment of theTethyan Himalaya (see figure 1 a, b in Zhu et al. 2007), which paleo-geographically belong to the northeast margin of greater India. On the basis of the petrogenesis, these Sangxui formations have been attributed to the interaction between Kerguelen hotspot and the lithosphere of the north eastern margin of greater India at ~ 133 Ma. These volcanic formations also consist of alkaline rocks and their ages overlap with the early stage of rifting between southwest Australia and greater India.

Using U-Pb zircon ages, obtained by sensitive high resolution ion microprobe (SHRIMP) and laser ablation inductively coupled plasma mass spectrometer (LA- ICP-MS) for the COMEI rocks in the south Tibet, Zhu et al. (2008) have also delineated presence of a ~132 Ma old volcanics. These COMEI igneous rocks, consists of basaltic lavas, dikes and gabbroic intrusions, together with subordinate layered ultramafic intrusions, which are exposed in the Tethyan Himalaya (see figure 1a,b in Zhu et al., 2007). In fact Zhu et al. (2008) infer that these intrusions form a part of a major volcanic eruption, which they termed as the Comei-Bunbury Large Igneous Province (LIP), and indicate that this magmatism was likely to have been caused by the Kerguelen plume, which initiated during early Cretaceous.

The above findings of mafic rocks from the eastern sectors of the NMM and belonging to the pre-outburst phases, suggest that probably owing to the very difficult terraines, the central and western parts of the NMM might have not been surveyed in requisite detail as yet; and there appears a possibility of finding more mafic occurrences related to the Kg and Ru plumes. Thus, the Paleopositions and rotation of India over the past 200 Ma and the evidences of mafic magmatism along the NMM, having ages much older than the Rajmahal (on the eastern side) and Deccan traps (on the western side) along the NMM, clearly imply that: (i) during their pre-outburst phases, these plume were thermally active, and (ii) both sides of the NMM, would have been significantly affected by the Kg and Ru mantle plumes. This may also mean that there could be an upward transfer of the thermal input (heat) from these plumes (Brown et al., 1996) which in turn, would have supplemented the other plausible heat sources, suggested earlier (Molnar et al., 1983; Nabelek and Liu, 2004) for crustal anatexis and generation of the leucogranites.

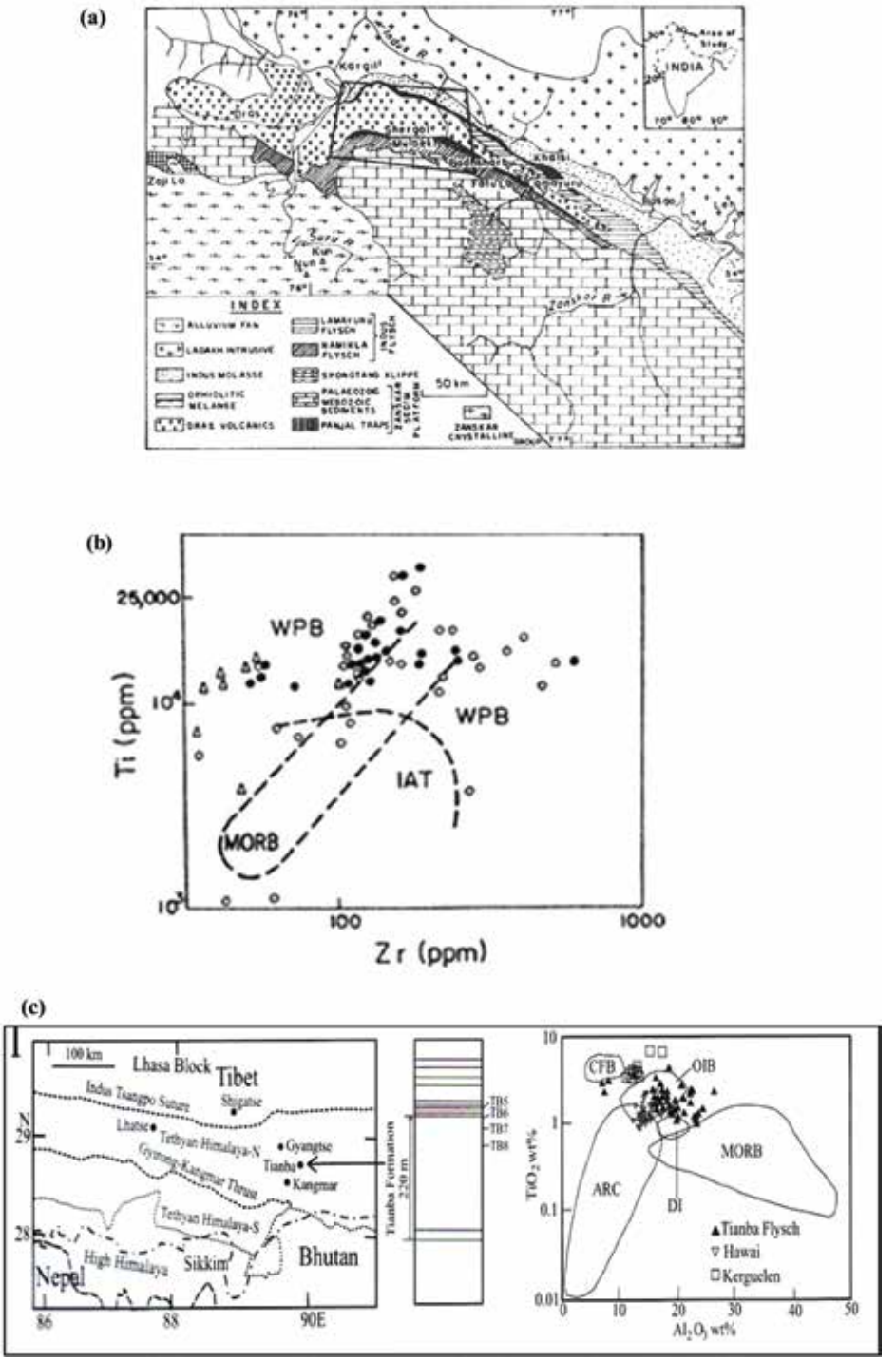

Figure 3. (a) Mafic magmatism exposed in the region between Leh and Kargil near the NW corner of NMM. (b) The Geochemical analysis of these late Cetaceous formation, reveal them to be of within-plate –basalt (WPB) type, which appears to be closely associated with those from the Reunion mantle plume and hence fall in the pre-outburst category (after Sinha and Mishra, 1992). (c) The map (on left) gives th location (28°44´N; 89°57´E) of late Cretaceous Tianba formation (exposed in the Nieru valley, souhern Tibet). TB5–TB8 are four samples containing spinel. The map on the right shows. Major element compositions of spinels shown on tectonic setting discriminant plot of the TiO_2 vs Al_2O_3. Continental flood basalts-CFB; Ocean island basalt (OIB); Midocean Ridge basalt (MOR) and island arc. The Cr rich samples from Tianba mostly correlated with OIB and CFB types (modified from Zhu et al., 2005) and strongly indicate a plume type mantle source. For comparison, spinel data from Kerguelen and Hawaii hotspots are also given.

LEUCOGRANITES

Peraluminous leucogranites are common in large orogenic belts; however origin of these syn-collsional leucogranites (LG) is highly controversial (Ma et al., 2017a) as evident from a number of studies (Bird, 1978; Le Fort et al., 1987; England and Thompson, 1984; Pinet and Jaupart, 1987; Jaupart and Provoast, 1985; England and Le Fort, 1992; England and Molnar, 1993). These LGs occur in all the three corridors of the NMM, viz. High Himalaya (HH), Tethyan Himalaya (TH) and the Gangdese Batholith (GB). The High Himalaya has a discontinuous presence of leucogranites plutons (see Figure1 in Windley, 1988) characterized by ages between 24 and 7 Ma (Scharer et al., 1986). There is a northward increase of ages of LGs across the NMM. It may be noted that although Mt. Kailas is considered to be a part of the Trans Himalaya Gangdese corridor, wherein much older ages of LGs (even upto 63-140 Ma) are found (Ma et al., 2017a), However, according to (Gustova et al., http://isinn.jinr.ru/proceedings/isinn-23/pdf/Gustova2.pdf) the age of the Mt. Kailas leucogranite is ~10.1±1.4 Ma, falling within the age interval (24-7 Ma) of Himalayan leucogranites. Recent mapping of Gangdese block also revealed that its LGs are similar to those Himalaya. All these LGs are considered to have been formed as a result of the intracrustal melting, following the India- Eurasia collision.

Regarding the heat required for the melting of the crust, problem of the heat source has been a matter of debate (Valdiya, 2001). Interestingly, the RAMBA leucogranites of Tethyan Himalaya, exhibit three episodes of LG generation at around 44, 28, and 8 Ma (Liu et al., 2014). Similarly, from the southern part of Lhasa (Tibet), a Paleocene (c. 62 Ma) leucogranite has been reported by (Ma et al., 2017b). They suggest that during this period, "slab-roll" would have significantly enhanced the asthenospheric corner flow and supplied long-lived heat source for coeval crustal anatexis and metamorphism in south Lhasa, during the early phase of continetal collision.

Heat source

Le Fort (1981) suggested that the occurrence of young post-collisional granites require large thermal perturbation. For this, Molnar et al. (1983) and Molnar (1984) list several possible heat sources like, (i) heat supplied from below the lower thrust plate, (ii) radiogenic heating within the crusts of both upper and lower plates, and (iii) frictional heating along the fault. As per his study, the lack of evidence for significant mafic magma necessary to cause melting of the upper plate rocks, imply that the leucogranites may be a product of crustal processes. Although the heat source needed for the partial melting of the source rocks still remain controversial, Nabelek and Liu (2004) postulated possibility of the following sources of heat:

i. A thickened crust with exponentially decaying distribution of the heat producing isotopes with depth, but it has been shown to be insufficient for heating the upper crust into melting condition.
ii. Thick sequence of sedimentary rocks with high amount of internal radioactive heat production.
iii. Decompressional melting.
iv. Thinning of mantle lithosphere, which is capable of raising the crustal temperatures, sufficient for the partial melting of metapelites, and
v. Shear heating.

According to Nabelek and Liu (2004), although the ii to iv sources, as listed above, may in a thickened crust, result into melting of the metapelites, but they also suggest that out of these, the shear heating may be the most viable process, as this model directly links the metamorphism and deformation, which precede the generation of leucogranites. Further, in case of Gangdese batholiths (GB), Wen et al. (2008) and Zhu et al. (2017) have noted two stages of plutonism, one at 103-80 Ma (late Cretaceous) and the other at 65-46 Ma ie late Cretaceous, each of the stages having been active for almost 20 Ma . These episodes appear to overlap with the time zones of the Kerguelen and Reunion plumes respectively. It is also pertinent to mention here that during the past decade, Chinese workers have carried out detailed geological studies, both in field as well as in lab in the eastern part of the NMM (or southern Tibet) have identified many mafic formations caused primarily by the Keguelen mantle plume and which fall in the pre-outburst category, because their ages are much older than that of the Rajmahal traps.

Evidence of thermal influx from the mantle

As discussed above, for past many decades, generation of the leucogranites has been considered to be due to partial melting (anatexis), confined only to the crust. But if the mantle plumes have affected the NMM, some role of mantle would be implied. In this context, a recent study by Zeng et al. (2016) appears quite significant. They have studied in detail the petrogenesis of the LENGKAZI leucogranite in the Himalaya and found that the leucogranite is an intrusion that contains large number of dioritic enclaves, which have a typical igneous texture, containing acicularapatite and have back-veining structure, quenched margins, besides crystallization ages identical to hosting two-mica granites, indicating that these enclaves

are magmatic. Although the enclaves are evolved, the most primitive samples contain high concentration of of MgO (upto 4.3%), Cr (upto 159 ppm), and Ni (upto 102 ppm) and contain relatively large ion-lithophile element. They are depleted in high–field-strength elements and have negative eNd(t) values (-8.6 to -6.1) and relatively high 87Sr/ 86Sr values (0.7085—0.7137), suggesting that they are derived from relatively enriched region of the lithosphere-mantle source. The whole-rock geochemical composition suggest that the primary melts that formed the Langkazi enclaves, were contaminated by the relatively juvenile Himalayan lower crustal material, implying that the mantle derived magmas underwent MASH (crustal melting, melt assimilation, magma storage and homogenization) process at the base of the lower crust, clearly indicating introduction of heat to the lower crust. This mantle derived heat may have also induced partial melting of the Himalayan lower crust, forming adakite-like magma. Such an input of thermal influx supplements other sorrces of heat like radiogenic heating, shear heating and decompositional melting.

Doming and Drainage Pattern at the Mt. Kailas

Significant 'doming' (or uplift) of the overlying crust – lithosphere system, may also take place owing to thermal input from the mantle plume present at depth. This fact has been used by Cox (1989) in a seminal paper, to explain the characteristic drainage pattern arising from the uplift. According to him, the doming or uplift may be sustained over quite long period of time following the plume–induced magmatic underplating, as Mckenzie (1984) had shown that uplift can take place due to the underplating. The areal extent of the doming follows from the lateral spread of the upwelling plume. Evidently, the central point of this dome or uplift, would act as the 'node' for streaming out of a topography-induced drainage system. To demonstrate this phenomenon, Cox (1989) provides a number of cases from all around the globe, which include (i) Deccan plume (India), Parana plume (south Brazil) and Karoo plume (Zambia) (Figure 4) among other examples.

Above observation is corroborated by Allen et al. (1992) by utilizing it in the Lake Superior region of North America. They find a high topography in the Lake Superior, and hence, the streams flow radially away from the center of this swell (or dome) towards the flanks. They attribute the topography swell and resulting dome-flank guided drainage pattern to a ~ 1100 Ma mantle plume. Further, this plume is also presumed to be responsible for giving rise to the mid-continental rift of the Central- North America (see figures 1and 2 in Allen et al., 1992). As per these authors, the influence of the plumes may be felt upto nearly 500 km distance. They further attribute the observed gravity anomaly, over the lake Superior, to the depletion of upper mantle and sustainance of doming for so long due to the magma underplating underneath.

Interestingly, the NMM of greater India, also exhibits domal upwarps (Valdiya, 2001). And in view of the earlier discussion, including the above two studies, the doming of the Mt. Kailas appears to be plume-induced also/as there thermal inputs too would contribute to doming, which inturn acts as a major 'Node' (Figure 5) of the characteristic drainage pattern of the ITS-Himalaya region, caused by the dome-flank system. A number of major rivers like Indus, Tsangpo, Satlaj, Karnali and Ganga stream out of this Kailas node. These rivers provide fresh water to more than one-fifth of world population. The Indus and Brhamaputra (or Tsangpo) rivers, flow along the NMM, with Indus to the west and Brhmaputra towards the east. As mentioned above, and Ru and Kg plumes also seems to have followed nearly similar paths.

Further, the Gangotri region of high Himalaya, which is considered to be the point of origin of river Ganga, is ~ 225 km southwest of Mt. Kailas, however from the INDEPTH study of the Tibet-Himalaya collision zone (Nabelek et al., 2009), Indian slab has been underthrusting the Tibet plate (continental–continental subduction) (Figure 6) for over the past ~50 Ma. it has reached ~31°N beneath the south Tibet. It may be relevant to mention that the presence of mantle plumes would facilitate the subduction process due to plume-triggered lubrication (Raval and Veeraswamy, 2007; Gerya et al., 2015). The underthrusting implies that in order to better comprehend the geodynamics and its consequences, one may have to gradually retrieve the Indian plate by going back in time and in space (in south-west direction), because the present forward movement is trending north-east. The age of Kailas leucogranite is measured as 10.0+1.4 Ma (Gustova et al http://isinn.jinr.ru/proceedings/isinn-23/pdf/Gustova2.pdf) and if rate of underthrusting is taken as 20mm/yr (Bilham et al 1997; Chen et al 2017)) between India and the Indus-Yarlung suture (IYS) or the southern boundary of Tibet. Then by going back in space and time the Indian slab beneath Mt. Kailas (presently at 31.06 N; 81.3 E) would have been closer to the Gangotri (30.9 N; 78.9 E) during the Himalayan metamorphism and emplacement of the leucogranite.

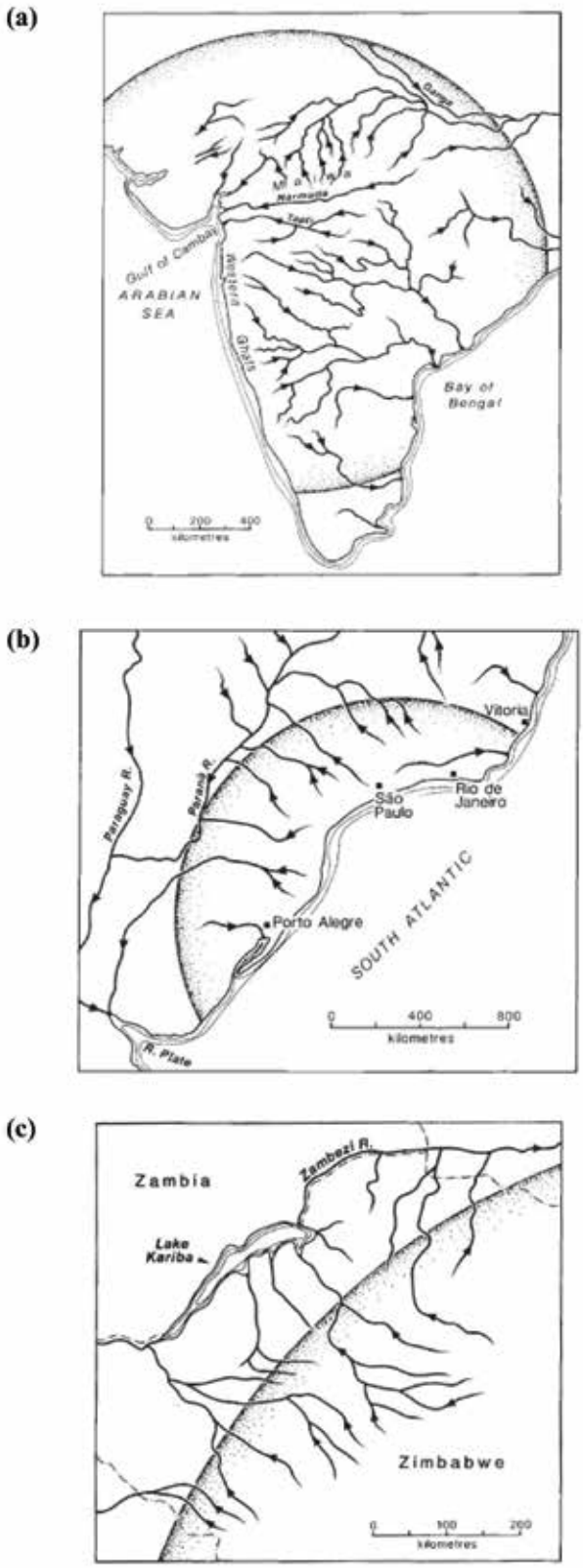

Figure 4. (a) The Reunion mantle plume and consequent radial drainage pattern of the peninsular India. (b) Parana plume induced dome-flank system and consequent drainage pattern in southern Brazil. (c) The dome-flank system drainage formed by the Karoo plume and resulting drainage pattern over Zambia (after Cox, 1989).

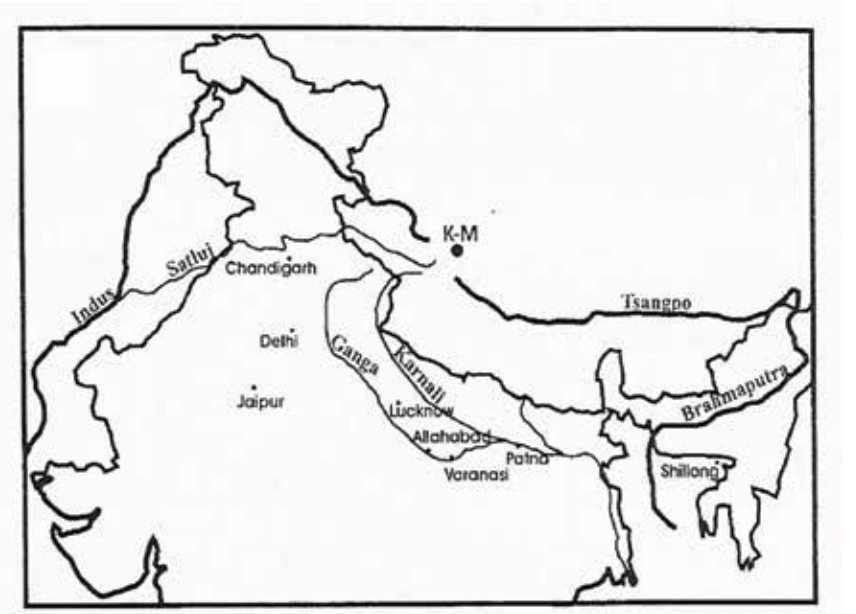

Figure 5. The drainage pattern of major rivers emanating from the Mt. Kailas node (after Valdiya, 1998). As mentioned in the text, the paths of the Indus and Brahmaputra (Tsanpo) rivers seem to interestingly follow the corridors of the NMM affected by the Reunion and Kerguelen mantle plumes.

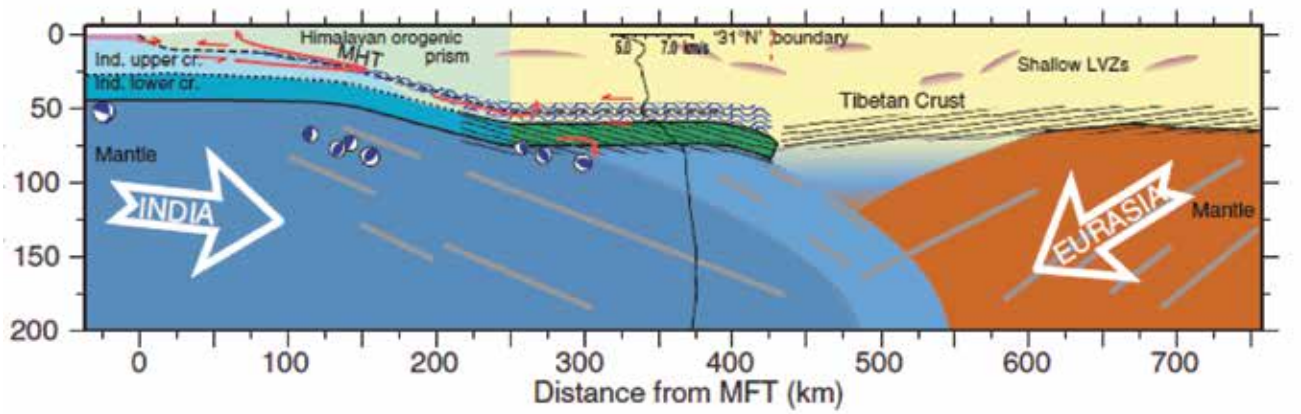

Figure 6. The model depicting under thrusting of the Indian slab below the Tibetan plate, based on the INDEPTH study. India seems to have penetrated beneath the Tibet upto ~ 31 N (after Nabelek et al., 2009).`

CONCLUSIONS

On the basis of the paleorecontructions and magmatic occurrences, it appears that the NMM of Indian subcontinent has been thermally affected by the Kerguelen mantle plume (on the estern side) and Reunin plume (on the western part). These results and the underthrusting of Indian plate beneath the Tibetan slab, suggest that Mt. Kailas may be the northern most point of the Himalaya and is the 'Node" for a number of major rivers of India and Asia. This follows from the doming caused by the influence of 'thermally active' pre-outburst phases of the Kerguelen and Reunion mantle plumes. The thermal inputs from these plume would also contribute/add to the heat sources required for the generation of the Oligocene-Miocene leucogranites, which occur discontinuously along the high Himalaya form the above discussions an interesting possibility also seems to emerge that the boundaries/ margins of the subcontinent seems to have been carved out by interaction of its lithosphere with the mantle plumes.

ACKOWLEDGMENT

Author is extremely thankful to the editor for painstakingly going through the manuscript and suggested changes that has significantly improved the presentation, Author dedicates the study to his teacher and guide late Dr, Janardan G. Negi.

Compliance with Ethical Standards

The author declare that he has no conflict of interest and adhere to copyright norms.

REFERENCES

Allen, D.J., Hinze, W.J. and Cannon, W.F., 1992. Drainage, topographic and gravity anomalies in the Lake Superior region: Evidenc for a ~ 1100 Ma mantle plume. Geophys. Res. Lett.,19(21), 2119-2122.

Baksi A.K., 1994. Geochronological studies on whole rock basalts, Deccan traps, India: evaluation of the timings of volcanism related to the K-T oundary. Earth. Planet. Sci. Lett., 121, 43-56.

Baksi, A.K., 1995 Petrogenesis and timing of volcanism in the Rajmahal flood basalts province, north eastern India Chem. Geol. 122, 73-90.

Basu, A., Renne, P.R., Das Gupta, D.K., Teichman, F. and Fored, R.J., 1993. Early and late alkali igneous pulses and a high mantle plume origin for the Deccan flood basalts. Science, 261, 902-906.

Bird, P., 1978. Initiation of intracontinental subduction in the Himalaya. J. Geophys. Res., 83, B10, 4975-4987.

Bilham, R., Larson, K. and Freymueller, J., 1997. GPS measurement of present day convergence across the Nepal Himalaya. Nature, 386, 61-64

Brown, L.D., Zhao, W., Nelson, K.D., Hauck, M., Alsdorf, D., Ross, A., Cogan, M., Clark, M., Liu, X. and Che, J., 1996. Bright spots, structure, and magmatism in Southern Tibet from INDEPTH seismic reflection profiling. Science, 274(5293), 1688-1690.

Chen, M., Fenglin Niu, Tromp, J., Lenardic, A., Lee, C.T., Cao, W. and Ribeiro, J., 2017. Nature communications 8, 15659.

Cox, K.G., 1989. The role of mantle plumes in the development of continental drainage pattern. Nature, 342, 873-877.

Curray, J.R., Emmel, F.J., Moore, D.G. and Raitt, R.W., 1982. Structure, tectonics and geological history of NE Indian Ocean: In Nairn A.E.N. and Stehli F.G. (eds): The ocean basins and margins. Plenum Press, 6, 399-450.

England, P.C. and Thompson, A.D., 1984. Pressure-Temperature-Time Paths of Regional Metamorphism I. Heat transfer during the evolution of regions of thickened continental crust. J. Petrol., 25, 894-928.

England, P. and Le Fort, P., 1992. Heat source for Tertiary metamorphism and anatexis in the Annapurna-Mansalu region central Nepal. J. Geophys. Res., 97(B2), 2107-2128.

England, P. and Molnar, P., 1993. Cause and effect among thrust and normal faulting, anatectic melting and exhumation in the Himalaya. Geol. Soc. Lond. Sp. Pub. 74, 401-411.

Gerya, T.V., Stern, R.J., Baies, M., Sobolov, S.V. and William, S.A., 2015. Plate tectonics on the earth triggered by plume-induced subduction initiation. Nature 527, 221-225.

Gustova, M.V., Maslova, O.D., Trinh, T.T., M. and Norov, N., Determination of elemental composition and the age of geological samples collected at the Kailas mountain (Tibet) by X ray and nuclear analytical methods. http://isinn.jinr.ru/proceedings/isinn-23/pdf/Gustova2.pdf

Kent, R.W., Pringle, M.S., Muller R.D., Saunders A.D. and Ghose, N.C., 2002. 40Ar/39Ar geochronology the Rajmahal basalts, India and their relationship to the Kerguelen plateau. J. Petrol., 43, 1141-1153.

Klootjwick, C.T., 1979. A review of paleomagnetic data from Indo-Pakistan fragment of Gondwana: In Geodynamics of Pakistan. (Eds. A.Farah and K.A. DeJong), Geol. Surv. Pakistan, 41-80.

Klootjwick, C.T. et al., 1994. Further paleomagnetic data from Chitral (Eastern Hindukush) evidence for early India-Asia contact. Tectonophyscs, 237(1-2), 1-25.

Le Fort, P., 1981. Manaslu leucogranite: A collision signature of the Himalaya: A model for its genesis and emplacement. J. Geophys. Res., 86(B11), 10545-10568.

Le Fort, P., et al., 1987. Crustal generation of Himalayan leucogranites. Tectonophysics , 134(1-3), 39-57.

Jaupart, C. and Provost, A., 1985. Heat focusing, granite genesis and inverted metamorphic gradients in continental collision zone.

Mahoney, J.J. et al., 2002. Cretaceous volcanic rocks of the South Tethyan suture zone, Pakistan: implications for the Réunion hotspot and Deccan Traps. Earth Planet. Sci. Lett. 203, 295-310.

McCormik, G.R., 1991. Origin of volcanics in Tethy suture zone of Pakistan. In Ophiolites genesis and evolution of oceanic lithosphere (Ed. Peters et al.) 715-722.

Molnar, *P.*, Chen, W.P. and Padovani, E., 1983. Calculated temperatures in over thrust terraines and possible combinations of heat sources responsible for the Tertiary granites in the greater Himalaya. J. Geophys. Res., 88(B8), 6415-6429.

Molnar, P., 1984. Structure and tectonics of the Himalaya. Ann. Rev. of Earth and Planet. Sci. 12, 489-518.

Nabelek, J., Hetenyi, G., Vergne, J., Sapkota, S., Kafle, B., Jiang, M., Su, H., Chen, J. and Huang B.S., 2009. Underplating in the Himalaya-Tibet collision one Revealed by the Hi-CLIMB Experiment. Science, 325, 1371-1374.

Nabelek, J. and Liu, M., 2004. Petrological constraints on the origin of leucogranites in collision zone. Proc. R.S. Edinburgh Earth sci., 95, 73-85.

Raval, U. and Veeraswamy, K., 2007. Within and beyond the Protocontinents: Some geophysical aspects reflecting geodynamics of the Indian continental lithosphere, Int. Assoc. Gondwana Res. Mem. No.10, 263-285.

Pinet, C. and Jaupart, C., 1987. A thermal model for the distribution in space and time of the Himalayan granites. Earth Planet. Sci. Lett., 84(1), 87-99.

Scharer, U., Xu, R.H. and Allegre, C.J., 1986. U-(TH)-Pb systematic and ages of Himalayan Leucogranite south Tibet. Earth. Planet. Sci. Lett.,77(1), 35-48.

Sivaraman, T.V. and Raval, U., 1995. U-Pb isotopic studyof zircons from a few granitoids of Delhi-Aravalli belt. J. Geol. Soc. Ind. 46, 461-475.

Shrivastava, R.K., 1988. Magmatism in Aravalli mountain range and its environs. J. Geol. Soc. Ind. Mem. No. 7, 77-93.

Windley B. F. 1988 Tectonic framework of the Himalaya, Karakoram and Tibet and problems of their evolution. Trans. royal Soc. A., 326, issue 1589.

Zhu B., Delano, J.W. and Kidd, W.S.F., 2005. Magmatic compositions and source terranes estimated from melt inclusions in the detrital Cr-rich spinels: An example from mid-Cretaceous sandstones in the eastern Tethys Himalaya. Earth. Planet. Sci. Lett., 233, 295-309.

Zhu, D., et al., 2007. Petrogenesis of volcanic rocks in the Sangxiu formations, central segment of Tethyan Himalaya: A probable example of plume-lithosphere interaction. J. Asian Earth Sci. 29, 320-335.

Zhu, D., et al., 2008. Petrogenesis of the earliest early Cretaceous mafic rocks from the CONA area of the eastern Tethyan Himalaya in south Tibet: Interaction btween the incubatingKerguelen mantle plume and the eastern greater India. Lithos, 100(1), 147-173.

Zhu, D., et al., 2017. Raising the Gangdese mountain in southern Tibet. J. Geophys. Res., (Solid Earth), 122(1), 214-223.

Valdiya, K.S., 1998. Dynamic Himalaya. Geological Magazine, Univ. Press. pp 178.

Valdiya, K.S., 2001. Himalaya: emergence and evolution. Univ. press ltd. p.139.

Wen, D.R., Liu, D., Chung, S.L. and Chu, M.F., 2008. Zircon SHRIMP U-Pb ages of Gangdese batholith and implications for NeoTethys subduction in S. Tibet. Chem. Geol., 252(3), 191-201

Liu, Z.C., Wu, F.Y., Wei-Qiang Ji, Wang, J.G. and Liu, C.Z., 2014. Petrogenesis of Ramba Leucogranite in Tethyan Himalaya. Lithos, 208-209.

Ma, L. et al., 2017a. Early Cretaceous (~140Ma) aluminous A-type leucogranite in Tethyan Himalaya, Tibet: Product of crust-mantle interaction during lithospheric extension. Lithos, 300, DOI: 10.1016/j.lithos.2017.11.023

Ma, L. et al., 2017b. Paleocene (ca. 62 Ma) leucogranites in southern Lhasa Tibet: Product of syn-collisional crustal anatexis during slab-roll back, J. Petro. 58(11), 2089-2114.

Mckenzie, D., 1984. A possible mechanism for epierogenic uplift. Nature, 307, 616-618.

Sinha, A.K. and Mishra, M., 1992. Plume activity and seamounts in NeoTethys: evidence supported by geochemical and geochronological data, J. Himalayan Geol., 3, 91-95.

Storey, B., 1995. The role of mantle plumes in continental breakup: case histories from Gondwanaland. Nature, 377, 301-308.

Zeng, Y., Hou, Z., Fu, Zhu, D., Liang, W. and Xu, P., 2016. Mantle inputs to Himalayan anatexis: Insights from petrogenesis of the Miocene Langkazileucogranite and its dioritic enclaves. Lithos., 264, 125-140.

Received on: 29.4.18; Revised on: 20.3.19; Accepted on: 15.4.19

J. Ind. Geophys. Union (May 2019)
v.23, no.3, pp: 249-259

Sea surface temperatures of different Nino regions over equatorial Pacific Ocean and linkages with summer monsoon rainfall in India and its homogeneous regions

R. Bhatla[1*], Harikesh Yadav[2], Babita Dani[3] and B. Mandal[1]

[1]Department of Geophysics, Institute of Science, Banaras Hindu University, Varanasi-221005, India.
[2]Department of Botany, Institute of Science, Banaras Hindu University,Varanasi-221005, India.
[3]Department of Geology, Institute of Science, Banaras Hindu University, Varanasi-221005, India.
*DST-Mahamana Centre of Excellence in Climate Change Research, Institute of Environment and Sustainable Development, Banaras Hindu University, Varanasi-221005, India.
Corresponding author: rbhatla@bhu.ac.in

ABSTRACT

The intra-seasonal and inter-annual variability of the summer monsoon has a tremendous socio-economic impact on India, especially in the fields of agriculture and health. In the present study, the correlation between SST (Sea Surface Temperature) anomaly of different Nino regions (Nino1+2, Nino3, Nino 3.4 and Nino 4) and summer monsoon rainfall have been analyzed to find the association of SST of different Nino regions over Equatorial Pacific Ocean with the rainfall over all India and its homogeneous regions, including core monsoon zone for different time scale. The study shows that the entire Indian Summer Monsoon Rainfall (ISMR), is inversely related to SST anomalies over Nino 3, Nino 3.4 and Nino 4 region for the periods previous to spring to winter spring (MAM-DJF) and hence, behavior of SST anomaly during MAM-DJF over Nino 3, Nino 3.4 and Nino 4 region can be used as precursor of ISMR over entire India.

Keywords: ISMR, SST, correlation analysis, homogeneous regions.

INTRODUCTION

Monsoon is a complete replacement of the dry hot air by the equatorial maritime air up to an altitude of three to five kilometers over the land and water surface. Most of the annual rainfall in India occurs from June to September, during what is referred to as the summer monsoon or southwest monsoon. The winter monsoon or the northeast monsoon brings rainfall to the south-eastern part of India through north easterlies during October to December and contributes a small percentage to the annual Indian rainfall. Two remarkable features of the summer monsoon are its regular occurrence every year from June to September and the irregular variation in the amount of seasonal mean rainfall that it brings to India from one year to the other. There are many instances of years with flood (strong monsoon) or drought (weak monsoon), during which India as a whole receives excess or deficient seasonal rainfall, respectively. The seasonal reversal of the wind direction occurring in May brings moisture from the warm waters of the tropical ocean to the Indian continent through south-westerlies. The onset of the monsoon over India involves the establishment of a low pressure region called the monsoon trough. The active and break periods are thought to be related to where the monsoon trough is over India and to the genesis and growth of the monsoon disturbances within the trough.

Researchers have experienced that ISMR (Indian Summer Monsoon Rainfall)is controlled by different global forcing remotely, such as North Atlantic Oscillation (NAO)/ Arctic Oscillation (AO) (Joaquim et al., 2010; Mi-Kyung et al., 2006), Madden-Julian Oscillation (MJO) (Bhatla et al., 2016), Pacific Decadal Oscillation (PDO) (Dong, 2016; Krishnan and Sugi, 2003), Pacific North American (PNA) pattern (Joaquim et al., 2010; Leathers et al., 2009; Feldstein, 2001).The principal controlling factor is found to be the tropical Pacific's SST anomaly for variability of tropical monsoon circulation in inter-annual scale. Climate scientists have shown a link between ISMR and eastern Pacific Ocean SST anomaly. El-Niño events are nothing but the warmest SST anomaly in eastern Pacific Ocean, which is responsible for a lesser amount of summer monsoon rainfall that occurs in India (Sikka, 1980). Later, pronounced and strong inverse relations between summer monsoon rainfall and SST anomalies over the eastern Equatorial Pacific Ocean, have also been identified by Angell (1981) and Mooley and Parthasarathy (1983, 1984), using data of a few seasons. Rasmusson and Carpenter (1982, 1983), Elliott and Angell (1987) and Parthasarathy et al. (1988) also proposed that the Indian Summer Monsoon Rainfall is related to SST anomalies, over the eastern Equatorial Pacific Ocean. Further, Bhatla and Chattopadhyay (1995) have studied different homogenous regions of drought and floods over India utilizing the criteria of India Meteorological Department (IMD). Aldrian and Susanto (2003) examined the association of SST in the Pacific and Indian Oceans with the variability of rainfall over Indonesia. Varikoden and Preethi (2013) peculiarly observed that either the Pacific

Ocean SST hot or cold or correspondingly the ISMR is deficient or excess. Chattopadhayay and Bhatla (2002) explained the influence of different Nino regions on ISMR in association with QBO. Besides, Chattopadhayay and Bhatla (1993) also studied the combined impact of SST anomalies of Eastern Pacific Ocean and Western Pacific Ocean on ISMR. Since, there are many studies which have been based on larger scale/regions, but none over smaller scale. Therefore, the objective of the present work is to study the association of Sea Surface Temperature of different Nino regions over Equatorial Pacific Ocean on smaller scale/regions, with the rainfall over all India and the six homogeneous regions, including core monsoon zone for different time period of the year.

DATA AND METHODOLOGY

In the present study, summer monsoon (June – September) rainfall data of All India (AI) as well as different zone of homogenous regions of India namely Central North East(CNE), North West(NW), North East (NE), Peninsular India(PI) and West Central (WC) and Core Monsoon zone (Core), taken from Indian Institute of Tropical Meteorology, Pune, (www.tropmet.res.in). Rainfall data are calculated as percentage of departure and are used for analysis in the present study. Shukla (1987) stated that the interannual study of percentage of departure is more suitable. The Nino regions over Equatorial Pacific Ocean are taken into consideration for the present study. The monthly SST data over different Nino regions e.g. Nino1+2 (0^o-10^o S, 90^0-80^0 W), Nino3 (5^oN-5^oS, 150^o-90^o W), Nino 3.4 (5^oN-5^oS, 170^o-120^o W), Nino4 (5^oN-5^oS, 160^oE-150^oW), were taken from National Oceanic and Atmospheric Administration (NOAA) site (http://www.cpc.ncep.noaa.gov/data/indices/sstoi.indices). Nino1+2 regions are integrated by taking arithmetic average of Nino1 and Nino2 zones. SST anomaly of different time scale has been constructed, using arithmetic operation. Pearson Moment Correlation Coefficient (CC) approach has been used to furnish the degree of association between SST anomalies over different Nino region and rainfall anomalies over entire India and its homogeneous regions. The CCs between SST anomaly of different Nino region with ISMR anomaly, have been computed separately for the durations of single month, two successive months, and also for two following seasons starting from the previous December to the February DJF (-) and March to May (MAM), are calculated in order to verify the significance of "r" associated with definite degree of freedom using conventional student t test in terms of confidence level.

RESULT AND ANALYSIS

Effect of SST over All India Regions

The correlation coefficient (CC) between anomalies of Indian Summer Monsoon Rainfall (ISMR) over all India and different Nino regions viz. Nino 1+2, Nino 3, Nino3.4 and Nino4 are shown in different tables. It is clear from the Table 1 that the SST over Nino 1+2 region, shows the highest CC of 0.24 at confidence level 80% during January with all India rainfall. Table 2 shows that SST has the highest CC of -0.31 at the confidence level 90% over Nino 3 region. It is also clear from the Table 3, that the

Table 1. Correlation coefficient between summer monsoon rainfall over All India, Core region, Central North East, North West, North East, Peninsular India and West Central with Nino 1+2 regions.

Month/season	AI	CORE	CNE	NW	NE	PI	WC
January	**0.24**	**0.26**	**-0.16**	**0.22**	0.06	**0.39**	**0.28**
February	0.16	0.16	-0.12	0.12	0.12	0.31	0.16
March	-0.03	-0.06	-0.06	-0.08	0.14	0.08	-0.07
April	-0.10	**-0.25**	-0.12	-0.15	**0.17**	0.09	-0.14
May	0.06	0.16	**-0.23**	0.11	-0.03	0.22	0.12
JF	0.21	0.22	-0.14	**0.18**	0.09	**0.36**	**0.23**
FM	0.06	0.04	-0.09	0.01	0.13	0.19	0.04
MA	-0.10	**-0.25**	-0.13	-0.16	**0.18**	0.09	-0.15
AM	-0.10	-0.24	0.07	-0.15	**0.17**	0.10	-0.14
DJF(-)	0.21	0.23	**-0.17**	**0.18**	0.08	**0.37**	**0.25**
JFM	0.14	0.13	-0.12	0.10	0.11	0.28	0.14
FMA	-0.10	**-0.25**	-0.13	-0.15	**0.18**	0.10	-0.14
MAM	-0.10	-0.24	-0.14	-0.15	**0.17**	0.11	-0.14
MAM-DJF	-0.12	**-0.27**	-0.12	**-0.17**	**0.17**	0.07	-0.17

Table 2. Correlation coefficient between summer monsoon rainfall over All India, Core region, Central North East, North West, North East, Peninsular India and West Central with Nino 3 region.

Month/season	AI	CORE	CNE	NW	NE	PI	WC
January	0.20	**0.27**	-0.27	**0.24**	0.05	**0.36**	**0.27**
February	0.14	0.23	**-0.31**	0.20	0.10	0.28	0.22
March	0.09	0.16	-0.26	0.13	0.09	0.18	0.15
April	-0.03	0.12	**-0.32**	0.07	-0.02	0.10	0.08
May	-0.12	0.07	-0.27	-0.05	**-0.13**	-0.01	0.01
JF	0.18	**0.25**	-0.29	0.23	0.07	**0.33**	0.25
FM	0.12	0.20	-0.29	0.17	0.09	0.24	0.19
MA	0.03	0.14	-0.30	0.10	0.04	0.15	0.12
AM	-0.08	0.09	**-0.31**	0.01	-0.08	0.04	0.05
DJF(-)	0.21	**0.27**	-0.28	**0.26**	0.07	**0.35**	**0.26**
JFM	0.16	0.23	-0.29	0.20	0.08	0.29	0.23
FMA	0.08	0.18	**-0.31**	0.14	0.06	0.20	0.16
MAM	-0.03	0.12	**-0.31**	0.05	-0.02	0.09	0.09
MAM-DJF	**-0.31**	**-0.28**	0.14	**-0.32**	-0.12	**-0.42**	**-0.30**

Table 3. Correlation coefficient between summer monsoon rainfall over All India, Core region, Central North East, North West, North East, Peninsular India and West Central with Nino 3.4 region.

Month/season	AI	CORE	CNE	NW	NE	PI	WC
January	0.14	**0.27**	-0.34	**0.23**	0.08	**0.28**	**0.22**
February	0.09	0.23	**-0.40**	0.20	**0.09**	0.21	0.18
March	0.09	0.16	-0.37	0.21	0.06	0.17	0.19
April	-0.02	0.12	**-0.42**	0.15	0.04	0.08	0.09
May	-0.18	0.07	-0.39	-0.03	-0.05	-0.07	-0.06
JF	0.12	0.25	-0.37	0.22	**0.09**	0.25	0.21
FM	0.09	0.20	-0.39	0.21	0.08	0.19	0.19
MA	0.04	0.14	**-0.40**	0.19	0.05	0.13	0.15
AM	-0.10	0.09	**-0.42**	0.06	0.00	0.01	0.02
DJF(-)	0.15	**0.27**	-0.35	**0.25**	**0.09**	**0.28**	**0.22**
JFM	0.11	0.23	-0.37	0.22	0.08	0.23	0.20
FMA	0.06	0.18	**-0.40**	0.20	0.07	0.17	0.16
MAM	-0.03	0.12	**-0.42**	0.13	0.02	0.07	0.09
MAM-DJF	**-0.27**	**-0.28**	0.22	**-0.29**	-0.11	**-0.39**	**-0.28**

highest CC of magnitude -0.27 at confidence level 80%, was observed over Nino 3.4 region. The CC of -0.24 at confidence level 80% is observed over Nino 4 region (Table 4) during MAM-DJF. It can be clearly seen that the highest CC among all months and seasons is -0.32, obtained over Nino 3 region with ISMR during MAM-DJF.

From the above discussion, the SST over Nino 3 region for MAM-DJF may thus be used as a predictor for all India rainfall. Figure 1 represents the variation in percentage departure of ISMR with SST anomaly of Nino 3 region during MAM-DJF for 29 years, since 1983 to 2011. Out of these 29 years, 17 years have shown inverse relation

Table 4. Correlation coefficient between summer monsoon rainfall over All India, Core region, Central North East, North West, North East, Peninsular India and West Central with Nino4 region.

Month/season	AI	CORE	CNE	NW	NE	PI	WC
January	0.05	0.17	-0.41	**0.19**	**0.15**	0.16	**0.12**
February	0.01	0.15	-0.45	0.16	**0.15**	0.11	0.09
March	-0.01	**0.18**	-0.46	0.18	0.06	0.06	0.11
April	-0.11	0.11	-0.47	0.12	0.01	-0.01	0.01
May	-0.22	0.04	**-0.53**	0.02	-0.05	-0.08	-0.07
JF	0.03	0.16	-0.43	0.17	**0.15**	0.14	0.11
FM	0.00	0.17	-0.46	0.17	0.11	0.09	0.10
MA	-0.05	0.15	-0.47	0.16	0.04	0.03	0.07
AM	-0.16	0.08	**-0.51**	0.08	-0.02	-0.04	-0.03
DJF(-)	0.07	**0.19**	-0.40	**0.21**	**0.15**	0.16	**0.13**
JFM	0.02	0.17	-0.44	0.18	0.13	0.12	0.11
FMA	-0.03	0.15	-0.47	0.16	0.08	0.06	0.08
MAM	-0.10	0.12	**-0.50**	0.12	0.01	0.00	0.03
MAM-DJF	**-0.24**	**-0.18**	0.13	**-0.20**	**-0.26**	**-0.31**	**-0.21**

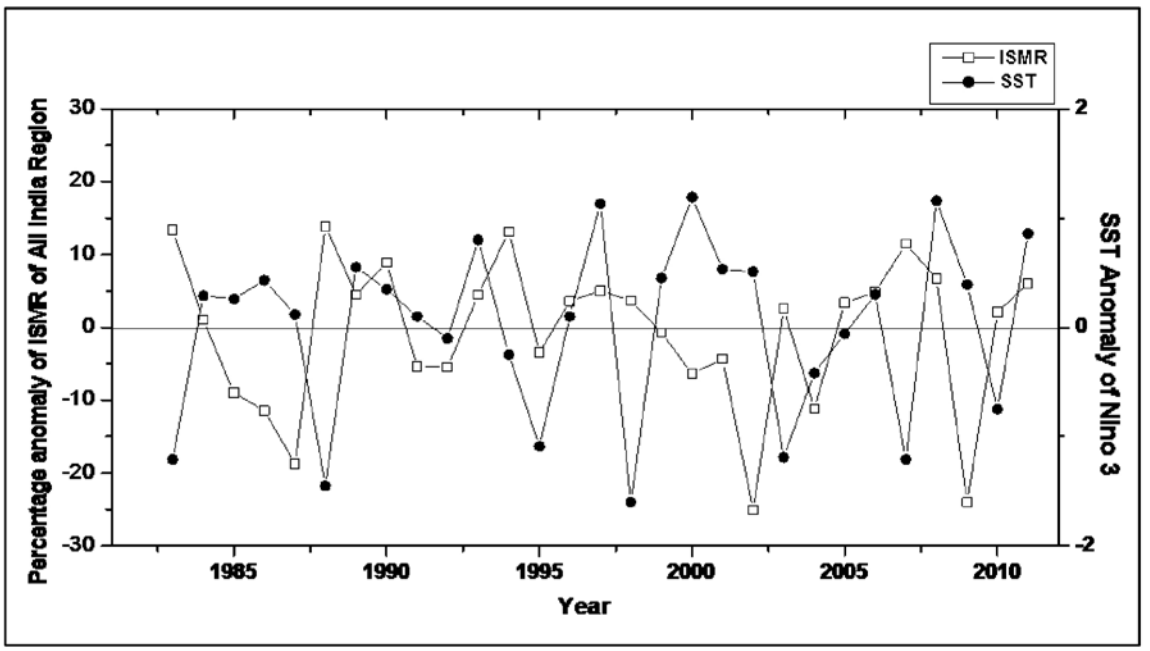

Figure 1. Time series of All India summer monsoon rainfall anomaly and SST anomaly over Nino 3 region during season MAM-DJF: n=29, r= -0.31 (confidence level 90%) 1983-2011.

between SST and rainfall anomaly, while 12 years show direct relationship.

Effect of SST over Core Region

Table1 also illustrates the CC between the anomalies of SST over Nino1+2 and ISMR over core region of India. The highest CC of magnitude -0.27 for season of MAM-DJF is observed with 80% confidence level. The CC are close to maximum with ±0.27 corresponding to 0.26,-0.25,-0.25 and -0.25 for months of January, April, MA and FMA respectively for Nino 1+2 region. Similarly, for Nino 3 region in Table 2, the maximum CC is -0.28 for the season of MAM-DJF with 80% confidence level. The CC found near to the significant value of -0.28 are 0.27, and 0.25 for January, DJF (-) and JF respectively**.** However, in Nino 3.4 region, the largest value of CC corresponding to season MAM-DJF is -0.28 (at 80%confidence level) in Table 3. The CC for the month January and season DJF (-) is 0.27 each which is near to significant value. In Nino 4 region

(Table 4), the CC is of magnitude 0.19 with 70% confidence level which is highest for season DJF (-). The CC near to the significant value is 0.18 and -0.18 for month MARCH and season MAM-DJF respectively. Thus, we observed that the CC between the SST and ISMR anomalies among all months/seasons over core region is highest in the Nino3 for the season of MAM-DJF.

Effect of SST over Central North East

The association of SST anomaly of different Nino regions (Nino1+2, Nino3, Nino3.4 and Nino4) and ISMR anomaly of Central North East (CNE) for the period from 1982 to 2011 are studied. From Table1 the maximum CC is foundto be -0.23 at confidence level 70% for the month of May in Nino 1+2 region. The CC -0.17 and -0.16 for season DJF(-) and month January are found close to the highest CC respectively. The Table 2 also depicts the highest CC that is -0.32 at confidence level 90% in the month of April over Nino region 3 and CC -0.31 have same magnitude for two season viz. FMA and MAM. Over the Nino 3.4 region, the CC of magnitude -0.42 is found to be maximum at the confidence level of 95%, which is largest of all other values for the month of April and seasons AM and MAM (shown in Table 3). Values that are found close to the maximum CC are -0.40,-0.40 and -0.40 for the month February and seasons MA and FMA respectively. While in the Nino 4 (Table 4) the CC is maximum i.e., -0.53 at confidence level 99% for the month of May. The other calculated CC for different months/seasons, -0.51 and -0.50, are close to the largest for AM, MAM respectively. Lastly, we came to a conclusion that out of all four Nino regions and among all months/seasons, the CC -0.53 is found significant for the month of May and are maximum for the Nino 4 region with Central North East (CNE).

Figure 2 shows the yearly variation of ISMR and SST anomalies in Central North East region for the month of May over Nino 4 region during 1982-2011. Out of 30 years data, 19 cases are inconsistent and 11 cases are in direct relationship. Thus, the relation between SST anomaly over Nino 4 region and summer monsoon rainfall is inverse. Comparatively, excess rainfall occurred (26.15%) over Central North East region due to negative SST anomaly 0.89 for the month of May in 2008. On the other hand, SST positive anomaly 0.66 for same period, produced 31.18% deficient rainfall in 2002 over Central North East region.

Effect of SST over North West Region

Further, the analysis of correlation coefficient (CC) between anomalies of Indian Summer Monsoon Rainfall (ISMR) and SST over different Nino regions for time period 1982 to 2011 have also been carried out. The maximum CC of magnitude 0.22 at confidence level 70%can be observed from the Table 1 for Nino 1+2 regions in the month of January. The values near to the highest CC are 0.18, 0.18 and -0.17 for season JF, DJF (-) and MAM-DJF. However, for the Nino 3 region the CC for North West region is more for the season of MAM-DJF with magnitude -0.32

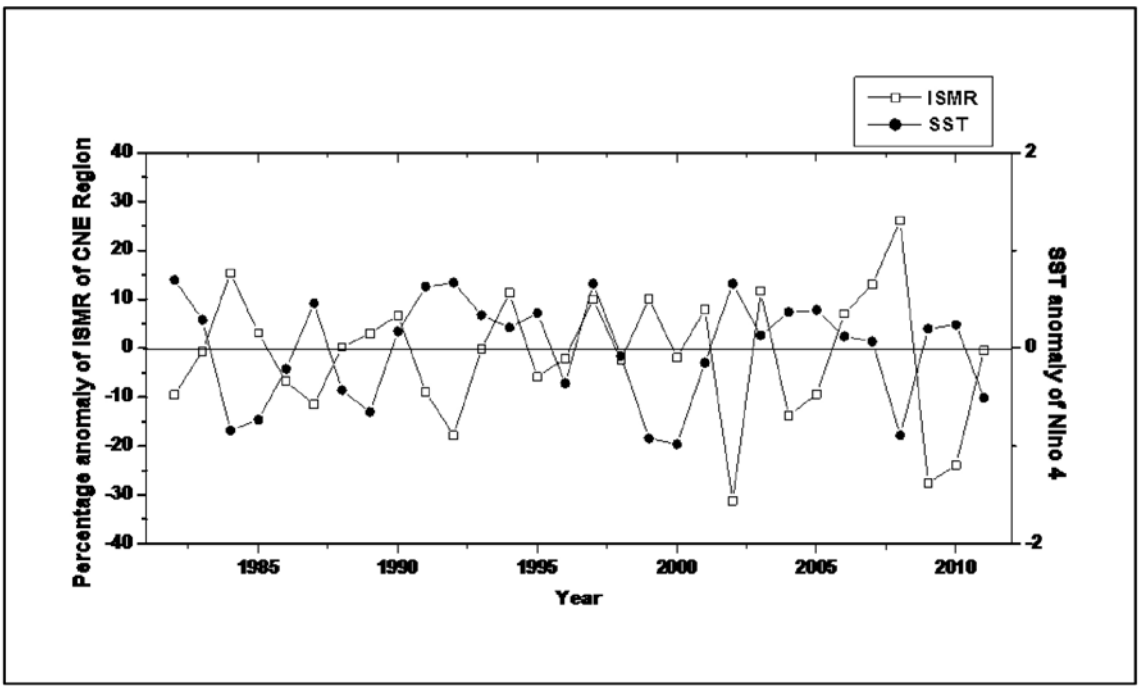

Figure 2. Time series of Central North East summer monsoon rainfall anomaly and SST anomaly over Nino 4 region during month of May: n=30, r= -0.53 (confidence level 99%) 1982-2011.

at confidence level 90% and is represented in Table 2. The other CC values close to the maximum are 0.26 and 0.24 for season DJF (-) and month January respectively. While it is observed from Table 3 that in the Nino 3.4 region, CC -0.29 at confidence level 80% for season MAM-DJF is largest of all computed values. Out of the rest calculated data, the CC 0.25 and 0.23 for season DJF (-) and month January respectively are close to the highest CC i.e. 0.29. Lastly, it can be seen from Table 4 for Nino 4 region, the highest CC of magnitude 0.21 at confidence level 70% is in season DJF (-)out of all other seasons. From the other calculated values which are close to the maximum CC are of magnitude-0.20 and 0.19 for season MAM-DJF and month of January. Therefore, out of all four Nino regions, we inferred that the CC -0.32 is highest for Nino region 3 in the season MAM-DJF among all other months/seasons. North West region in Figure 3, represents the yearly variation of ISMR and SST anomalies for the season MAM-DJF over Nino 3 region during 1983-2011. In this case, for the 29 years of data we observed inverse relation between SST and ISMR in 21 cases, while 8 cases are found to be in direct relation. During MAM-DJF in 2004 SST anomaly is -0.25, which accelerated the rainfall by 30.40% and in 1987 the SST anomaly 0.12 resulted to the deficiency in rainfall by 144.97% over North West region.

Effect of SST over North East Region

It is clear fromTable1that for the successive month MA and season FMA, the SST over Nino 1+2 region has higher CC of magnitude 0.18 each, at confidence level 60%. The other values close to the highest CC are 0.17 each for the months of April, AM and seasons MAM, MAM-DJF. Similarly, in Table2, the maximum CC is -0.13 at confidence level 60% for SST over Nino 3 region during the month of May, is dominating over all the months/seasons. While in case of SST over Nino region 3.4, the highest magnitude of CC is -0.11 for season MAM-DJF (Table3). The CC values proximate to the maximum are 0.09 each for months February, JF and season DJF (-). Lastly, in case of Nino 4 region, the largest CC of magnitude -0.26 and confidence level 80% in the season of MAM-DJF (Table4).The CC values revolving around the highest is 0.15 each for the month of January, February and JF and in season DJF(-). It is clear from the above discussion that the highest CC -0.26, at confidence level 80% among all months/seasons is found for MAM-DJF over Nino 4 region in North East zone.

Effect of SST over Peninsular India Region

Table1 illustrates the comprehensive correlation analysis for Peninsular India (PI) region and SST anomaly over different Nino regions for the period 1982-2011. During the month of January the highest CC of magnitude 0.39is observed at confidence level 95% for SST over Nino 1+2 region. Other CC values close to the highest are 0.37 and 0.36 for season DJF (-) and successive month JF respectively. In case of Nino 3 region from Table2, the maximum CC is observed to be -0.42 at confidence level 95% during season MAM-DJF. The other CC values close to the highest CC are 0.36, 0.35 and 0.33 for month January season DJF (-) and successive month JF respectively. Table 3 shows SST

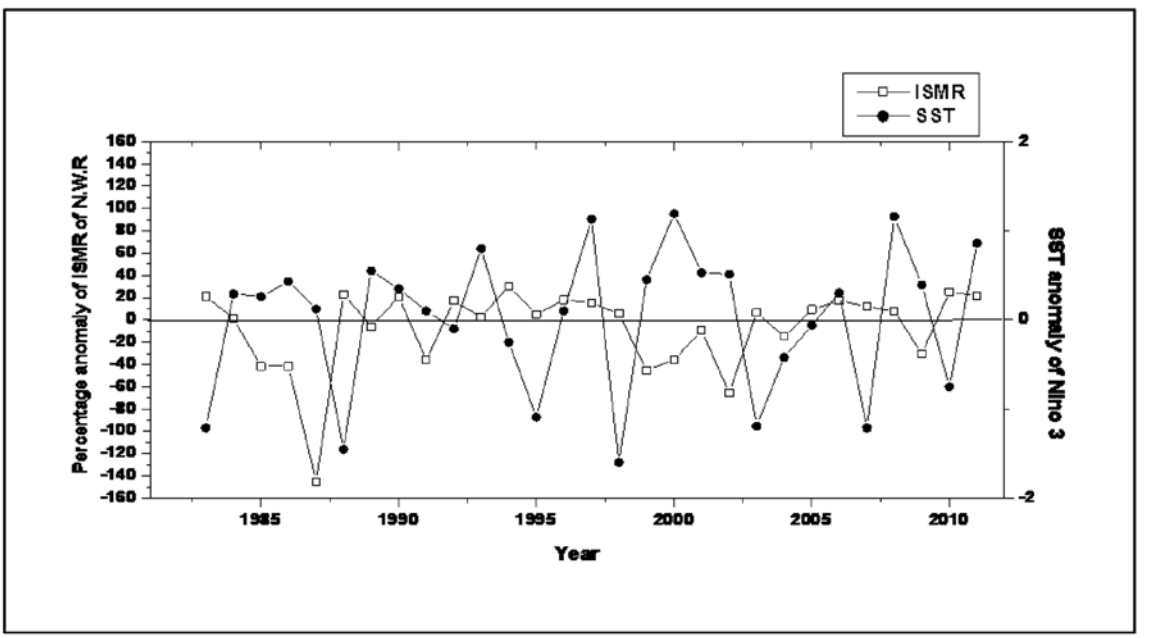

Figure 3. Time series of North West summer monsoon rainfall anomaly and SST anomaly over Nino 3 region during season MAM-DJF: n=29, r= -0.32 (confidence level 90%) 1983-2011.

over Nino3.4 has largest CC of -0.39 at confidence level 95% for season of MAM-DJF. Values that are close to the highest CC over Nino 3.4 region are 0.28 and 0.28 for month of January and season DJF(-) respectively. The CC of magnitude -0.31 at confidence level 90% in the season DJF (-) is observed for SST over Nino 4 region (Table 4). It is observed that over all the four Nino regions taken under study, the largest CC -0.42 is found during the season of MAM-DJF.

Effect of SST anomaly of Nino 3 region on summer monsoon rainfall over Peninsular India during time period 1983-2011 for MAM-DJF season is shown in Figure 4. It has been observed that 19 cases are found in inverse relation whereas direct relation is found in 10 cases out of 29 years between monsoon rainfall and SST anomalies. It is clearly observed from the figure 4 that negative SST anomaly 1.21 responses to render excess rainfall 25.24% over Peninsular India in 2007. After that in 2002, positive SST 0.51during period MAM-DJF was found responsible for the occurrence of less rainfall 52.60% over Peninsular India.

Effect of SST over West Central

Table 1 shows comprehensive correlation analysis in West Central (WC) region between SST and ISMR anomalies over four Nino regions for time period 1982-2011. From the Table 1, it is observed that during the month of January CC of magnitude 0.28 is maximum at confidence level 80% for Nino region 1+2. The computed data values for month/season DJF (-) and JF respectively have CC of 0.25 and 0.23 that cluster around the highest value of 0.28. While for Nino 3 region, the CC for WC is maximum for season of MAM-DJF with 0.30 at confidence level 80% (Table2). The other CC values that are close to the higher value are, 0.27 and 0.26 for January and DJF (-) respectively. Then in Nino 3.4 region, the maximum CC is -0.28 at confidence level 80%, corresponds to the season of MAM-DJF, which is shown in Table 3. The other significant values of CC 0.22 for month/season of January and DJF (-) are close to the highest. And at last from the Table 4, in Nino 4 region the CC for season of MAM-DJF is -0.21, which is maximum of all the other months and seasons at confidence level 70%. The CC values found aggregated near to the highest i.e. 0.13 and 0.12 respectively related to month of January and season DJF (-). From the above calculated results, it has been clearly observed that the highest CC found for the season of MAM-DJF is -0.30 at confidence level 80% over Nino 3 region for WC region of India.

CONCLUSIONS

The inter-annual variability of Indian Summer Monsoon Rainfall plays a vital role on economy, agriculture and daily life of living beings. This inter-annual variability of summer monsoon depends on regional circulation features and associated with other features on global scale. Most of the studies have been carried out for country as whole or based on meteorological sub-divisions, but very few studies

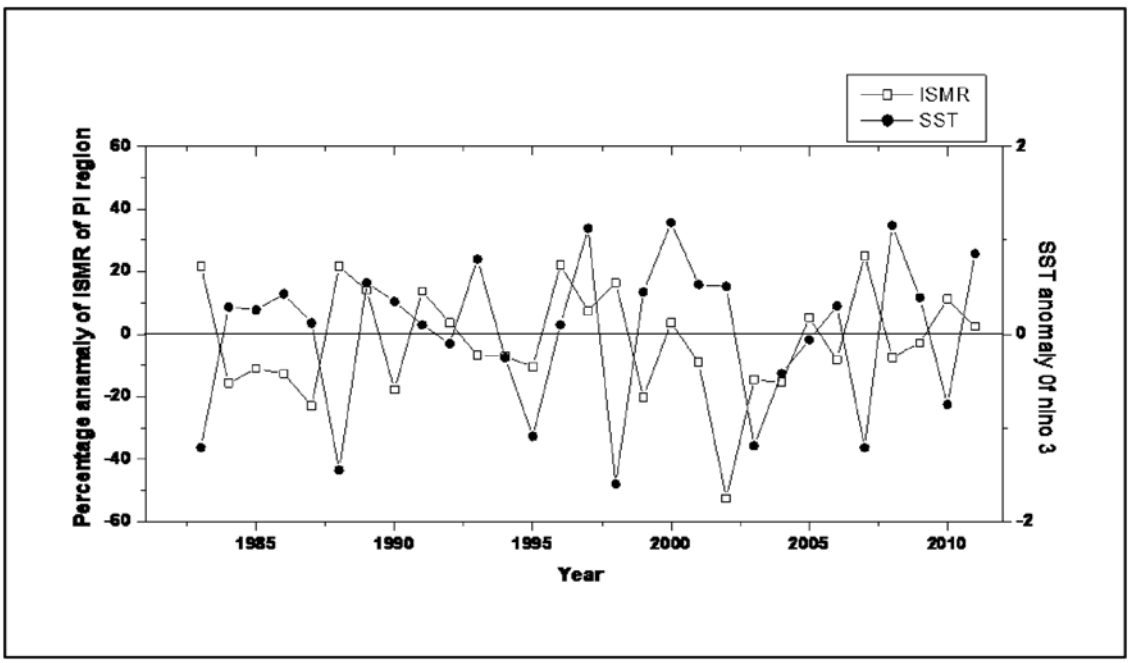

Figure 4. Time series of Peninsular India Region summer monsoon rainfall anomaly and SST anomaly over Nino 3 region during season MAM-DJF: n=29, r= -0.42 (confidence level 95%) 1983-2011.

are observed on regional and local scale. It is important to have a better understanding of changing trends of monsoon rainfall to identify the recent climate variability over micro-scale level. Hence, in the present study we tried to understand the relation between summer monsoon and SST of different Nino regions on over smaller scale. In view of this, correlation coefficient has been computed between summer monsoon rainfall anomaly over all India, core monsoon zone and homogeneous region with SST anomaly of different Nino regions (Nino1+2, Nino3, Nino3.4 and Nino 4). Following generalized conclusions can be drawn from the present study:

Entire Indian Summer Monsoon Rainfall is inversely related to SST anomalies over Nino3, Nino3.4 and Nino4 region for the period previous to spring to winter spring (MAM-DJF). Out of this, distinguished result is obtained for Nino 3 region compared to the other Nino regions for the same time period.

In case of Central North East region, summer monsoon rainfall is inversely associated with SST over Nino 1+2 and Nino 4 for the month of May and over Nino 3 for the month of April. Yet, the relationship between rainfall of the same region and SST anomaly over Nino 3.4 during the spring season MAM, is directly proportional. In this case, the best result is found during month of May for the Nino 4 region.

Inverse relationships are noticed between summer monsoon rainfall of North West region and SST anomalies of both Nino 3 and Nino 3.4 regions during the time period MAM-DJF. While direct relationships are observed between rainfall of this region with SST anomalies of Nino 1+2 and Nino 4 for the month of January and previous winter respectively. In this region, better result is observed during season MAM-DJF with Nino3 region.

SST anomalies of Nino3, Nino3.4 and Nino4 region have negative impact on the summer monsoon rainfall over Peninsular India during the season MAM-DJF. While for Nino 1+2, the SST anomaly for month of January has proportional impact on the summer monsoon rainfall of the same region. Nino 3 region shows best result with Peninsular India in season MAM-DJF.

SST over Nino 1+2, Nino 3, Nino 3.4 and Nino4 did not furnish any significant relation with summer monsoon rainfall over the core region of monsoon, North East and West Central zone.

Behavior of SST anomalies during MAM-DJF (-) over Nino 3, Nino 3.4 and Nino 4 region can be used as precursor of ISMR over whole India.

In Central North East, the summer monsoon rainfall could be predicted statistically with significance using the SST anomaly over Nino4 region for a period previous to May.

SST anomaly in Nino3 region during MAM-DJF, can also act as a predictor for monsoon rainfall over North West region and Peninsular India.

From the above discussion, it may be concluded that the statistical relationship of SST over Nino 3 region during the period MAM-DJF with All India, North West and Peninsular India; and during month of May with Central North East India, can be used for a meaningful prediction of summer monsoon rainfall.

ACKNOWLEDGEMENTS

The authors wish to express sincere thanks to Indian Institute of Tropical Meteorology, Pune for providing the necessary rainfall data and to National Oceanic and Atmospheric Administration (NOAA) for providing monthly SST data. The authors also wish to thank Department of Science and Technology (DST) PURSE grant to carry out the research work.

Compliance with Ethical Standards

The authors declare that they have no conflict of interest and adhere to copyright norms.

REFERENCES

Aldrian, E. and Susanto, R.D., 2003. Identification of three dominant rainfall regions within Indonesia and their relationship to sea surface temperature. Int. J. Climatol., 23, 1435–1452.

Angell, J.K., 1981.Comparison of variations in atmospheric quantities with sea-surface temperature variations in the equatorial eastern Pacific.Mon.Weath. Rev., 109, 230–243.

Bhatla R. and Chattopadhyay, J., 1995.Variability of summer monsoon rainfall and incidence of good and bad monsoon over India.1901–1990. J Sci Res., 45, 79–88.

Bhatla, R., Singh, Sandhya, Mandal, B. and Singh, M., 2016. Association of sea surface temperature over different Nino regions with summer monsoon rainfall over Indo-Gangetic plains.Vayumandal, 42 (1), 21-29.

Chattopadhayay, J. and Bhatla, R., 1993. Sea surface temperature anomaly over equatorial Pacific Ocean as a predictor of Indian summer monsoon rainfall.Vayumandal.23(1–2), 4–6.

Chattopadhayay, J. and Bhatla, R., 2002. Possible influence of QBO on teleconnection relating Indian summer monsoon rainfall and sea surface temperature anomaly across the equatorial Pacific.Int.J.Climtol., 22, 121-127.

Dong, X., 2016. Influences of the Pacific Decadal Oscillation on the East Asian Summer Monsoon in non-ENSO years.Atmos. Sci. Let., 17, 115–120.

Elliott, W.P. and Angell, J.K., 1987. The relation between Indian monsoon rainfall, the Southern Oscillation and hemispheric air and sea temperature: 1884–1984. J. Climatol. Appl. Met. 26, 943–948.

Feldstein, S.B., 2001. Fundamental mechanism of the growth and decay of the PNA teleconnection pattern.Quart.J. Royal Met. Soc., 128 (581), 775-796.

Joaquim, G.P., Mark R. and Uwe, U., 2010.The variable link between PNA and NAO in observations and in multi-century CGCM simulations.Climate Dynamics.36 (1), 337-354.

Krishnan, R. andSugi, M., 2003.Pacific decadal oscillation and variability of the Indian summer monsoon rainfall.Climate Dynamics, 21(3), 233- 242.

Leathers, D.J., Yarnal, B.andPalecki, M.A., 2009.The Pacific North-American teleconnection pattern and United-States climate regional temperature and precipitation associations.J. Clim., 4, 517-528.

Mi-Kyung, S., Kwon, W.T., Baek, H.J., Boo, K.O, Lim, G.H. and Kug, J.S., 2006. A possible impact of the north Atlantic oscillation on the East Asian summer monsoon precipitation.Geophys. Res. Lett., 33, L 21713.

Mooley, D.A. and Parthasarathy, B., 1983. Indian summer monsoon and El Nino. Pure App. Geophys., 121, 339–352.

Mooley, D.A. and Parthasarathy, B., 1984. Indian summer monsoon and east equatorial Pacific sea-surface temperature. Atmosphere-Ocean., 2, 23–35.

Parthasarathy, B., Diaz, H.F. and Eischeid, J.K., 1988. Prediction of all India summer monsoon rainfall with regional and large-scale parameters.J..Geop.Res., 93(D5), 5341–5350.

Rasmusson, E.M. and Carpenter, T.H., 1982. Variations in tropical sea-surface temperature and surface wind fields associated with the Southern Oscillation/El Nino. Mon. Weath. Rev., 110, 354–384.

Rasmusson, E.M. and Carpenter, T.H., 1983. The relationship between eastern equatorial Pacific sea-surface temperature and rainfall over India and Sri Lanka.Mon. Weath. Rev., 111, 517–528.

Shukla, J., 1987. Interannual variability of monsoons. In Monsoons, Fein J. S., Stephens P. L., (eds). 18 Wiley: New York. 399-464.

Sikka, D.R., 1980. Some aspects of large-scale fluctuation of summer monsoon rainfall over India in relation to fluctuations in the planetary and regional scale circulation parameters.Proc. Ind. Acad. Sci. (Earth and Planetary Science), .89, 179-195.

Varikoden, H. and Preethi, B., 2013. Wet and dry years of Indian summer monsoon and itsrelation with Indo-Pacific Sea surface temperatures. Int. J. Climatol., 33, 1761–1771.

Received on: 28.12.18; Revised on: 14.2.19; Accepted on: 8.3.19

J. Ind. Geophys. Union (May 2019)
v.23, no.3, pp: 258-270

Morphological and Elemental Characteristics of Indoor Fine Aerosols in Urban Households at Three Capital Cities of India

Manisha Mishra, Rasna Jawahar V.K., Chanthingla Horam, and Umesh C. Kulshrestha*

School of Environmental Sciences, Jawaharlal Nehru University, New Delhi – 110067.
*Corresponding author: umeshkulshrestha@gmail.com

ABSTRACT

Indoor Air Pollution (IAP) puts people at greater health risks, as compared to outdoor air pollution. Whenever there is poor ambient air quality, it is advised to stay indoors for maximum hours. But in the Indian context, the studies have shown that even in the indoors, the people can not get away from outdoor pollution. To explore such scenario, this study was carried out in the urban houses at three regionally distinct cities of India viz. Delhi, Imphal and Trivandrum. Fine aerosol concentration was found highest in the Delhi households (196.5±48 $\mu g/m^3$), followed by Imphal (173.6±46 $\mu g/m^3$) and Trivandrum (69.4±38 $\mu g/m^3$). Samples were also collected from different parts of the each house, mainly kitchen, living room and bathrooms, to find out activity-wise differences in aerosol characteristics. Despite having larger sources, kitchens were found to be cleaner as compared to other parts in each site. As the morphology and elemental compositions are potential indicators of sources and transport of the pollutants, SEM-EDX analysis was also performed. Soot, fly-ash, flour dust, crustal materials, secondary and biogenic aerosols are the dominant particles present in indoor aerosols. Different activities in each part of the house, have clearly shown its effect on the elemental composition of aerosols. However, despite keeping the study within the four walls of the houses, the corresponding impact of geographical and meteorological conditions of locations has remained prominent at all the sites.

Key Words: Indoor Air Pollution, Fine Aerosols, Urban households, Morphology and Elemental composition, Environment.

INTRODUCTION

Growing air pollution over the urban areas has shown increasing health risks related to respiratory and cardiovascular systems (Pope, 2000). Emission of various harmful pollutants due to burning of fossil fuel and biofuel, degrades air quality and thus damages the human health. The most important are particulates, CO, NO_x, SO_x, PAHs, Arsenic, Fluoride (primarily from coal burning), Benzene, Formaldehyde and polycyclic organic matter, including carcinogens such as benzo(a)pyrene. Apart from these, particles with diameter less than 10 μm (PM_{10}) and particularly those below 2.5 μm in diameter ($PM_{2.5}$), can penetrate deep into the lungs and appear to have the greatest potential for damaging the health (Brunekreef and Holgate, 2002; Franklin et al., 2008). Indoor Air Pollution is observed as a major contributor to the global burden of disease (GBD) in the epidemiological studies and is considered as the second important contributor to ill health worldwide (WHO, World Health Report, 2002; Nel, 2005). The primary factors for this include a variety of indoor sources, higher levels of some toxic pollutants, the amount of time spent indoors, etc. In modern urbane societies, where people spend more than 80% of their time inside the four walls of home, school and offices, they tend to become more susceptible to such health risks. Indoor pollution is also an important factor in causing Acute Lower Respiratory Infections (ALRI), including respiratory problems in elderly people and pneumonia in children (Mishra, 2003; Franklin, 2007). This burden of diseases in children becomes disproportionately high in developing countries due to complex sources of pollution in urban settlements, where the improper heating, ventilating and air conditioning (HVAC) systems along with infiltration of outdoor harmful pollutants make the condition more severe (Spengler and Sexton, 1983; Bruce et al., 2000, Pegas et al., 2012; Salma et al., 2013; Singh et al., 2014).

In developing countries, solid fuels, including both biomass and coal, have been identified as primary energy sources with very high emission of harmful gases and particles used for cooking and heating purposes (Ezzati and Kammen, 2002). Wood, dung cakes, charcoal, crop residues and dry leaves are some of the most common fuels used for heating and cooking in India, which emit excessive harmful particles and gases (Kim et al., 2011; Wiedinmyer et al., 2014). In some of the rural areas, farmers have the option of utilizing biomass through digester and turning them into biogas, which can be used more efficiently for cooking and heating. However, modern fuels such as liquefied petroleum gas (LPG), having higher energy content per kilogram of fuel, are used for cooking purposes in urban houses in most of the parts of India. Without any harmful emissions, they are also considered as cleanest form of energy. It has been estimated that cooking with LPG has almost five times higher efficiency (60%) as compared to biomass burnt (12%) in traditional stoves, with least

pollution (D'sa and Murthy, 2004). Such kinds of efficient energy sources are very crucial for maintaining indoor air quality and sustainability in both urban and rural areas.

Some of the indoor activities contribute to the higher number of ultrafine particles and lead to an increase in indoor aerosol concentrations. Cooking (frying, baking, barbequing,grilling, boiling, toasting, etc.), dusting, washing, cleaning products, room fresheners, perfume spray, hair spray, gas-powered clothes dryers, tobacco smoke, candle and incense burning, furniture polish containing terpenes, photocopiers, laser printers, etc., are identified as major sources of indoor origin (Abt et al., 2000; Dennekamp et al., 2001). Whereas, coarse aerosol generally comes from dusting, sweeping, human movement, hovering, re-suspension from clothes (folding and unfolding of blankets, bed sheets, carpets) sitting on upholstered furniture, washing powder residues (zeolite),animal hairs, bioaerosols, etc. (Owen et al., 1992; Abt et al., 2000; Long et al., 2000; Ferro et al., 2004; Koistinen et al., 2004). However, most of the Indian houses have open window systems which mean that the indoor environment is also affected by the outdoor sources and air quality.

The pollution sources, its concentration, exposure levels vary within the households, depending upon the inside activities (Balasubramanian and Lee, 2007). However, size, morphology and elemental composition play crucial roles in deciding the toxicity of the aerosols. This study has mainly focused on the indoor aerosols of urban households. Aerosol loadings within the different parts of the houses located at three geographically distinct regions and their morphological and elemental composition have been reported to improve our understanding regarding the likely sources of indoor air pollution with respect to geography and distinct indoor characteristics.

METHODOLOGY

Description of Sampling Sites

This study was carried out in the three capital cities of India viz. Delhi, Imphal and Trivandrum (Figure 1). The site description is given below.

Delhi

National Capital Trritory of Delhi, located at 28° 36′ 36″ N, 77° 13′ 48″ E, has elevation of ~240 m above the mean sea level. Delhi ranks second in population, having population density 11,297 per square km with land area 1,484 square km. Delhi has a subtropical climate, where dry weather condition prevails during most part of the year except monsoon season. Delhi has a variety of areas which differ in traffic and population densities, number of industrial sites, land use patterns, etc. The samples were collected from highly populated urban localities of north and south Delhi in October month, having mean temperature 26°C. The kitchen samples were collected from houses that are ventilated poorly and rarely used exhaust fans. The cooking time was from 6 am to 8 pm and the oil used was mustard oil. The bathrooms were poorly ventilated and all of them had room fresheners, in addition to the toiletries. The living rooms had windows, but mostly closed. The houses were away from main roads, but all of them were in a highly populated residential area. Dust re-suspension occurs on a daily basis. The construction activities were also observed in proximity to the respective sampling sites.

Imphal

Imphal is located around 24°48′28″ N, 93°56′39″ E and has an altitude of ~784 m above the mean sea level. It has a population density of 847 per square km with a land area ~558 square km. Imphal is characterized by hot and humid rainy conditions during the summer months and cool and dry conditions, during the winter. The samples were collected from different urban households in September month having mean temperature 25°C. The selected houses are properly ventilated with large windows, though exhausts are absent. The kitchens are active from 7 AM to 8 PM. Generally, the vegetable oil is used for cooking. The bathrooms were poorly ventilated with small, partially opened windows. The living rooms are large and close to kitchens. Two of the selected houses are close to main roads while, one is away from the main road.

Trivandrum

Trivandrum is located at 8°29′7″ N, 76°56′57″E, ~18m above mean sea level. It has a population density 4500 per square km, spread over 215 square km. It is characterized by hot tropical climate. This district stretches for about 78 km along the Arabian Sea on the west. The samples were collected from urban households in September month having a mean temperature of 24°C. The houses are properly ventilated with windows, though exhausts are absent. The kitchens are active from 6 AM to 8 PM. The coconut oil is mostly used as cooking midium. The bathrooms are poorly ventilated with small, partially opened windows. The living rooms are not spacious but, all of them were attached to the kitchen. Three of the houses were close to busy roads and one was very close to NH 47.

Collection of Samples

The indoor aerosol samples were collected on 47mm Whatman Quartz Filter (QMA), using 47 mm filter holder, connected to a low volume vacuum pump through a silicon tube operated at the flow rate between 28-30

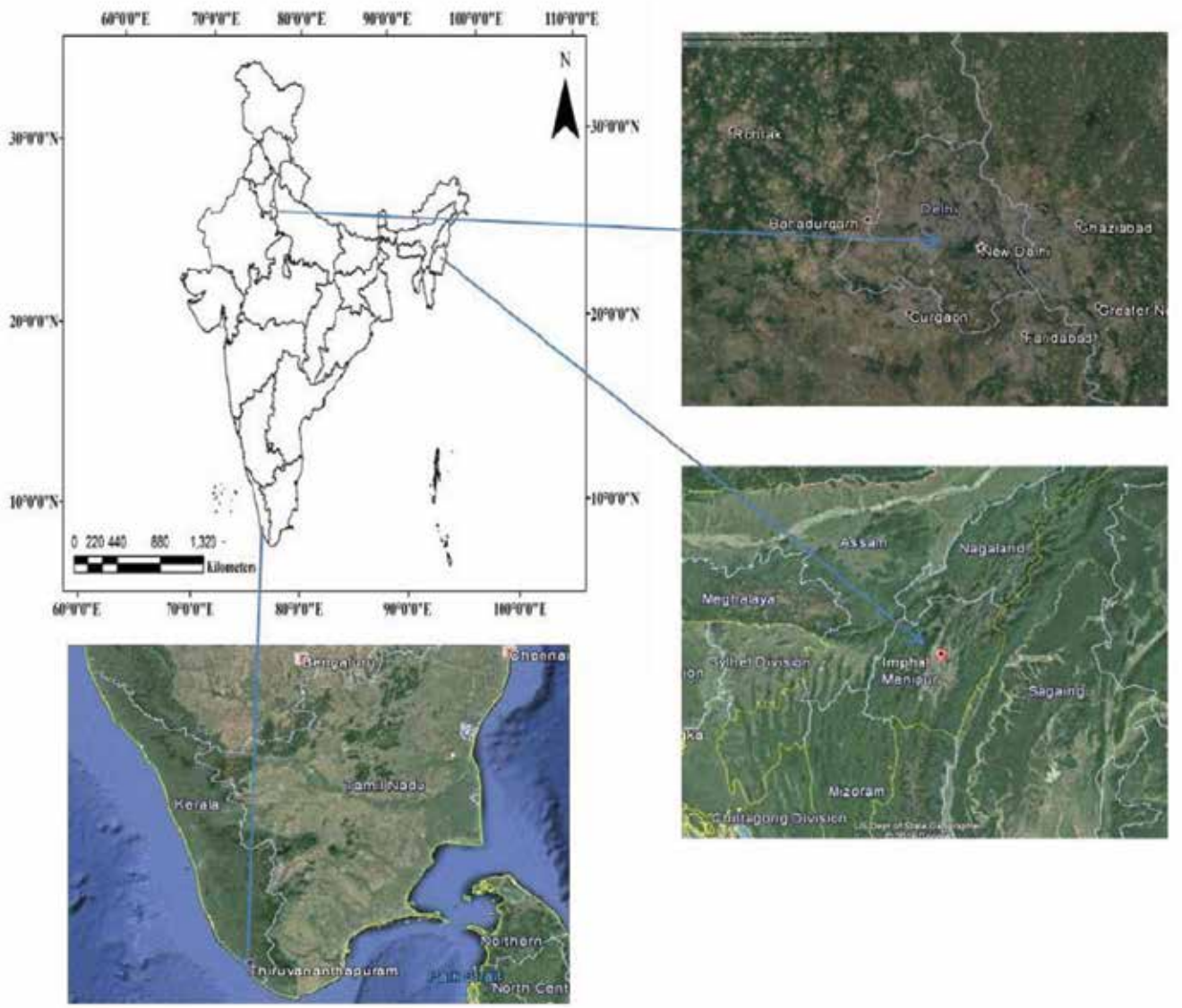

Figure 1. Description of Sampling sites.

LPM. Sampling was conducted randomly for eight hours from three different houses within a week from three capital cities. In Imphal and Trivandrum, the samples were collected during the second and third week of September 2016 and in Delhi during the last week of October and First week of November 2016. In order to get an impact of inside activities on aerosol composition, sampling was conducted in kitchen, living room and bathroom areas in each selected house. After the collection, samples were carefully stored in 60 mm petri dishes at room temperature, since the study does not include volatile compounds. Each filter was kept in desiccator for 24 hours before taking initial and final weights. Filters were measured gravimetrically before and after the sampling using 0.0001g sensitivity microbalance (Mettler Toledo, ME204) to calculate the indoor aerosol loading. One field blank from each site was also analyzed in order to avoid over/under estimation during the sampling and analysis. A total of 25 samples was collected from different sites.

Morphological and elemental analysis of samples

For surface morphological and elemental analysis of the indoor aerosols, sample filters were analyzed using Scanning Electron Microscope (SEM) with Energy Dispersive Spectroscopy (EDS) (Carl Zeiss AG- EVO® 40 Series Model). In order to analyze the samples, metallic stubs of 15mm diameter were cleaned with acetone, which was followed by sticking of double sided carbon tape on its flat upper surface. About 0.5 cm^2 of filters were cut with an iron punch and stuck on the tape. For the elemental analysis, a thin layer of gold coating was

done on the samples by Sputter Coater–Polaron (SC7640) material, which converts the non-conductive elements into conductive ones (Mishra and Kulshrestha; 2017).

According to working principle, significant amount of kinetic energy carried by accelerating electrons upon experiencing a deceleration in the solid sample, on account of electron-sample interactions, dissipates a variety of signals. The signals include secondary electrons (SE, that produce SEM image), back scattered electrons (BSE), X-rays (used for elemental analysis), visible light (cathodoluminescence, CL), diffracted back scattered electrons (EBSD which is used for orientation and crystal structure determination) and heat. SE and BSE are commonly used for imaging samples. Of these, the former is important for showing morphology and topography on samples, the latter is significant for illustrating contrasts in composition in multiphase samples. The inelastic collision of the incident electrons with electrons in discrete orbital of atoms in the sample leads to X-ray generation. The X-rays of fixed wavelength are emitted by electrons returning from higher energy states to lower energy states. Thus, for each element in a mineral, characteristic X-rays are produced. Since SEM analysis is a "non-destructive" process where electron interactions do not cause loss of sample, it becomes possible to repeatedly analyze the same sample material.

Another notable feature of SEM is its capability to perform analysis of selected point locations on the sample, for it enables a qualitative or semi-quantitative determination of chemical compositions (using EDS) crystal structures, and crystal orientations (using EBDS). Using the conventional SEM techniques area of images ranging from 1 cm to 5 microns in width can be analyzed. The magnification range of SEM is about 20X to approx 30,000X with spatial resolution of about 50 nm to 100 nm.

RESULTS AND DISCUSSION

Average Aerosol loadings at three Sites

Aerosol loadings were calculated gravimetrically by weighing the quartz filters before and after sample collection using following formula.

$$M = m2 - m1$$

Where, m_1 and m_2 are the initial and final weight of samples (in mg) respectively. Depending upon the site, there have been variations in the average aerosol loading at three sites (Table 1).

Among all the samples, the highest aerosol loading is found in Delhi samples, with an average of 196.5±48$\mu g/m^3$. This may be attributed to various indoor sources such as cooking, cleaning, use of cleaning liquids, tobacco smoking along with the influence of highly polluted outdoors and their infiltration through the ventilation system of the houses. Delhi, being one of the principal polluted cities of the world, witnesses contribution to the aerosol concentrations from outdoor sources (Table 2) as well, such as high levels of vehicular and industrial emissions, solid waste burning, construction and demolition activities, resuspension of soil and road dust and biomass burning (Pant et al., 2015; Mishra and Kulshrestha, 2017). Delhi is followed by Imphal having aerosol loading with a mean value of 173.6±46.7$\mu g/m^3$. Air pollution due to dust particle was the highest in Imphal among all the North-eastern cities (Sangai Express, 29/3/2011). Construction works and particulate matter emitted from various brick fields surrounding the city may be other possible reasons for the high loading in addition to indoor sources (Balasubramanian and Lee, 2007; Quang et al., 2013). Trivandrum showed the least aerosol loading 69.4±38.2$\mu g/$

Table 1. Indoor aerosol concentration (in μg/m3) in urban households at three capital cities.

	Delhi	Imphal	Trivandrum
Mean	196.5	173.6	69.4
Minimum	27.8	4.6	4.6
Maximum	365.7	393.5	328.7
Standard Error	48.0	46.7	38.2

Table 2. Meteorological parameters and outdoor Average particulate and gaseous pollutant concentrations in sampling duration at three cities of India taken from IMD and CPCB.

Parameters	Delhi	Imphal	Trivandrum
Temperature (^oC)	26	24	28
Relative Humidity (%)	61	84	80
PM_{10} ($\mu g/m^3$)	167±90	NA	63±12
$PM_{2.5}$ ($\mu g/m^3$)	134±48	NA	28±9
SO_2 ($\mu g/m^3$)	19±9	NA	9±4
NO_2 ($\mu g/m^3$)	88±37	NA	7±2
CO (mg/m^3)	3±2	NA	1±0.5

NA= not available.

m^3 despite being one of the highly urbanized cities of Kerala. It may be explained by the meteorological impact of the proximity to the Arabian Sea that causes the aerosols in the atmosphere to wash out because of the high humid conditions (Table 2). This process lessens the aerosol concentration in the outdoor atmosphere which, in turn, affects the indoor aerosol concentration.

Aerosol Loading within the Households at each site

When analyzed for different parts of the houses, aerosol loading varied significantly from one part to another as shown in Figure 2.

Delhi: The average highest loading (305 $\mu g/m^3$) was found among bathroom samples in Delhi, which is very high as compared to outdoors. This may be due to poor ventilation and activities such as washing, cleaning (using detergents and other cleaning materials) etc. Also the presence of high humid conditions in bathrooms may result in the dissolution and aggregation of various aerosols and suspension for a long term. Air fresheners were used in all the three bathrooms which might have contributed to the emissions of VOCs directly and /or the formation of secondary reaction products indirectly. The bathrooms at all the sites were attached to bedrooms and hence human activities such as dusting, cleaning, vacuuming might have an effect on the aerosol loading. The living room aerosol loading (157.4 $\mu g/m^3$) is higher than that in kitchen. This may be because people remain active for maximum time in Living Rooms and their greater interface with the outdoor environment. The living room is exposed to cooking emissions from kitchen (Balasubramanian and Lee, 2007). Since all the living rooms were adjacent or attached to kitchens at respective homes, the possibility of exposure to cooking-induced emissions is higher. Kitchen samples showed the least loading (126.5 $\mu g/m^3$). This may be directly attributed to the use of exhausts during the peak cooking hours.

Imphal: The highest loading (282.4 $\mu g/m^3$) is found in living rooms followed by bathrooms (196 $\mu g/m^3$) and kitchen (78.7 $\mu g/m^3$). This may be attributed to the diffusion of aerosols from kitchen as they were very much connected and there are no doors to separate each other and also to the infiltration of outdoor aerosols. The bathrooms were poorly ventilated with a small window and exhaust systems were absent. In addition, the cleaning products used were locally made which may have an impact on the chemical characteristics of the aerosols. The lowest loading in kitchen can be clearly attributed to the proper ventilation with large windows, opened during peak cooking hours.

Trivandrum: The highest loading was found in bathroom samples (148.2$\mu g/m^3$) followed by living room (41.7$\mu g/m^3$) and kitchen (9.3 $\mu g/m^3$). All the bathrooms were poorly ventilated and exhaust systems were absent. The humid conditions in the bathrooms might have enhanced the dissolution and dispersion of aerosols for long periods. The living rooms remained active almost whole day and properly ventilated and kitchens were also ventilated with windows, opened during peak hours of cooking. Two of the households were also surrounded by vegetation that may act as a barrier to outdoor dust. Due to humid climate even the outdoor aerosol concentrations remain very less in Trivandrum, which clearly affect indoors too (Viswanadham and Santosh,1989).

The lowest aerosol loading in kitchens of Trivandrum and Imphal can be clearly attributed to the proper ventilation during peak cooking hours while the highest loading in Delhi can be due to poor ventilation as well as infiltration from outdoor concentrations. The higher loading in living rooms of Imphal and Delhi can be attributed to the higher exposure of living rooms to outdoor air as well as proximity to kitchen while the lower loading of the same in Trivandrum can be mainly due to the effect

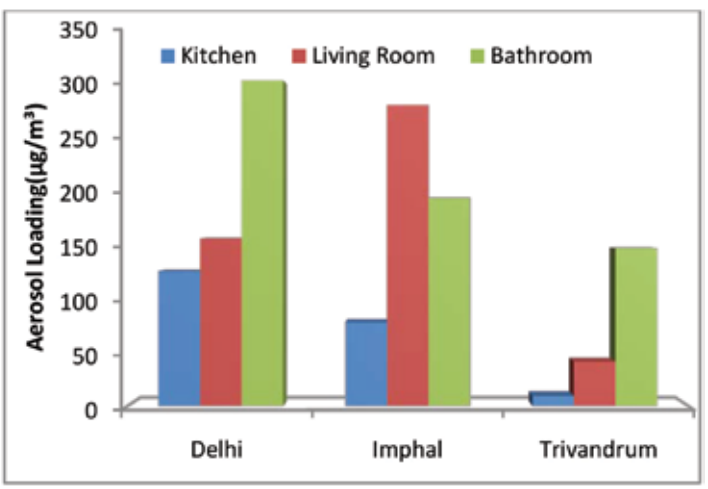

Figure 2. Average aerosol loading of different parts within the households at each location.

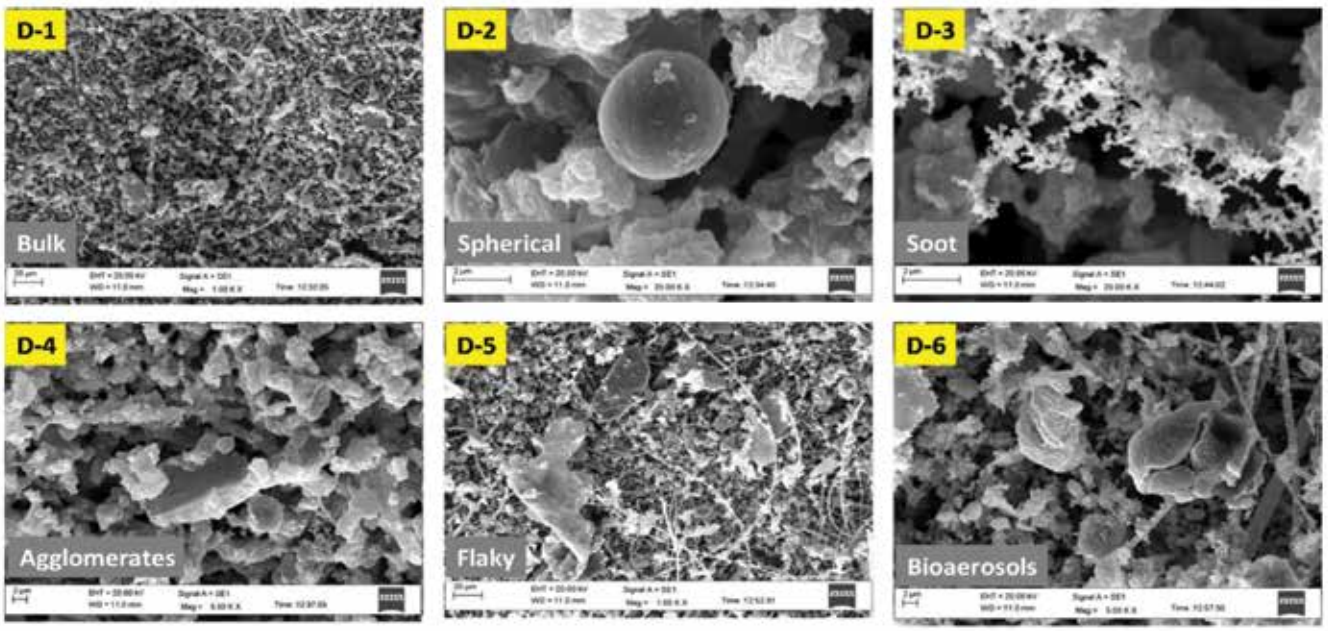

Figure 3. SEM images of indoor particles in urban households of Delhi.

of local climate conditions, which not only affect ambient concentration but also indoor levels. The comparatively higher aerosol loading in bathrooms across all the three sites can be due to the poor ventilation which explains the prolonged re suspension of aerosols caused by activities like cleaning, bathing, washing, spraying etc.

Morphological Analysis of Aerosols at three Sites

Delhi: Most of the images of indoor aerosols in Delhi (figure 3 D-1) were either spherical or aggregates of irregular shaped particles. The spherical shaped (D-2) particles can be indicative of inorganic fly ash particles rich in calcium, silicon and iron. The chain like aggregates (D-3) can be soot particles, which may be originated from incomplete combustion of fossil fuel and organic matter and hence its source seems to be outdoors as the cooking fuel used is LPG and not biomass. Higher coagulation of particles (D-4) mostly caused by reactive gases and VOCs emitted from indoor activities such as cooking, cleaning, sweeping, paints, solvents etc. (Srivastava and Jain, 2007). Irregular shaped large sized particles show the presence of aerosols from crustal emissions (D-5). In Delhi, the crustal materials are majorly ferruginous quartzite, consisting of silica and iron and are rich in alkaline ($CaCO_3$) dust. Image (D-6) also shows the presence of biogenic particles, which could be attributed to the higher levels of bioaerosols during post monsoon in the indoors as the sampling was conducted during October and November (Lal et al., 2013). The aerosols with flaky appearance can be particles rich in oxygen and carbon, whose source can be indoor activities like cooking, boiling etc., which may further undergo dissolution or gas-to-particle phase conversion. In short, it is very clear that Delhi's indoors are very much representative of its outdoors (Srivastava and Jain, 2003).

Imphal: Most of the particles show very well defined shapes (Figure 4) indicating it's biogenic nature or Carbon–Oxygen rich composition (Pachauri et al., 2013; Mishra et al., 2015). The triangular flaky and crystalline shape (I-2) gives clue about the presence of quartzite which is basically geologic in origin. There are chain aggregates of soot aerosols (I-3) showing the biomass burning in nearby locations. Aging of particles with rough surface (I-4) shows re-entrainment of existing particles in the indoor environment. Bioaerosls (I-5) were found dominated in the urban houses of Imphal due to high vegetation in surrounding areas. Particles of smooth oval shape were also observed (I-6), which are generally found to be rich in C and O, and emitted from bio-fuel burning.

Trivandrum: A combination of different kinds of particles (T-1) is observed in the SEM images of Trivandrum (Figure 5). Particles of elongated triangular shape (T-2) and soot aggregates (T-3) showing the infiltration of outdoor aerosols through the gaps of the doors and windows of the houses, as they don't have any such sources inside. Big aged carbon fractal comprising of carbon monomers (T-4) shows the presence of particles emitted from combustion/vehicular emission activities. Mishra et al. (2015) have found that fresh carbon fractals (open long chains) are released into the atmosphere which reside for a long time and form close fractals (closed chain compact fractal) due to surface tension and particle dynamics. Irregular flattened particles (T-5) indicating the presence of silicon rich aerosols. The presence of aged sea salt (T-6) has to be considered very strongly as Trivandrum is a coastal region.

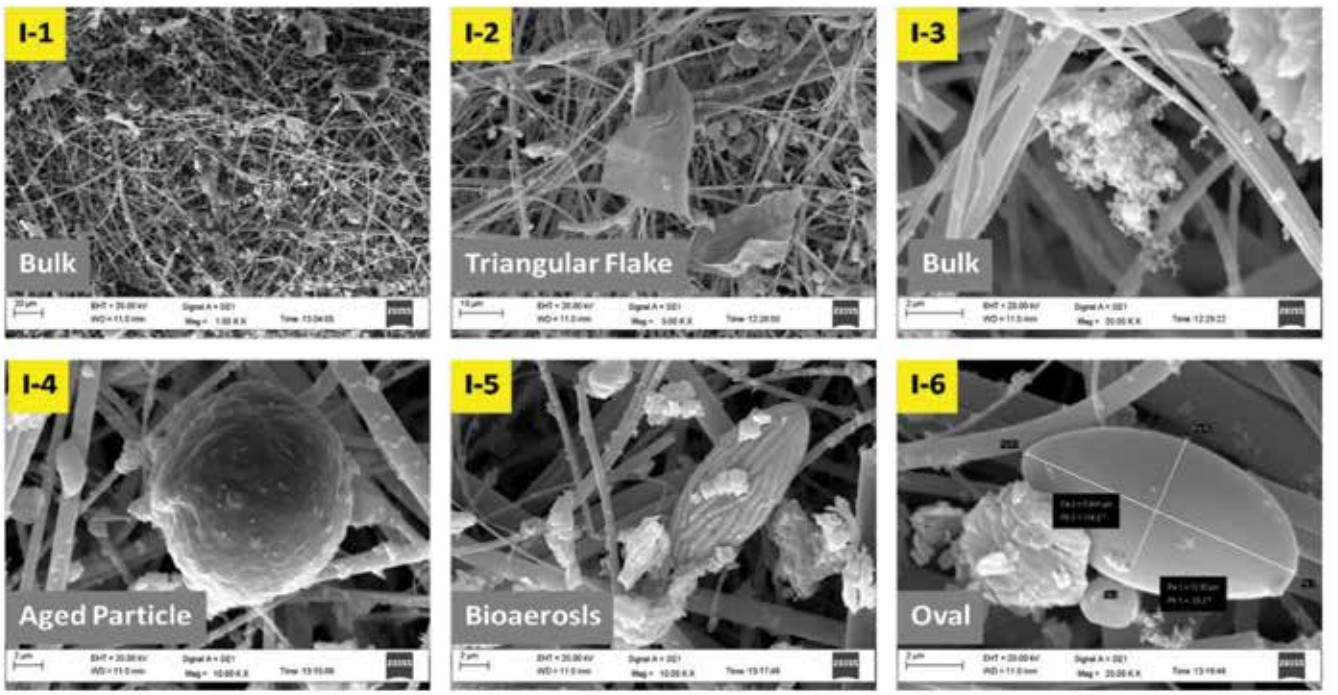

Figure 4. SEM images of indoor particles in urban households of Imphal.

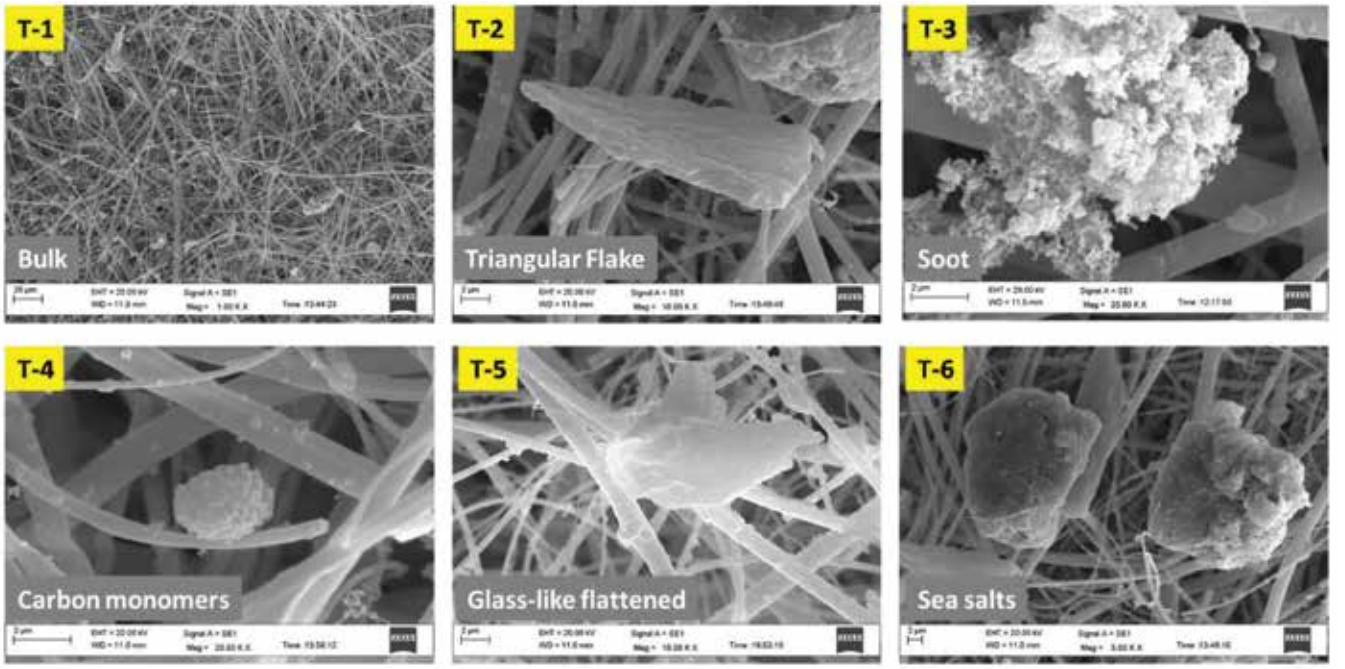

Figure 5. SEM images of indoor particles in urban households of Imphal.

The morphological analysis of selected samples from each site shows the presence of both regular and irregular shaped particles. The majority of the particles were found in the fine mode, while a few belonged to coarse mode. Most of the particles were found as agglomerates or aggregates and irregular shapes, whereas some found in flaky, crystalline, spherical and chain like shapes. The particles forming the aggregates or agglomerates consist of various volatile organics and soluble components formed by gas to particle conversion. Volatile compounds emitted from indoor activities such as cooking, cleaning, bathing, etc. also tend to get adsorbed onto the surface of existing air particles forming agglomerates. Such particles may also formed by the aging and their resuspension in the air.

Table 3. Relative Percentage of elements present in the indoor aerosol in different parts of the House (LR=Living Room, K= Kitchen and B=Bathroom; ND= Not Detectable).

Sites	Part of House	Atomic Percentage of various elements in fine aerosols										
		O	**C**	**Al**	**Ca**	**Mg**	**S**	**Cl**	**Zn**	**Na**	**K**	**Fe**
Delhi	**K**	37.2	**41.7**	8.7	2.7	0.4	0.7	3.1	1.4	0.8	1.4	1.9
	LR	31.5	**50.3**	8.9	3.4	0.4	0.5	0.3	1.9	0.2	1.0	1.6
	B	23.6	**58.1**	8.5	2.3	0.3	1.1	2.0	1.2	0.2	1.5	1.2
Imphal	**K**	**55.6**	15.7	22.7	0.4	0.1	ND	ND	2.6	0.1	0.3	2.4
	LR	**63.5**	13.2	20.1	ND	0.4	ND	ND	1.1	0.4	ND	1.1
	B	**44.7**	34.3	16.0	0.4	0.6	ND	ND	1.5	0.5	ND	2.0
Trivandrum	**K**	33.2	**52.9**	11.0	0.9	0.2	ND	ND	1.3	ND	ND	0.6
	LR	**64.4**	7.2	22.9	ND	ND	ND	ND	3.8	0.6	ND	1.1
	B	**46.9**	30.7	17.6	2.2	ND	ND	ND	1.2	ND	ND	1.3

Smooth spherical particles show the presence of fly ash particles in the indoor environment (Pachauri et al., 2013). Since fly ash is generated from industrial activities, their dominance indicates that indoor air is very much affected by the outdoor air quality. Chain-like complex structures in the aerosol samples suggest the presence of soot and carbonaceous particles suspended inside the houses (Posfai et al., 2004; Sachdeva and Attri, 2008; Tumolva et al., 2010). Irregular particles with rough surface are primarily the windblown soil-dust generated from unpaved roads, construction activities and building materials (Jiao, 2006; Pachauri et al., 2013). Apart from this, bioaerosols were also observed in the images which again could be attributed to the infiltration of contaminated outdoor air through open areas of the houses (Batterman and Burge, 1995). Analysis of various shapes of the indoor aerosols clearly shows that irrespective of the geographical locations of the houses the indoor air quality is largely dependent on the infiltration and ventilation rate of outdoor air (Leung, 2015).

Elemental Analysis of Aerosols at three sites

The elemental composition of the indoor aerosol was analyzed with the help of SEM–EDS. EDS analysis was carried out for one blank filter (Figure 6) and samples each area of the houses from all the three sites. Since the quartz filter is composed of silicon and oxygen (SiO_2), thus showing intensity peaks of only Si and O. Among various elements, oxygen and carbon were found as most dominant element contributing about three quarters of total composition at all the sites (Table 3).

Delhi: The order of elemental composition in Delhi Kitchen samples was C> O> Al>Cl>Ca> Fe> K= Zn>Na>S (Figure 7a). The order of elemental composition in Delhi Living Room samples was C> O>Al>Ca>Zn>Fe>K>Mg>S>Cl>Na (Figure 7b). The high percentage of carbon and oxygen in the kitchen show the influence of cooking activities, VOCs formed during cooking, their subsequent diffusion and conversion into particles. The aluminium, calcium and other elements may be of outdoor origin. Their sources may be vehicular and industrial emissions, biomass burning, dust re-suspension etc. The similar trend can be attributed to the proximity of kitchen and living rooms and the mutual dispersion of particles and gases. The percentage of carbon in living room is higher than that in kitchen which may be due to the possibility of infiltration of outdoor particles. The order of elemental composition in Delhi Bathroom samples was C> O> Al> Ca>Cl>K> Zn=Fe>S> Mg> Na (Figure 7c). Magnesium and sodium showed negligibly small percentage. The same trend as in kitchen and living room shows the similarity in indoor air quality although the sources responsible are different. The percentage of carbon is the highest in the bathroom which may be attributed to the formation of SOCs from VOCs and its prolonged persistence due to poor air exchange.

Imphal: The elemental composition of Kitchen samples in Imphal urban houses showed the trend O> Al>C> Zn> Fe> Ca> K> Mg=Na (Figure 8a). The elemental composition of Living Room samples showed the trend O> Al> C> Fe=Zn> Mg=Na (Figure 8b). The significant percentage of aluminium shows its crustal origin and the influence of ambient air in the indoor environment. Carbon content can be attributed to cooking and cleaning in Kitchens. The presence of zinc can be traced from vehicle emissions and iron can be traced from geologic sources, might infiltrate through the large windows of the houses (Kulshrestha et al., 2014). The similar trend of kitchen and Living Rooms again can be attributed to its connectivity

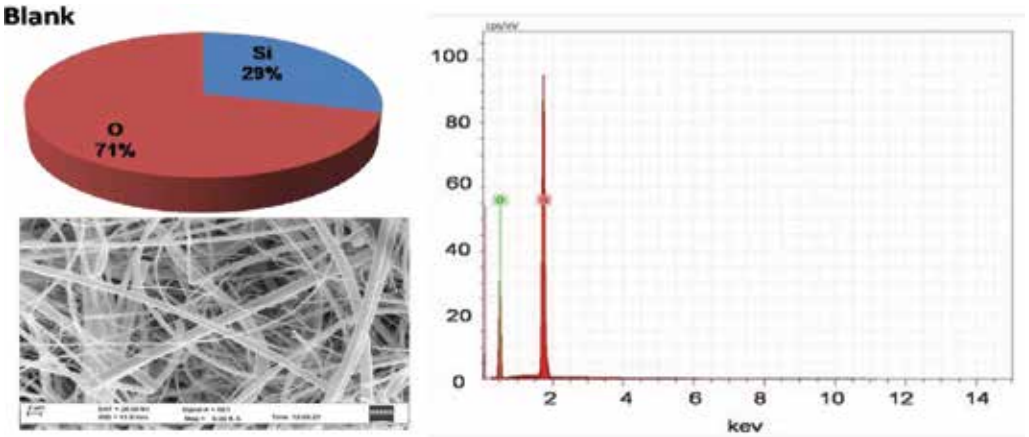

Figure 6. Elemental analysis of blank quartz filter.

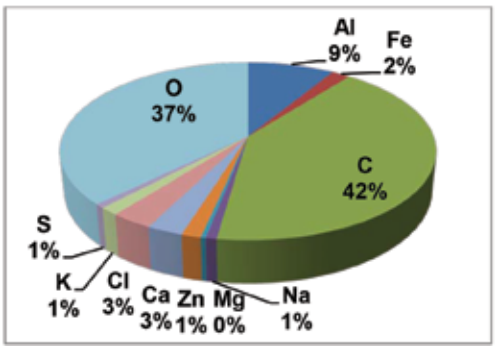

Figure 7a. Elemental Analysis of Delhi Kitchen (DK) samples.

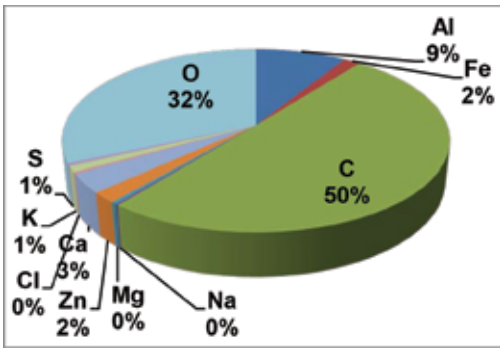

Figure 7b. Elemental analysis of Delhi Living Room (DLR) samples.

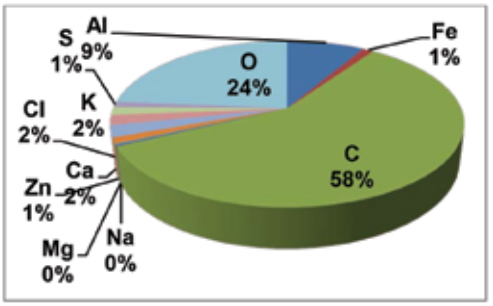

Figure 7c. Elemental Analysis of Delhi Bathroom (DB) samples.

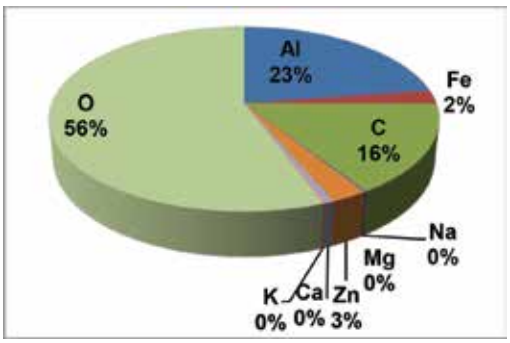

Figure 8a. Elemental Analysis of Imphal Kitchen (IK) samples.

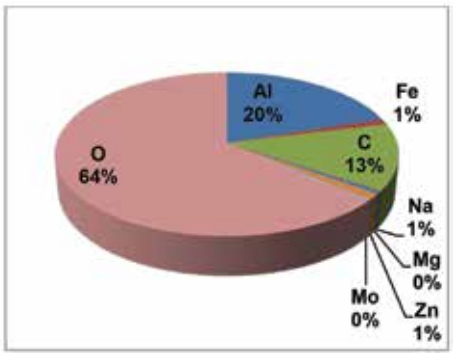

Figure 8b. Elemental Analysis of Imphal Living Room (ILR) samples.

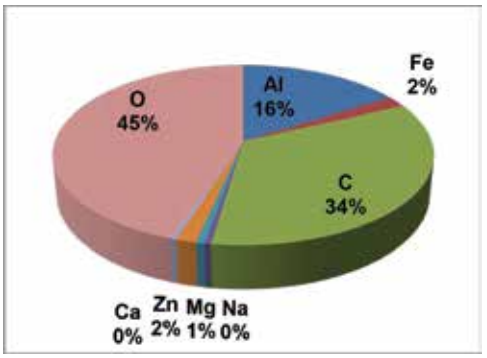

Figure 8c. Elemental Analysis of Imphal Bathroom (IB) samples.

to the kitchen. The elemental composition of bathroom samples showed the trend O> C> Al> Fe>Zn> Mg> Na> Ca (Figure 8c). The relatively higher percentage of carbon in bathroom can be attributed to formation of SOCs from VOCs emitted from various activities like washing, cleaning, usage of air fresheners etc.

Trivandrum*:* The elemental composition showed the trend C> O> Al> Zn> Ca> Fe> Mg (Figure 9a). Cooking may be primarily responsible high percentage of carbon and oxygen. It has been observed that while unflued gas heater operation, indoor concentration for volatile organic compounds exceeds the outdoor concentration (Jurvelin et al., 2001; Adgate et al., 2004; Ferrari et al., 2004). The use of coconut oil for frying might be the reason of higher carbon content in the Trivandrum Kitchens. Other elements found in the samples might be originated from indoor activities such as cleaning, paint dust as well as infiltration of outdoor aerosols. The elemental composition showed the trend O> Al> C> Zn>Fe> Na (Figure 9b). Living Room has lesser carbon as compared to Aluminium owing to the influence of suspended dust. For other elements pattern was similar to kitchen, which may be due to the connectivity of living rooms to kitchen. The elemental composition showed the trend O> C> Al> Ca>Fe> Zn (Figure 9c). The comparatively higher carbon percentage in bathroom, than living room, may be due to the formation of SOCs from various sources like detergents, air fresheners, cleaning products etc.

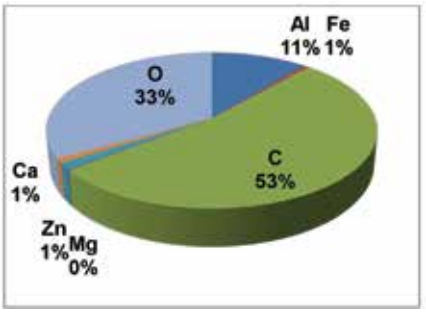

Figure 9a. Elemental Analysis of Trivandrum Kitchen (TK) samples.

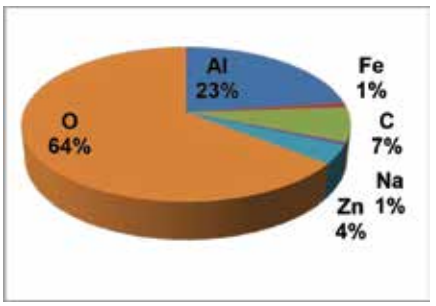

Figure 9b. Elemental Analysis of Trivandrum Living Room (TLR) samples.

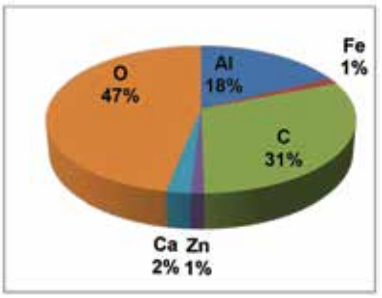

Figure 9c. Elemental Analysis of Trivandrum Bathroom (TB) samples.

The results show that indoor aerosols in all the parts of the houses have the highest percentage of carbonaceous aerosols, irrespective of regional differences in their locations. Almost every sample consisted of some amount of Al, Fe, and Zn, whereas Ca, Mg, S, K and Na were present sporadically across different sites. Following O and C, aluminium (Al) contributed more than any other element showing the outdoor influence on indoor aerosols as primarily aluminium comes from crustal or industrial sources. The analysis clearly indicates the outdoor effects on the indoor aerosol composition.

CONCLUSIONS

Delhi, being one of the most densely populated metropolitan cities in the world, is infamous for its deteriorating air quality because of various anthropogenic sources. Even the indoor spaces in Delhi are not immune from the alarming pollution in the outdoor spaces.The average highest fine indoor aerosol loading was in Delhi, followed by Imphal and Trivandrum. This is very much in accordance with the studies until now. The outdoors of Delhi influences the indoors greatly as many aerosol components are exclusively outdoors in origin like aluminum, iron, soot, fly ash, etc. However, the absence of outdoor data of all the locations during the same hours remained the limitations of the study.

In the morphological characterization, most of the samples represented soot, fly ash, crustal materials, floor-dust in common and a few represented biogenic aerosols too. The presence of carbon and oxygen rich components indicate the influence of both indoor sources such as cooking, VOCs from various consumer products as well as outdoor sources through the infiltration of outdoor

components. The different activities in each part of the houses have clearly shown its effect on the elemental composition of aerosols in urban households. Poor ventilation in Bathrooms, higher activities in Living rooms and Kitchen exhaust system/ open windows have their significance in the aerosol levels in the indoor environment. Keeping these aside, the impact of outdoor sources also remained prominent at all the sites.

The study shows that not only outdoors but our indoors are also contaminated, or more precisely polluted, putting our lives under the silent threat. Higher concentration of PM in indoor environment is more dangerous as compared to outdoor because of the confined space of the houses, which do not allow the dispersion of the pollutants causing severe health impacts. The study reminds that our urban indoors require a very efficient air exchange mechanism that may withdraw contaminated air and may pass contamination-free filtered clean air. Plantation around the houses could act as a better alternative to reduce outdoor pollution. Delhi being most affected, should strictly implement air quality guidelines for both indoors and outdoors. The other two sites being vulnerable, needs to act foresightedly to protect indoor environment and life from serious deterioration.

ACKNOWLEDGEMENT

We sincerely thank the financial support received from Jawaharlal Nehru University, New Delhi, and CSIR, to conduct this research work. Analytical assistance provided by DST-PURSE, and Advance Instrumentation Research Facility (AIRF), JNU is gratefully acknowledged.

Compliance with Ethical Standards

The authors declare that they have no conflict of interest and adhere to copyright norms.

REFERENCES

Abt, E., Suh, H.H., Allen, G. and Koutrakis, P., 2000. Characterization of indoor particle sources: A study conducted in the metropolitan Boston area. Environmental health perspectives, 108(1), 35.

Adgate, J.L., Church, T.R., Ryan, A.D., Ramachandran, G., Fredrickson, A.L., Stock, T.H. and Sexton, K., 2004. Outdoor, indoor, and personal exposure to VOCs in children. Environmental health perspectives, 112(14), 1386.

Balasubramanian, R. and Lee, S.S., 2007. Characteristics of indoor aerosols in residential homes in urban locations: a case study in Singapore. J. Air and Waste Manag. Assn, 57(8), 981-990.

Batterman, S.A. and Burge, H., 1995. HVAC systems as emission sources affecting indoor air quality: a critical review. HVAC and R Res., 1(1), 61-78.

Bruce, N., Perez-Padilla, R. and Albalak, R., 2000. Indoor air pollution in developing countries: a major environmental and public health challenge. Bulletin of the World Health organization, 78, 1078-1092.

Brunekreef, B. and Holgate, S.T., 2002. Air pollution and health. The lancet, 360(9341), 1233-1242.

Dennekamp, M., Howarth, S., Dick, C.A.J., Cherrie, J.W., Donaldson, K. and Seaton, A., 2001. Ultrafine particles and nitrogen oxides generated by gas and electric cooking. Occupational and Environmental Medicine, 58(8), 511-516.

D'sa, A. and Murthy, K.N., 2004. Report on the use of LPG as a domestic cooking fuel option in India. International Energy Initiative, Bangalore, 17-19.

Ezzati, M. and Kammen, D.M., 2002. The health impacts of exposure to indoor air pollution from solid fuels in developing countries: knowledge, gaps, and data needs. Environmental health perspectives, 110(11), 1057.

Ferrari, L., Fleer, F., Pender, T., Tulau, M., Houston, J. and Myszka, A., 2004. Unflued Gas Appliances and Air Quality in Australian Homes. Department of Environment and Heritage.

Ferro, A.R., Kopperud, R.J. and Hildemann, L.M., 2004. Elevated personal exposure to particulate matter from human activities in a residence. J. Exposure Sci. and Environmental Epidemiology, 14(S1), S34.

Franklin, P.J., 2007. Indoor air quality and respiratory health of children. Paediatric respiratory rev., 8(4), 281-286.

Franklin, M., Koutrakis, P. and Schwartz, J., 2008. The role of particle composition on the association between PM2. 5 and mortality. Epidemiology (Cambridge, Mass.), 19(5), 680.

Jurvelin, J., Vartiainen, M., Jantunen, M. and Pasanen, P., 2001. Personal exposure levels and microenvironmental concentrations of formaldehyde and acetaldehyde in the Helsinki metropolitan area, Finland. J. Air and Waste Manag. Assn, 51(1), 17-24.

Kim, K.H., Jahan, S.A. and Kabir, E., 2011. A review of diseases associated with household air pollution due to the use of biomass fuels. J. hazardous materials, 192(2), 425-431.

Koistinen, K.J., Edwards, R.D., Mathys, P., Ruuskanen, J., Künzli, N. and Jantunen, M.J., 2004. Sources of fine particulate matter in personal exposures and residential indoor, residential outdoor and workplace microenvironments in the Helsinki phase of the EXPOLIS study. Scandinavian J. work, environment and health, 36-46.

Kulshrestha, A., Massey, D. D., Masih, J. and Taneja, A., 2014. Source characterization of trace elements in indoor environments at urban, rural and roadside sites in a semi arid region of India. Aerosol Air Qual. Res, 14, 1738-1751.

Lal, H., Punia, T., Ghosh, B., Srivastava, A. and Jain, V.K., 2013. Comparative study of bioaerosol during monsoon and post-monsoon seasons at four sensitive sites in Delhi region. Int. J. Advancement in Earth and Environmental Sci., 1(2), 1-7.

Leung, D.Y., 2015. Outdoor-indoor air pollution in urban environment: challenges and opportunity. Frontiers in Environmental Sci., 2, 69.

Long, C.M., Suh, H.H. and Koutrakis, P., 2000. Characterization of indoor particle sources using continuous mass and size monitors. J. Air and Waste Manag. Assn, 50(7), 1236-1250.

Mishra, V., 2003. Effect of indoor air pollution from biomass combustion on prevalence of asthma in the elderly. Environmental health perspectives, 111(1), 71.

Mishra, S.K., Agnihotri, R., Yadav, P.K., Singh, S., Prasad, M.V.S.N., Praveen, P.S., ...and Sharma, C., 2015. Morphology of atmospheric particles over Semi-Arid region (Jaipur, Rajasthan) of India: Implications for optical properties. Aerosol and air quality research, 15(3), 974-984.

Mishra, M. and Kulshrestha, U., 2017. Chemical characteristics and deposition fluxes of dust-carbon mixed coarse aerosols at three sites of Delhi, NCR. J. Atmos. Chem., 74(4), 399-421.

Nel, A., 2005. Air pollution-related illness: effects of particles. Science, 308(5723), 804-806.

Owen, M.K., Ensor, D.S. and Sparks, L.E., 1992. Airborne particle sizes and sources found in indoor air. Atmospheric Environment. Part A. General Topics, 26(12), 2149-2162.

Pachauri, T., Singla, V., Satsangi, A., Lakhani, A. and Kumari, K.M., 2013. SEM-EDX characterization of individual coarse particles in Agra, India. Aerosol and Air Quality Res., 13(2), 523-536.

Pant, P., Shukla, A., Kohl, S. D., Chow, J. C., Watson, J. G., & Harrison, R. M., 2015. Characterization of ambient PM2. 5 at a pollution hotspot in New Delhi, India and inference of sources. Atmospheric Environment, 109, 178-189.

Pegas, P.N., Nunes, T., Alves, C.A., Silva, J.R., Vieira, S.L.A., Caseiro, A. and Pio, C.A., 2012. Indoor and outdoor characterisation of organic and inorganic compounds in city centre and suburban elementary schools of Aveiro, Portugal. Atmospheric Environment, 55, 80-89.

Pope 3rd, C.A., 2000. Epidemiology of fine particulate air pollution and human health: biologic mechanisms and who's at risk?. Environmental health perspectives, 108(Suppl 4), 713.

Posfai, M., Gelencsér, A., Simonics, R., Arató, K., Li, J., Hobbs, P.V. and Buseck, P.R., 2004. Atmospheric tar balls: Particles from biomass and biofuel burning. J. Geophys. Res.,: Atmospheres, 109(D6).

Quang, T.N., He, C., Morawska, L. and Knibbs, L.D., 2013. Influence of ventilation and filtration on indoor particle concentrations in urban office buildings. Atmospheric environment, 79, 41-52.

Sachdeva, K. and Attri, A.K., 2008. Morphological characterization of carbonaceous aggregates in soot and free fall aerosol samples. Atmospheric Environment, 42(5), 1025-1034.

Salma, I., Dosztály, K., Borsós, T., Söveges, B., Weidinger, T., Kristóf, G., ... and Kertész, Z., 2013. Physical properties, chemical composition, sources, spatial distribution and sinks of indoor aerosol particles in a university lecture hall. Atmospheric environment, 64, 219-228.

Singh, S., Gupta, G.P., Kumar, B. and Kulshrestha, U.C., 2014. Comparative study of indoor air pollution using traditional and improved cooking stoves in rural households of Northern India. Energy for sustainable development, 19, 1-6.

Spengler, J.D. and Sexton, K., 1983. Indoor air pollution: a public health perspective. Science, 221(4605), 9-17.

Srivastava, A. and Jain, V.K., 2003. Relationships between indoor and outdoor air quality in Delhi. Indoor and Built Environment, 12(3), 159-165.

Srivastava, A. and Jain, V.K., 2007. A study to characterize the suspended particulate matter in an indoor environment in Delhi, India. Building and environment, 42(5), 2046-2052.

Tumolva, L., Park, J.Y., Kim, J.S., Miller, A.L., Chow, J.C., Watson, J.G. and Park, K., 2010. Morphological and elemental classification of freshly emitted soot particles and atmospheric ultrafine particles using the TEM/EDS. Aerosol Sci. and Technology, 44(3), 202-215.

Viswanadham, D.V. and Santosh, K.R., 1989. Air pollution potential over south India. Boundary-Layer Meteorology, 48(3), 299-313.

Wiedinmyer, C., Yokelson, R.J. and Gullett, B.K., 2014. Global emissions of trace gases, particulate matter, and hazardous air pollutants from open burning of domestic waste. Environmental Sci. Technology, 48(16), 9523-9530.

World Health Organization., 2002. The world health report 2002: reducing risks, promoting healthy life. World Health Organization.

Received on: 27.1.19; Revised on: 13.3.19; Accepted on: 18.3.19

J. Ind. Geophys. Union (May 2019)
v.23, no.3, pp: 271-278

Tree ring-width study from North Sikkim region of India in relation to heat and moisture index: A case study

Somaru Ram[1]*, Ramesh Kumar Yadav[1], H.N. Singh[1], and Manoj K. Srivastava[2]

[1] Indian Institute of Tropical Meteorology, Pune-411008, India
[2] Department of Geophysics, Banaras Hindu University, Varanasi-221005, India
*Corresponding author: somaru@tropmet.res.in

ABSTRACT

A tree-ring data of *Tsuga Dumosa* of 438 years (1572-2009 C.E.) from the north Sikkim region of India, have been used in relation to climate variability / change over the region. The tree growth climate-relationship indicates that late summer (July to August) heat index and temperature over the region, have significant negative impact on tree growth while moisture index (which is a function of rainfall and temperature) exhibits a positive relationship with tree growth during late spring (April to May). Heat index and mean temperature showed constantly significant correlation coefficients (at the 5% level) from 1981 onwards in sliding 31-year window, suggesting that the late summer heat index might be the important climatic parameters influencing the tree growth patterns over the region. However, there is a variation in the relationship over time. The results indicate that the rising heat index /temperature during late summer might enhance the moisture deficiency over the region by accelerating potential evapotranspiration, which is not found to be conducive for tree growth.

Keywords: Eastern Himalaya, tree ring chronologies, Temperature, Moisture index, Heat index

INTRODUCTION

The climate change study has been one of the hot topics in many parts of the world. Particularly the Himalaya, which includes the highest mountain ranges on the earth, had the largest interaction with tropical, subtropical, polar, and Mediterranean influences over the Asian region. The northern part of India especially hilly region and adjoining plains are influenced by transient disturbance in mid latitude westerlies (De et al., 2005). Vast diversity in climate within a short distance can be seen due to distinct changes in mountain ranges across the Himalayas, especially rainfall.

In contrast, there is a strong consistency in temperature variations over the Himalaya ((Yadav, 2009; Yadav et al., 2004; Yadav and Singh, 2002). Such climatic records are available from the western Himalaya tree growth of different species. Despite these, there is a fairly good amount of tree ring based climate reconstruction of the western Himalayan region (Cook et al., 2010; Hughes, 1992; Yadav et al., 1997, 2015a; Singh and Yadav, 2005; Singh et al., 2009, 2006; Ram, 2012; Ram and Borgaonkar, 2016, 2017), which indicates the possibilities of getting suitable trees for the reconstruction of rainfall and temperatures from this region.

However, tree-ring based studies from the Eastern Himalaya are sparse, but it is extremely important to understand climatic conditions over this monsoon dominated region. The incoming monsoon wind originating over the Bay-of-Bengal, which is very close to Eastern Himalaya, causes more precipitation in the region than central and western part of the Himalaya (Shah et al., 2014a). The changes in precipitation / temperatures over the region of the eastern Himalaya may affect a large area and population of the Indian sub-continent and south-east Asia, who inhabited over mountain chains and depended on the natural resources of the region (Shah et al., 2014a).

Moreover, to understand the long-term temperature, rainfall, and discharge fluctuations over the Eastern Himalaya, some of dendroclimatic analysis over the region has been performed in relation to natural climate variability / change using different species like Fir, Toona ciliata, and Tsuga dumosa (Bhattacharyya et al., 1992; Shah and Mehrotra, 2017; Shekhar and Bhattacharyya, 2015; Borgaonkar et al., 2018). These studies showed that the relationship of tree growth with rainfall and temperature over the region, emphasizes the potential of tree growth to reconstruct the past climate for a few centuries. However, in the present analysis, due to lack of proxy climate records over the eastern Himalaya, we attempt here to assess the connection between trees growth and climate (moisture index, heat index, rainfall and temperatures) nearby and thereby to understand the climate factors which is more dominated in limiting tree growth patterns than rainfall and temperature over the region.

METHODOLOGY

Tree ring-width data

Tree ring-width data of *Tsuga dumosa* from eastern Himalaya has been used in relation to climate variability over the region. We considered total 36 tree cores samples from 24 trees from Dambung site in north Sikkim region of eastern Himalaya (Borgaonkar et al., 2018) to investigate tree growth climate relationship (Figure 1). The quality

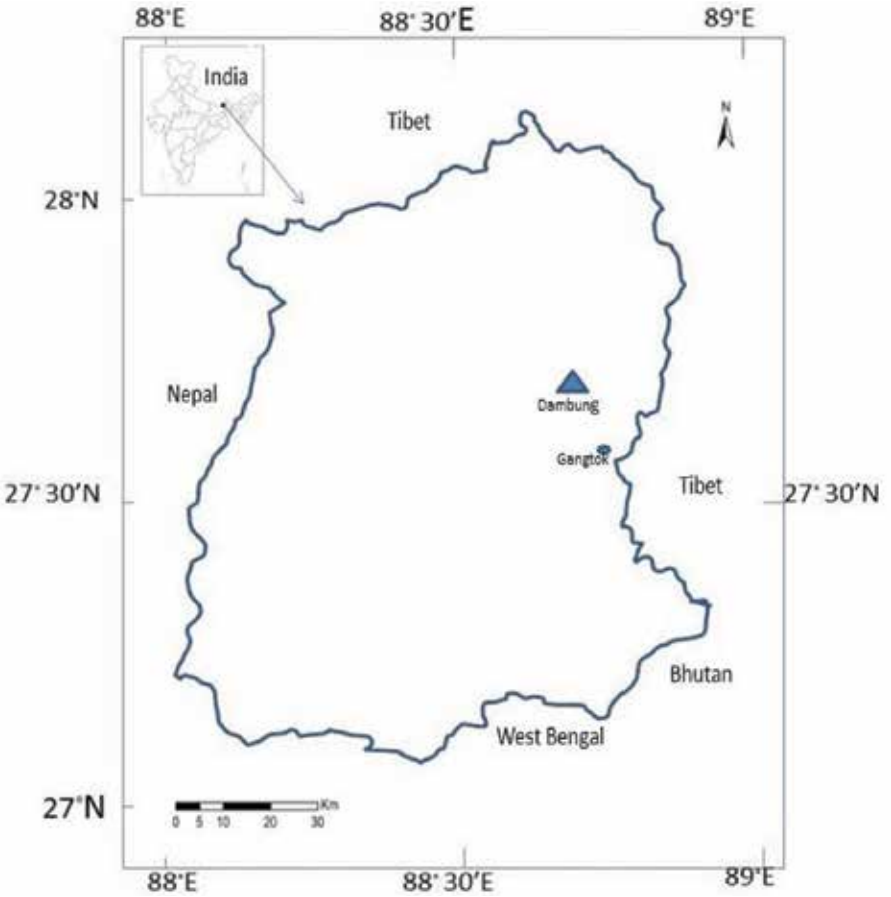

Figure 1. Location of the study areas in Sikkim. ▲: tree ring site; ●: climatic data

of cross dating tree ring-width data were further checked using the COFECHA program (Holmes, 1983) to identify possible dating and measurement problem in the samples, if any. The inter-correlation coefficient of all radii computed by COFECHA is 0.526, which indicates coherency in tree growth variations and representing the common signal in tree ring-width data, i.e. climate.

Dated ring-width series were then standardized using the program ARSTAN (Cook, 1985) to remove the growth trends of stand dynamics and preserve the common variations (Cook, 1985; Cook and Kairiukstis, 1990). A 35-year smoothing spline with 50% frequency cut off response was used for detrending of tree core samples to obtain a new index for each tree core sample. A new tree ring-width index was prepared for each sample by dividing the actual ring width (raw ring width) through corresponding year curve fitted values (Borgaonkar et al., 2018). Each ring-width index series was pre-whitened by autoregressive model to reduce the persistence of low frequency signal from the indices. The resulting indices were then averaged robustly to dimensionless chronologies of ring width indices. Statistics of tree ring chronology is shown in a Table 1 and time series of the standard chronology, which has been used in further analysis, is shown in Figure 2.

Climatic Data

Climatic records from the north Sikkim are very patchy and sparse. Meteorological stations over the region are mainly localized in the valley floor, which may not present the proper climate of the sampling sites located at remote and high altitude in the Himalayan region. However, to establish the relationship between tree growth and climate a long climatic record is required from nearby. In this context, the Gangtok meteorological station has been selected which is considered the nearest to the study site as compared to other stations. The observed data is more reliable than gridded data in tree growth-climate relationship (Figure 1). The time span of climatic (rainfall, mean, maximum and minimum temperature) data is from 1966 to 2017 C.E. However, there were some missing data in climate records. They are mostly in 2008 and 2011. The missing data in climate records (rainfall and temperatures) were estimated using the Dendrochronology program library (DPL). In addition, monthly moisture (which is a function of rainfall and temperature) and heat index were computed using the empirical formula developed by Thornthwaite (1948) and Ram et al. (2008), in relation to assess the relationship between tree growth and climate.

Table 1. General statistics of tree ring chronology from North Sikkim of Eastern Himalaya (the values inside the bracket are with autoregressive modeling).

Chronology time span	1572-2009 C.E.
Numbers of tree (radii)	24 (36)
Mean sensitivity	0.18 (0.20)
Standard deviation	0.19 (0.16)
Autocorrelation order 1	0.36 (0.0)
Common interval time span	1867-1997
Number of trees (radii)	20 (25)
Common variance	0.24 (0.30)
Signal to Noise Ratio (SNR)	6.4 (8.3)
Expressed population signal (EPS)	0.96 (0.98)

Table 2. Monthly trends/years in rainfall (RF) and mean temperature (Tm) of Gangtok,

	Jan	Feb	Mar	Apr	May	Jun	Jul	Aug	Sep	Oct	Nov	Dec
RF	-0.41	-.02	-.10	2.5*	-2.7	0.67	-0.95	-0.69	-1.4	-0.42	.01	-0.21
Tm	.01	.02	0.0	0.0	.01	.01**	0.0	.01*	0.0	0.0	0.0	.02

*significant at 5% level; **significant at1% level;

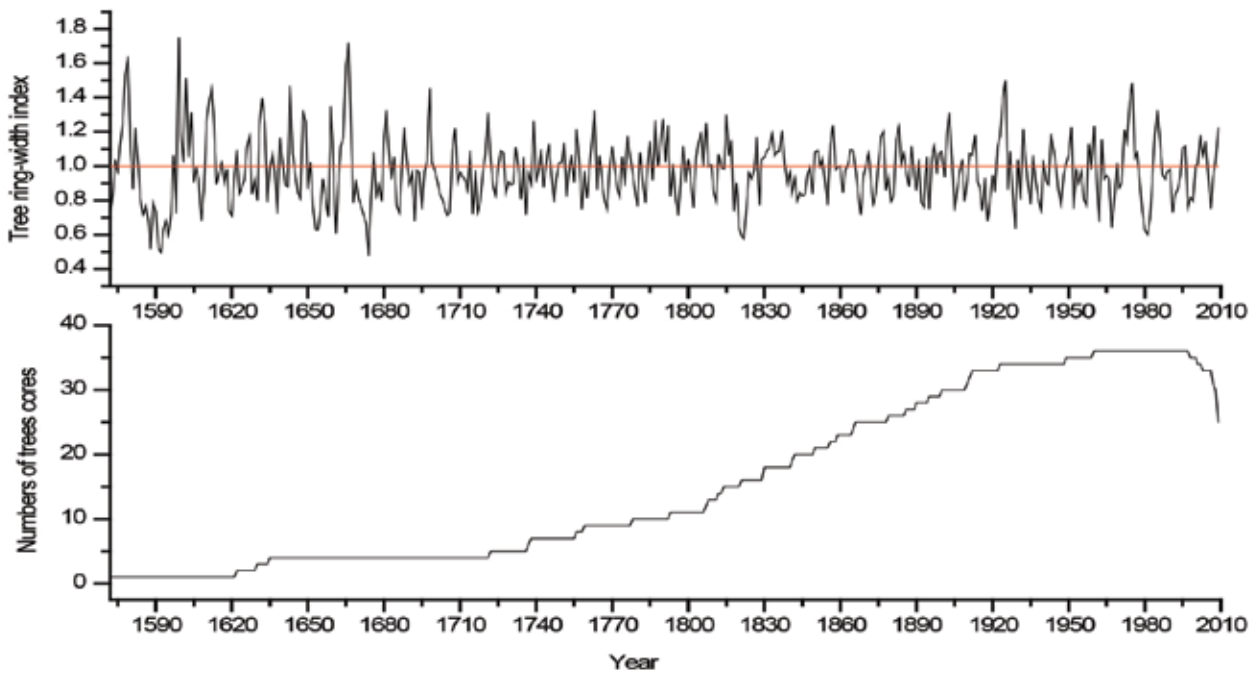

Figure 2. Tree ring-width index chronology from eastern Himalaya during 1572-2009 C.E.

Mean monthly variations of mean, maximum and minimum temperature and rainfall were shown in Figure 3. The highest mean rainfall (633.9 mm) was observed in the month of July. More than 70% of the annual rainfall over the region is brought by the monsoon season (Figure 3). August is the hottest month by 19.6°C and January coldest by 8.7°C. June and August month temperatures showed significant increasing trends over the region. In case of rainfall, the only significant increasing trend was found in the month of April, representing the general climatic condition in and around the sampling areas (Table 2).

Tree growth-climate relationship

To examine relationship between tree growth and climate we have carried out the Correlation analysis by using

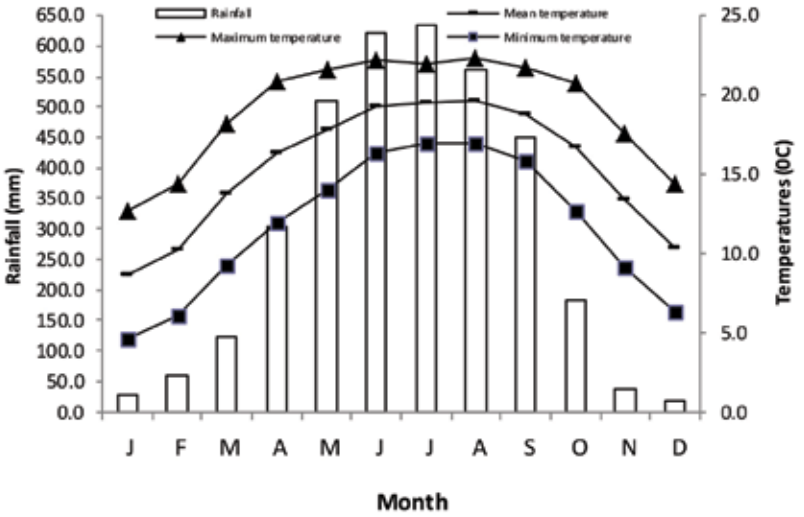

Figure 3. Mean monthly variations in rainfall (bar), mean (-), maximum (▲) and minimum temperatures (▪) at Gangtok during 1966-2017.

program DENDROCLIM2002 (Biondi and Waikul, 2004) to understand the influence of climate on tree growth (Figure 4a-f).The monthly climatic data for a 13 month period extending from previous year's October (ending growth) to current year's October (ceasing tree growth) were used for trees growth-climate relationship, covering time span from 1966-2009C.E. The climate data of the previous growth year were considered in the analysis to understand the influence of previous year climate on tree growth. Horizontal dashed lines are the significant level at 5% (Figure 4a-f). Correlation analysis shows that tree growth is significantly negatively correlated with current year July to September mean and maximum temperature and heat index and positively correlated with April and May moisture index (Figure 4a-f). Minimum temperature during July-September also show negative correlation with trees growth, but not statistically significant. However, rainfall data does not indicate significant relationship with tree growth.

RESULTS AND DISCUSSION

Tree ring chronology was developed from the dated tree ring-width data as mentioned in Table 1. The statistical performance of tree ring chronology is also shown in table 1. The values inside the brackets are from the autoregressive modeling. The statistics indicated high dendroclimatic potential of the chronology prepared from the species of *Tsuga dumosa*. The statistical parameters namely signal to noise ratio, common variance, expressed population signal (EPS), and mean sensitivity of the chronology are 8.3, 0.30, 0.98, and 0.20 respectively, increased slightly after autoregressive model (Table 1). Moderately high common variance (between trees), signal to noise ratio (depend on numbers of trees and mean correlation) indicated the usefulness of tree ring chronologies for dendroclimatic analysis (Fritts, 1976). The EPS value of 0.85 was taken as reasonable threshold used to assess the acceptance of tree ring-width chronology quality, which quantifies the degree to which the prepared chronology is found hypothetically perfect and reliable for further analysis (Wigley et al., 1984; Fritts, 1976).

Correlation analysis indicated that tree growth over the region was mainly affected by mean and maximum temperatures, and heat index of late summer (July to September) and moisture index of late spring (April to May). The negative correlation of tree growth with minimum temperature of July-September was also observed, but not significant. However, significant positive relationship of tree growth with moisture index during April indicates that tree growth over the region is moisture sensitive. May moisture also reveals positive relationship, but barely significant. There is no significant relationship between tree growth and rainfall of any month.

However, the significant relationship of tree growth with moisture during April indicates that increasing trend in April rainfall, might maintain sufficient moisture at root zone of the trees (Table 2), and boosts moisture to trees growth for early wood formation during growing season. So, based on the close relationship between tree growth and moisture, we formed a season to see the combine effect of moisture during late spring (April to May) (Figure 5). The CCs between tree growth and late spring (April to May) is observed 0.34 (significant at 5% level), indicates seasonally climate is more effective than a single month. Both the time series showed the similar type of variations during common period 1966-2009 (Figure 5). It means that wet and cool condition during spring season, might be in favour of trees growth over the studied region (Shah et al. 2014b; Singh and Yadav, 2005; Singh et al., 2009; Shekhar and Bhattacharyya, 2015; Ram and Borgaonkar, 2014).

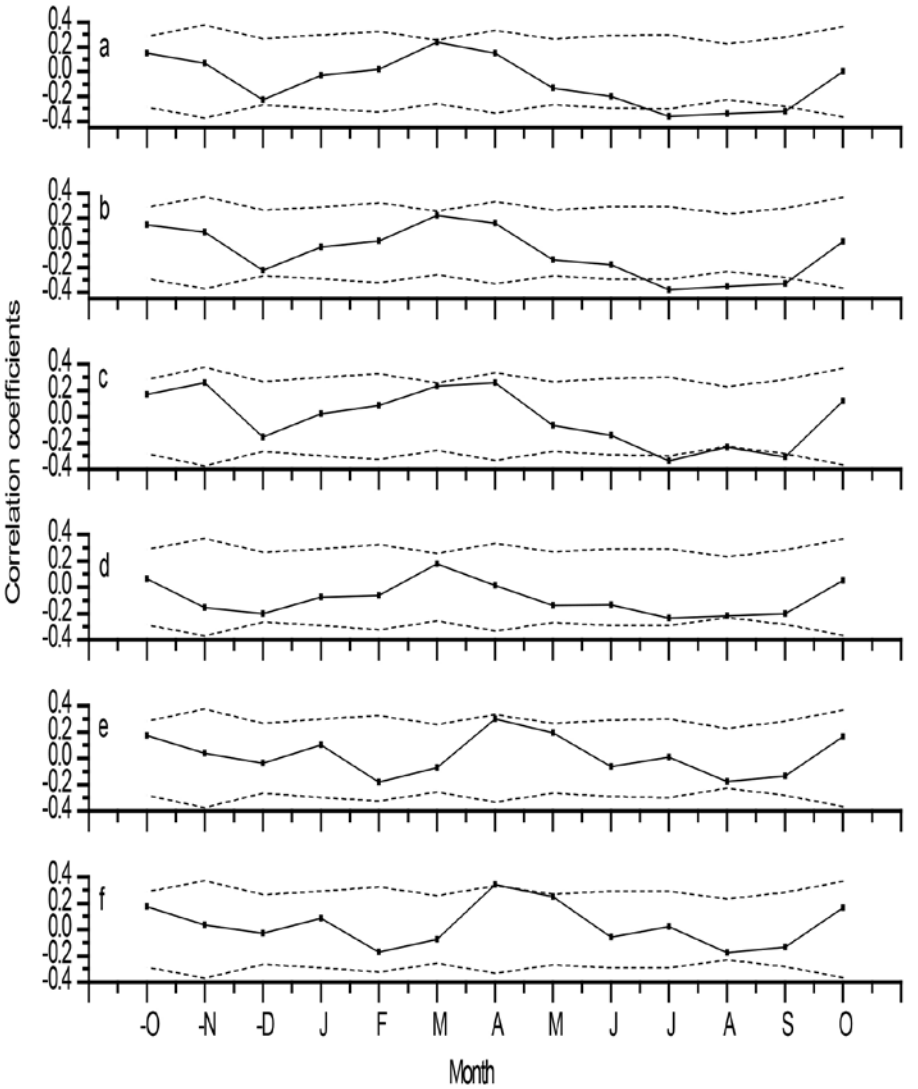

Figure 4. Correlation coefficients between tree ring-width index chronology and mean temperature (a), heat index (b), maximum temperature (c), minimum temperature (d), rainfall (e), and moisture index (f) during 1966-2009. Dashed line indicates significant at 5% level.

Similarly, to see the relationship between tree growth and monthly heat index, mean, maximum and minimum temperatures during consecutive three month (July to September), we have made a season from July to September to see the impact of seasonal climate on tree growth over the region. The Correlation coefficients (CCs) between tree ring-width index chronology and mean temperature, heat index, maximum and minimum temperatures are -0.36, -0.38, -0.34, and -0.23 respectively (Figure 6a-d). CCs are found statistically significant at 5%, 1%, 5% level respectively, except minimum temperature. It showed that seasonally averaged climate is more dominant than a single month climate in development of trees growth over the eastern Himalayan region (Shekhar and Bhattacharyya, 2015; Singh and Yadav, 2005; Ram and Borgaonkar, 2014, 2016, 2017; Ram, 2018).

The observed CCs are slightly more between tree growth and seasonal heat index than CCs between tree growth and other climate (Figure 6a-d). It showed that heat index's influence is more on tree growth patterns than other climate of the region. Thus, increasing heat index, mean, maximum and minimum temperatures during late summer, might enhance the moisture deficiency over the region due to high potential evapotranspiration, which is not found to be conducive in favor of trees growth (Ram and Borgaonkar, 2016).

Moreover, to see the long-term temporal stability between tree growth and climate (heat index, mean and maximum temperatures), we have performed a 31-year sliding correlation analysis, based on their significant relationship. Heat index and mean temperature showed constantly significant correlation coefficient from 1981

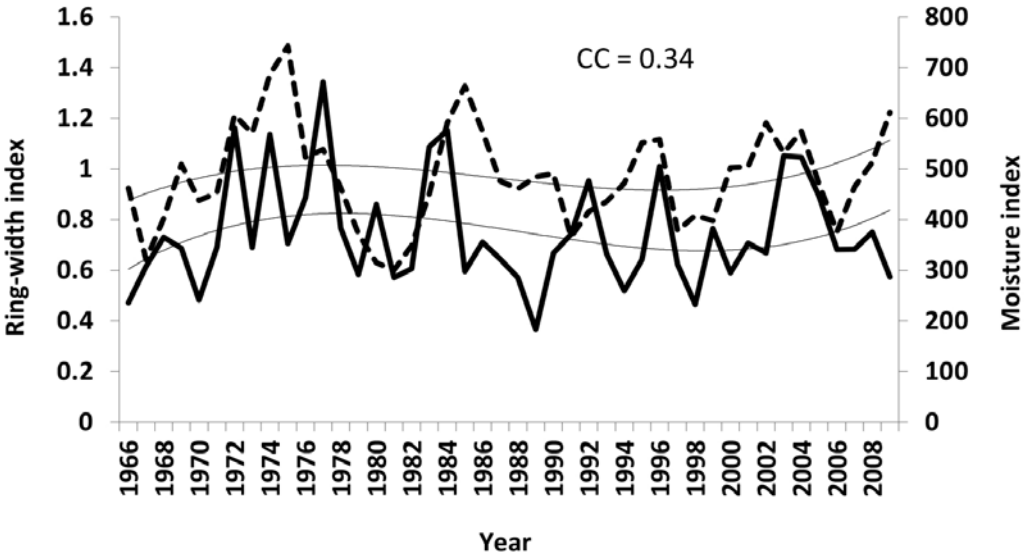

Figure 5. Variation in tree ring-width index chronology (dashed lines) and moisture index (solid lines) during late spring (April to May) during 1966-2009. The smoothed lines are 3rd degree polynomial fitting. CC is correlation coefficient.

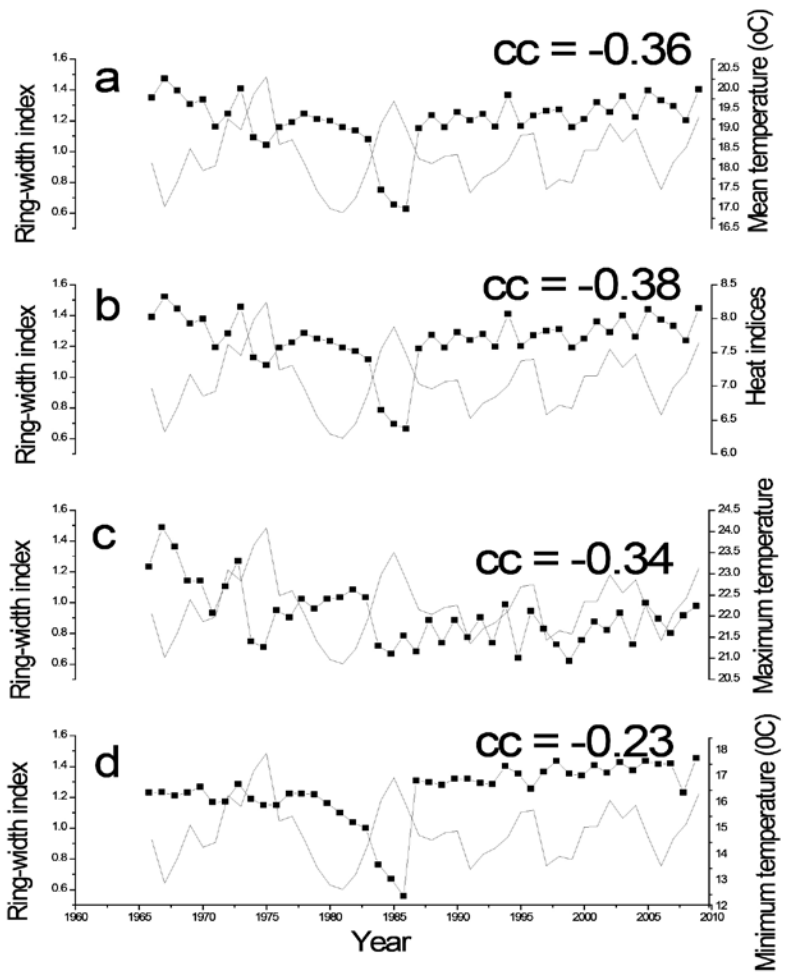

Figure 6. Variations in tree ring-width index (solid line) with (a)mean temperature (▄), (b) heat indices (▄), (c) maximum temperature (▄), and (d) minimum temperature(▄) during common period 1966-2009.CC is the correlation coefficients.

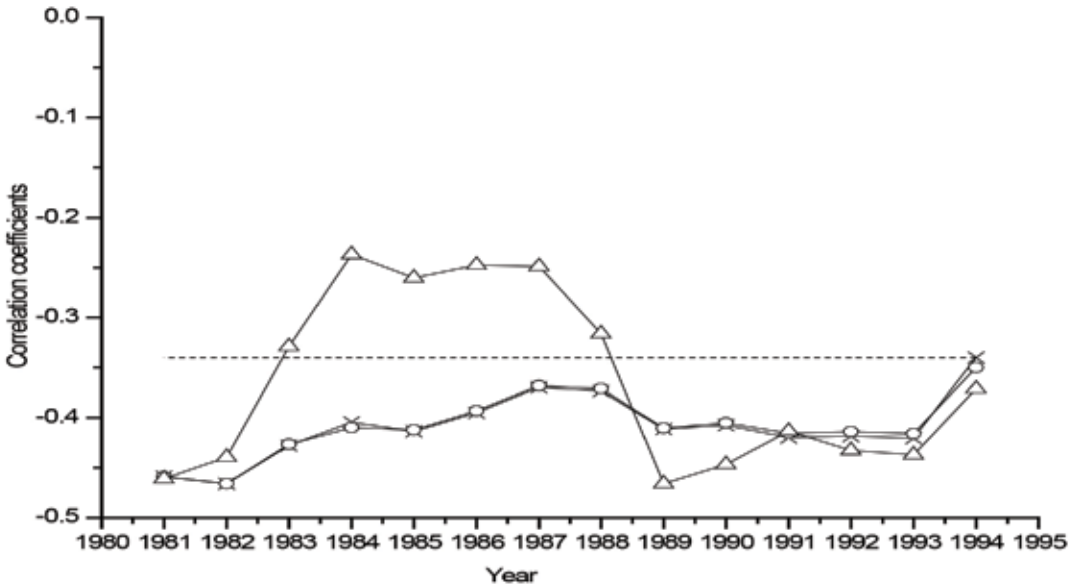

Figure 7. The sliding 31-year correlation coefficients between tree ring-width index chronology and mean temperature (x), heat index (o) and maximum temperature (Δ) during summer (July to September). Correlation coefficients are plotted against the central year of 31-year period. Dashed lines are 95% confidence level.

onwards. There is a variation in the relationship over time. However, the maximum temperatures showed significant CCs during 1981-1982, and 1989 onwards (Figure. 7).

There are weaken CCs during 1984-1988.The reason for weakening CC is not known but increasing heat index / temperature over the region might be one of the possible causes to change the behavior of the trees.

Overall, the results indicate that increasing heat index and mean temperature during summer (July to September) over the region, has adverse effect on trees growth by creating high potential evapotranspiration, which results insufficient moisture supply over the region, which is not considered favourable for the growth of the trees during following and subsequent year growing season of the trees (Borgaonkar et al., 2018; Yadav et al., 2015b). Whereas, wet and cool condition during late spring (April to May), exhibit an important role in tree growth over the region. The study showed that long-term high resolution proxy record of tree rings from this region, might be very useful in understanding the long-term fluctuation of moisture and heat indices in absence of observed climate data.

CONCLUSIONS

The relationship of tree growth with various climatic parameters indicates that tree growth in this area is very sensitive to heat index and temperatures during summer climate of July to September and moisture availability during the late spring season (April to May). This single site tree ring–width data motivate us to develop a tree ring chronology by incorporating the higher replication of tree core samples from the Himalayan region for the earlier period to monitor the wet and dry conditions over the region. Tree ring studies carried out in this region may be benefited in planning of management of the resources and environment conservation. The environment where weather stations are not available can be known from the tree growth patterns and climate reconstruction studies. And thereby, establishing the relationship between tree growth and climate over the region may fill up the gap of discrepancy in understanding climate variability / change on local and regional scale across the Himalaya, other than rainfall and temperature. Moreover, heat and moisture index data from this region would be of great use for forest management, water resources, and agricultural point of view.

ACKNOWLEDGEMENTS

Authors show gratitude to Director, IITM, Pune and Dr. R. Krishnan, Executive Director, CCCR, IITM, Pune for their kind support and providing infrastructure facilities. The authors are thankful to forest department of Sikkim for their kind help during field work and Dr. H.P. Borgaonkar (visiting scientist), IITM for his kind help in data preparation. Authors are grateful to India meteorological Department (IMD), Pune for providing the climatic data.

Compliance with Ethical Standards

The authors declare that they have no conflict of interest and adhere to copyright norms.

REFERENCES

Biondi, F. and Waikul, K., 2004. Dendroclim2002: AC++ program for statistical calibration of climate signals in tree-ring chronologies. Comput. Geosci., 30, 303-311.

Borgaonkar, H.P., Gandhi, N., Ram, S. and Krishnan, R., 2018. Tree ring reconstruction of late summer temperatures in northern Sikkim (eastern Himalaya). Palaeogeo. Palaeoclimatol. Palaeoecolog., 504, 125-135.

Bhattacharyya, A., Lamarche, Jr., V.C. and Hughes, M.K., 1992. Tree-ring chronologies from Nepal. Tree ring Bull. 52, 59-66.

Cook, E.R. and Kairiukstis, L.A., 1990. Methods of dendrochronology: applications in the environmental sciences. Kluwer Academic Publ., Dordrecht/Boston/London. p.394

Cook, E.R., Anchukaitis, K.J., Buckley, B.M., D'Arrigo, R.D., Jacoby, G.C. and Wright, W.E., 2010. Asian Monsoon failure and megadrought during the last millennium. Science, 328, 486-489.

Cook, E.R., 1985. A time series analysis approach to tree-ring standardization; Dissertation, University of Arizona, Tuscon, AR, USA.

De, U.S., Dube, R.K. and Prakasa Rao, G.S., 2005. Extreme weather events over India in the last 100 Years. J. Ind. Geophy. Uni., 9(3), 173-187.

Fritts, H.C., 1976. Tree-rings and climate; Academic press, London.

Holmes, R.L., 1983. Computer assisted quality control in tree-ring dating and measurement. Tree-ring Bull., 44 69-75.

Hughes, M.K., 1992. Dendroclimatic evidence from the western Himalaya. In: R.S. Bradley and P.D. Jones, editors, Climate since AD1500, London: Routledge

Ram, S., 2012. Tree growth-climate relationships of conifer trees and reconstruction of summer Palmer Drought Severity Index at Pahalgam in Srinagar, India. Quat. Int. 254, 152-158.

Ram, S. and Borgaonkar, H.P., 2014. Tree-ring analysis over the western Himalaya and its long-term association with vapor pressure and potential evapotranspiration. Dendrochronologia, 32, 32-38.

Ram, S. and Borgaonkar, H P., 2016. Reconstruction of heat index based on tree-ring width records of western Himalaya in India. Dendrochronologia, 40, 64-71.

Ram, S. and Borgaonkar, H.P., 2017. Moisture index during the last two centuries inferred from tree growth in the western Himalaya. Curr. Sci., 112, 12: 2453-2455.

Ram, S., Borgaonkar, H.P. and Sikder, A.B., 2008. Tree-ring analysis of teak (*Tectona grandis* L.F.) in Central India and its relationship with rainfall and moisture index. J. Earth Sys. Sci., 117(5), 637-645.

Ram, S., 2018. Tree ring-width variation over western Himalaya in India and its linkage with heat and aridity indices. Nat. Haz., 92, 635-645.

Shah, S.K., Mehrotra, N. and Bhattarchayya, A., 2014a. Tree-ring studies from Eastern Himalaya: Prospects and challenges. Him. Res. J., II(I), 21-28.

Shah, S.K., Bhattarchayya, A, and Chaudhary, V., 2014b. Streamflow reconstruction of Eastern Himalaya river, Lachen 'Chhu' north Sikkim, based on tree-ring data of larix griffithiana from Zemu glacier basin. Dendrochronologia, 32, 97-106.

Shah, S.K. and Mehrotra, N., 2017. Tree-ring studies of Toona ciliata from subtropical wet hill forest of Kalimpong, Eastern Himalaya. Dendrochronologia, 46, 46-55.

Shekhar, M. and Bhattacharyya, A., 2015. Reconstruction of January-April discharge of Zemu Chuu-A first stage of Teesta river north Sikkim eastern Himalaya based on tree ring data of Fir. J. Hydro.: Regional studies 4, 776-786.

Singh, J. and Yadav, R.R., 2005. Spring precipitation variations over the western Himalaya, India, since A.D. 1731 as deduced from tree-rings. J. Geophy. Res., 110, d01110, doi: 10.1029/2004JD004855

Singh, J., Park, W.K. andYadav, R.R., 2006.Tree-ring based hydrological records from Western Himalaya, India. Clim. Dyn., 26, 295-303.

Singh, J., Yadav, R.R. and Wilmking, M., 2009. A 694-year tree-ring based rainfall reconstruction from Himachal Pradesh, India. Clim. Dyn., Doi 10:1007/s00382-09-0528-5

Thornthwaite, C.W., 1948. An approach towards a rational classification of climate. Geograph. Rev., 38, 55-94.

Wigley, T.M.L., Briffa, K.R. and Jones, P.D., 1984. On the average value of correlated time series, with applications in dendroclimatology and hydrometeorology. J. Clim. Appl. Meteorol., 23, 201-213.

Yadav, R.R., Park, W.K., Singh, J. and Dubey, B., 2004. Do the western Himalayas defy global warming? Geophy. Res. Lett., 31, L17201.doi:10.1029/2004GL020201.

Yadav, R.R., 2009.Tree Ring imprints of long-term climate changes in climate in western Himalaya, India. J. Bios., 34(5), 699-707.

Yadav, R.R., Park, W.K. and Bhattacharyya, A., 1997. Dendroclimatic reconstruction of April-May temperature fluctuations in the western Himalaya of The India since A.D.1698. Quat. Res., 48, 187-191.

Yadav, R.R. and Singh, J., 2002. Tree-Ring based spring season temperature patterns over the past four centuries in western Himalaya. Quat. Res., 57, 299-305.

Yadav, R.R., Misra, K.G., Yadav, A.K., Kotlia, B.S. and Misra, S., 2015a. Tree-ring footprint of drought variability in last 300 years over Kumaun Himalaya, India and its association with crop productivity. Quat. Sci. Rev., 117, 113-123.

Yadav, A.K., Yadav, R.R., Misra, K.G., Singh, J. and Singh, D., 2015b. Tree ring evidence of late summer warming in Sikkim, northeast India. Quat. Int. 371, 175-180.

Received on: 20.2.19; Revised on: 5.4.19; Accepted on: 14.4.19

J. Ind. Geophys. Union (May 2019)
v.23, no.3, pp: 279-284

A comparative geochemical study on laterites from Mallampalli of Pakhal Sub Basin (Telangana) and eastern parts of Andhra Pradesh, Southern India

N. Kalpana[1]*, A. Narsinga Rao[1], and K.S.V. Subramanyam[2]

[1]Department of Geology, Osmania University, Hyderabad-500007, India
[2]CSIR- National Geophysical Research Institute, Hyderabad-500007, India
*Corresponding author: kalpananerella52@gmail.com

ABSTRACT

This paper focuses on geochemical variations and genesis of laterites from different parts of Andhra Pradesh (AP) and Mallampalli region of the Telangana state. Geochemically, the AP laterites are rich in Al_2O_3 content and depleted in Fe_2O_3, but Mallamapalli laterites are found to be enriched in Fe_2O_3 content and depleted in Al_2O_3. The non-lateritic nature is recorded in the studied samples at few places of AP. The chemical index alteration and chemical index weathering values of the laterites from Mallampalli and AP are almost similar. Based on geochemical studies the Mallampalli laterite can be considered altered product of ferruginous shale (bed rock), which was subjected to kaolinization, while the AP laterites can be considered alteration products of mafic protolith.

Key words: Pranahita Godavari Basin, Proterozoic Pakhal Group, Laterite, Ferruginous shale.

INTRODUCTION

In Indian geological scenario, the laterites occupied a vital place and the word "laterite" was introduced by Buchanan (1807), which denote a building material used in the mountaineous regions of Malabar (India). It occurs in an area of about 2,48,000 km^2 in the states of Karnataka, Kerala, Madhya Pradesh, the Eastern Ghat regions of Orissa, Maharashtra, Malabar and parts of Assam (Raychaudhuri, 1980). In Andhra Pradesh (AP), the laterite and lateritic soils occur in the districts of Srikakulam, Visakhapatnam, East Godavari and Nellore, but in Telangana state, the deposits are restricted to Medak, Jayashankar bhupalpalli and Warangal districts. Major laterite soils cover an area of 82,869 hectares in the Medak district and occupy 61,793 ha in Zaheerabad and Sadasivapet areas (Reddy et al., 2005).

The present paper focuses on laterites of Mallampalli area from Mallampalli subgroup belonging to Mid-Proterozoic Pakhal group of Pranhita–Godavari (PG) Valley. Quantitative characterization of weathering in laterite, is done by developing weathering indices (Price and Velbel, 2003), The Chemical Index of Alteration (CIA) (Nesbitt and Young, 1982) and Chemical Index of Weathering (CIW) (Harnois and Moore, 1988). The Pranhita–Godavari (PG) Valley is oriented NW–SE and cover parts of Telangana, Maharashtra and the Bastar region of Chhattisgarh. PG valley is surrounded by the Dharwar and Bastar cratons on either side (Naqvi and Rogers 1987). It is about 400 km in length and about 100 km in width (including the Gondwana outcrops in the middle), and is in tectonic contact with a linear belt of granulites on both sides (Chaudhuri et al., 2002). The PG Basin can be divided into two sub-parallel belts i.e., eastern and western belts, with the contact zone between the two belts covered by an about 40 km wide outcrop of Paleozoic–Mesozoic rocks of the Gondwana Supergroup (Conrad et al., 2011). Paleogeographical reconstructions suggest that during Pakhal times, the PG Basin was a continental margin marine basin that opened to the east in Eastern Ghats belt (Chaudhuri, 2003).

STUDY AREA

Our study area falls between latitudes 17°59´ to 18°11´N and longitudes 79°45´ to 80°01´E and belong to the Godavari rift valley formation. The reddish brown colored laterite deposits occur as capping on dolomite limestones at Ramachandrapuram as well as Mallampalli villages of Mulug taluk, extending to a maximum thickness of 10 to 15 meters and well exposed towards the eastern side of Mallampalli with boulder to nodular appearance (Figure 1).

GEOLOGICAL SETTINGS

The Pakhal Group (eastern belt), comprises Mallampalli and Mulug Sub groups having an overall sequence of coastal alluvial to shallow marine conglomerates and arkosic to sub arkosic sandstones, grading into limestones and dolomites, deposited in coastal marine environments, such as tidal flats, lagoons and intertidal and high-energy banks (Chaudhuri and Howard, 1985). The Mallampalli Group (Lower Pakhals) sediments are deposited around 1686±6 Ma and the Mulug Group (Upper Pakhals) sediments, around 1565 ± 6 Ma in the Pakhal basin, which is further overlain by Penganga Group, deposited around 1180 Ma (Conard, et al., 2011) (Figure 2).

Figure 1. (a) Gritty, layered, medium to coarse hematite nodule horizons. (b) Exposures of coarse hematite nodules

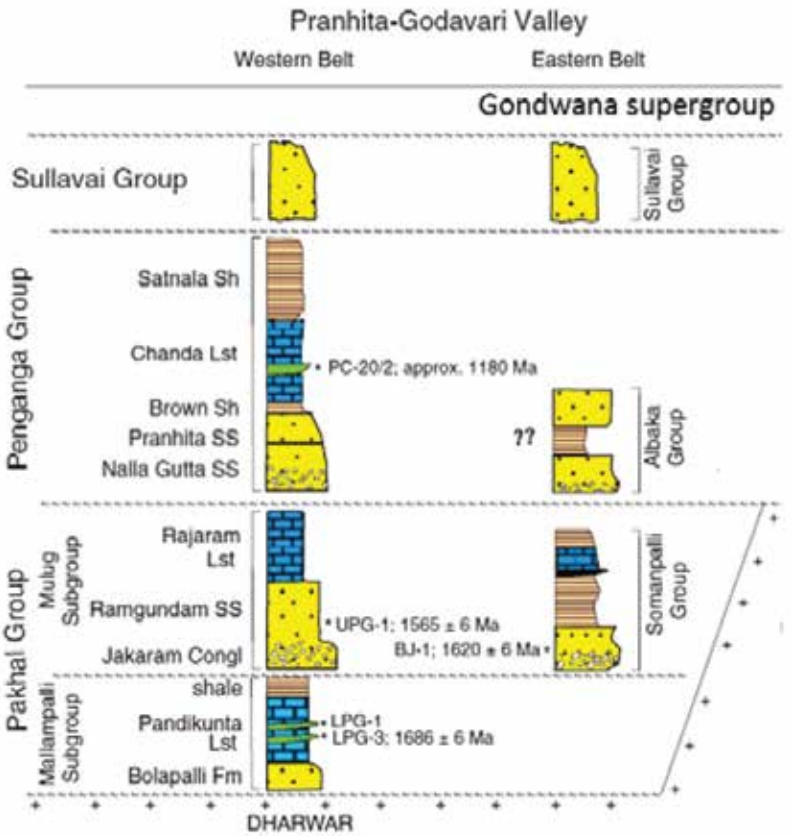

Figure 2. Geological cross section depicting stratigraphic succession of Pranahita-Godavari valley (Conrad et al., 2011). Geological ages are from Patranabis-Deb and Chaudhuri, 2007) and Das et al., (2009).

The Mallampalli laterite formation has a sharp contact on its northeastern side with sandstone of Mulug formation and on southwestern side with grey granites of eastern Dharwar craton. It is understood that the Dharwar craton of south India is made up of two sub-blocks. The older western Dharwar craton (WDC: 3.3–2.7 Ga), which is mainly composed of a tonalite–trondhjemite–granodiorite (TTG) gneissic basement, overlain by greenstone belts, while the younger eastern Dharwar craton (EDC: 3.0–2.5 Ga), comprises Neoarchaean (2.6–2.5 Ga) granitic intrusive into older TTG gneisses (2.9–2.7 Ga; Chadwick et al., 2000; Figure 3).

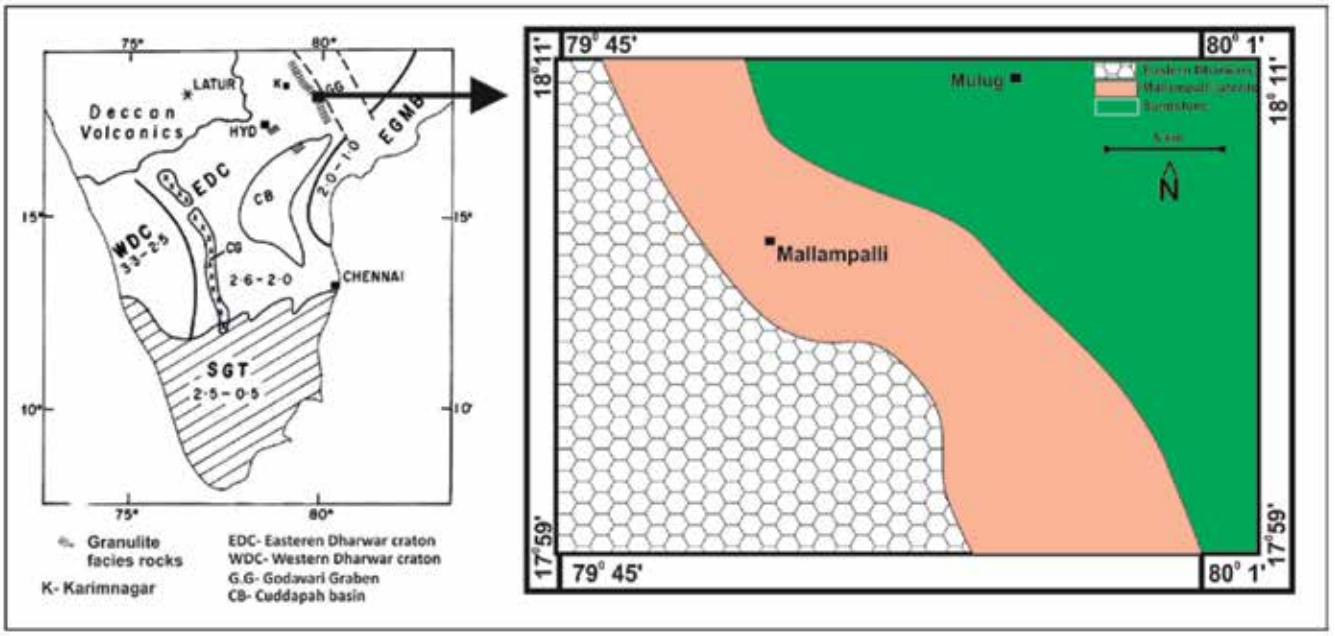

Figure 3. The Geological map of the Mallampalli area, Jayashankar Bhupalpalli district, Telangana

GEOCHEMISTRY

The Mallampalli laterite is found to be highly enriched in Fe_2O_3 content (22.1 to 25.2 wt. %). In comparison, the AP laterites of (i) Allimadugu contain on an average 10.2 (wt.%) (ii) Venkateswarapalem 11.9 (wt. %) (iii) Venkatachalam 13.4 (wt.%), (iv) Saidapuram 13.2 wt.%, (v) Kadivedu 12.5 wt.% and (vi) Nellore 12.4 wt.%. Similarly, the Al_2O_3 content in (i) Mallampalli laterites varies from 13.2 -13.3 wt.%, (ii) Allimadugu 14.1 wt.%, (iii) Venkateswarapalem 16.7 wt.%, (iv) the Venkatachalam 22.3 wt.%, (v) Saidapuram 18.3 wt.%, (vi) Kadivedu 19.4 wt.% and (vii) Nellore 15.3 wt.%. Among these laterites, the Mallampalli laterites are similar to Allimadugu laterites. Besides, the AP laterites have considerably high SiO_2 percentage (60.1-73.7 wt. %) in comparison to the Mallampalli laterites (47.9-48.7 wt. %; Table 1). Similar geochemical attributes are reported by Bhaskar and Tiwari (2017) for AP laterites from the above localities.

Laterites, which are reddish-brown coloured, are characterized by a definite ratio of SiO_2:R_2O_3 and subjected to toughening up on exposure to alternate wetting and drying. These are the products of strong tropical weathering made up of mineral assemblages that may include iron or aluminium oxides, oxyhydroxides or hydroxides, kaolinite and quartz, (Alexander and Cady, 1962; Maignien, 1966; McFarlane, 1976; Tardy, 1992; Bland and Rolls, 1998). Laterites with Fe_2O_3:Al_2O_3 ratio more than one and SiO_2:Fe_2O_3 ratio less than 1.33 is termed as ferruginous laterite, while that having Fe_2O_3:Al_2O_3 ratio less than one and SiO_2:Al_2O_3 ratio less than 1.33 is termed as aluminous laterite. The Mallampali laterite, enriched in Fe_2O_3 (22-25.24 wt. %) content and depleted in Al_2O_3 (13-13.31 wt.%), can be categorized under ferruginous laterite, while the AP laterites, are enriched in Al_2O_3 (14-22.30 wt.%) content and depleted in Fe_2O_3 (10-13.42 wt.%) content, which elucidated them to be aluminous laterites.

The Mallampalli laterites fall on the Kaolinization field and the AP laterites fall on the basalt field in the trilinear discrimination diagram (SiO_2-Fe_2O_3-Al_2O_3) (Schellmann, 1981), as shown in Figure 4. Similarly, in the variation diagram, the Mallampalli and AP laterites show negative correlation between Fe_2O_3 and SiO_2, while Fe_2O_3 have positive correlation with Al_2O_3 and TiO_2 (Figure 5).

It is well known that the laterites are the products of chemical weathering and their mineralogy and geochemical characters are controlled by such processes. The Chemical Index of Alteration (CIA; Nesbitt and Young, 1982) is able to measure the degree of decomposition and desilicification during the process of weathering. The Chemical Index of Alteration (CIA) can be calculated by the formula

$$CIA = Al_2O_3 / (Al_2O_3 + CaO + Na_2O + K_2O) \times 100$$

The values of CIA from AP is ranging from 76 to 89 and the values of CIA from Mallampalli laterite, range from 85 to 88, which elucidate that the laterites are subjected to high rates of weathering with severe losses of bases and are further subjected to kaolinisation after removal / modification of parent rock geochemistry. The CIA values are plotted against the major oxides (SiO_2, Al_2O_3, CaO, Na_2O and K_2O) (Figure 6), in which the Mallampalli laterites are negatively correlated except Fe_2O_3 which is

Table 1. Major elemental concentration averages for Mallampalli (Telangana) and Andhra Pradesh laterites

Sample No.	Al	VP	VC	SP	K	N	MP-1	MP-2
SiO_2	73.73	69.54	60.07	62.13	65.40	66.65	48.76	47.97
TiO_2	-	-	-	-	-	-	2.21	2.93
Al_2O_3	14.07	16.68	22.30	18.30	19.45	15.27	13.24	13.31
Fe_2O_3	10.25	11.90	13.42	13.25	12.50	12.38	22.14	25.24
MnO	0.04	0.03	0.04	0.05	0.06	0.02	0.54	0.22
MgO	0.61	0.63	0.40	0.34	0.58	0.41	0.17	0.12
CaO	0.42	0.57	0.45	0.33	0.36	0.24	0.78	0.65
Na_2O	1.19	0.68	3.46	2.58	2.78	0.67	0.37	0.34
K_2O	0.41	0.04	0.24	0.23	0.15	0.21	0.28	0.06
P_2O_5	-	-	-	-	-	-	0.15	0.08
LoI	-	-	-	-	-	-	11.44	8.37
Sum	100.71	100.07	100.39	97.22	101.27	95.83	100.05	99.30
R_2O_3	24.32	28.58	35.72	31.55	31.95	27.64	35.38	38.55
SiO_2/Fe_2O_3	7.19	5.84	4.48	4.69	5.23	5.39	2.20	1.90
Fe_2O_3/Al_2O_3	0.73	0.71	0.60	0.72	0.64	0.81	1.67	1.90
SiO_2/R_2O_3	3.03	2.43	1.68	1.97	2.05	2.41	1.38	1.24
CIW	83.84	88.55	77.38	79.06	78.84	90.84	87.70	87.25
CIA	81.12	88.34	76.68	78.21	78.32	89.65	85.11	88.00

R_2O_3 = (Al_2O_3 + Fe_2O_3); Al-Allimadugu, VP-Venkateswarapalem, VC-Venkatachalam, SP-Saidapuram, K-Kadivedu, N-Nellore of AP (Bhaskar and Tiwari, 2017). MP-1 and 2 belong to Mallampalli of Telangana (present study).

Figure 4. The Mallampalli laterite fall on the Kaolinization field and AP laterites fall on the basalt field in the Ternary diagram (SiO_2-Fe_2O_3-Al_2O_3) (Schellman, 1981).

positively correlated. On the other hand, AP laterites have negative correlations between Al_2O_3, Fe_2O_3, CaO, Na_2O and K_2O with CIA, but SiO_2 is positively correlated which reveals that the Mallampalli laterite is enriched in Fe content and depleted in other oxides, with progressive chemical alteration and in case of AP laterites, Si is increasing with simultaneous leaching of other elements with progressive chemical alteration.

The Chemical Index of Weathering (CIW) (Harnois and Moore, 1988) is calculated by following formula using molecular weight percentage

$$CIW = [Al_2O_3/(Al_2O_3 + CaO + Na_2O)] \times 100$$

The Values of CIW from AP is ranging from 78 to 91 and the Values of CIW from Mallampalli laterite ranging from 87 to 88, which are very similar to CIA values. Based on the obtained CIW values, it can be inferred that the

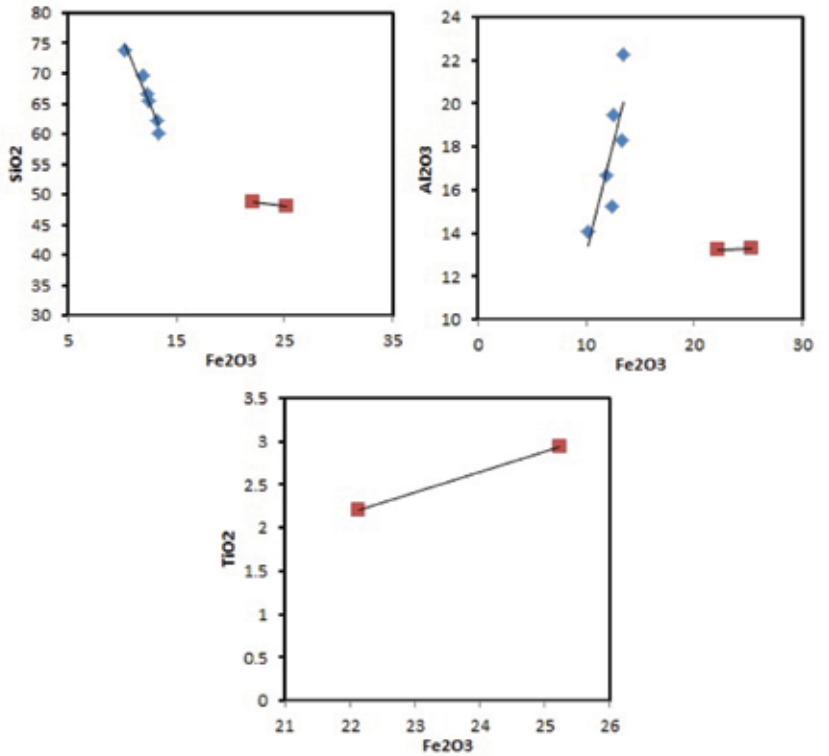

Figure 5. The variation diagram of Fe_2O_3 vs SiO_2, Al_2O_3 and TiO_2 for Mallampalli and AP Laterites.

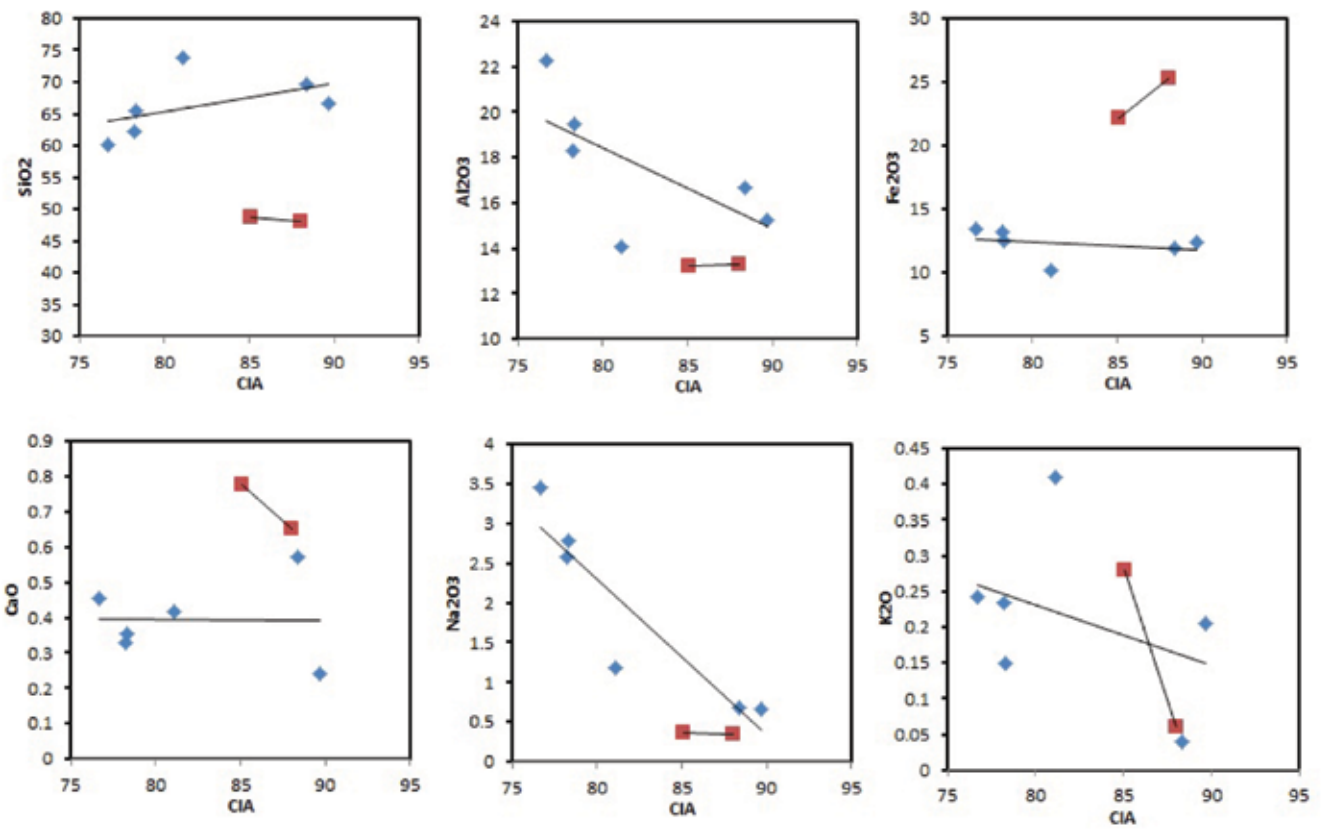

Figure 6. The CIA vs other major oxides variation diagram of Mallampalli and AP laterites.

Mallamapalli and AP laterites are subjected to intense weathering.

DISCUSSION AND CONCLUSIONS

Geochemically, the AP laterites are rich in Al_2O_3 content than Fe_2O_3 content, whereas the Mallamapalli laterites of Telangana, are enriched in Fe_2O_3 content and are depleted in Al_2O_3, clearly depicting their aluminous and ferruginous character respectively. The non-lateritic nature ($SiO_2/R_2O_3>2$) is recorded in case of AP laterites from Allimadugu, Venkateswarapalem, Kadivedu and Nellore but for localities Venkatachalam and Saidapuram of AP and Mallampalli, the SiO_2/R_2O_3 is less than 2, and reflect on their lateritic nature. CIA values exhibit that the Mallampalli laterite is enriched in Fe content and depleted in other oxides and in the AP laterites, Si is increasing due to leaching of other elements with increasing CIA. It is felt that the Mallampalli laterites are the product of Kaolinized ferruginous shale (bed rock), while the AP laterites are alteration products of the mafic protolith.

ACKNOWLEDGEMENT

NK is highly thankful to UGC-BSR fellowship and financial assistance to the work and also thankful to The Director, CSIR-NGRI for his kind approval to undertake geochemical studies. The authors are thankful to the anonymous reviewers for their constructive suggestions to upgrade the manuscript and Dr. O.P. Pandey, Scientist Emeritus for efficient editorial handling.

Compliance with Ethical Standards

The authors declare that they have no conflict of interest and adhere to copyright norms.

REFERENCES

Alexander, L.T. and Cady, J.G., 1962. Genesis and hardening of laterite in soils. U.S. Department of Agriculture, Technical Bull., 1281, 1-90.

Bhaskar, B.P. and Tiwari, G., 2017. Geochemical interpretations of laterite associated soils of east coast Andhra Pradesh. Chem. Sc. Rev. and Lett. 6(21), 187-197.

Bland, W. and Rolls, D., 1998. Weathering: An Introduction to the Scientific Principles. London: Arnold, 1-271.

Buchanan, F., 1807. A Journey from Madras Through the countries of Mysore, Kanara and Malabar (3 volumes). London: East India Co., 436-461.

Chadwick, B., Vasudev, V.N. and Hegde, G.V., 2000. The Dharwar craton, southern India, interpreted as the result of Late Archaean oblique convergence. Precamb. Res., 99, 91-111.

Chaudhuri, A. and Howard, J.D., 1985. Ramgundam Sandstone; a middle Proterozoic shoal-bar sequence. J. Sedimentary Res., 55(3), 392-397.

Chaudhuri, A.K., 2003. Stratigraphy and paleogeography of the Godavari Supergroup in the south-central Godavari valley, south India. J. Asian Earth Sci., 21, 595–611.

Chaudhuri, A.K., Saha, D., Deb, G.K., Patranabis-Deb, S., Mukherjee, M.K. and Ghosh, G., 2002. The Purana Basins of southern cratonic province of India – a case for Mesoproterozoic fossil rifts. Gond. Res., 5, 23–33.

Conrad, J.E., Hein, J.R., Chaudhuri, A.K., Patranabis-Deb, S., Mukhopadhyay, J., Deb, G.K. and Beukes, N.J., 2011. Constraints on the development of Proterozoic basins in central India from 40Ar/39Ar analysis of authigenic glauconitic minerals. GSA Bull., 123(1-2), 158-167.

Das, K., Yokoyama, K., Chakraborty, P.P. and Sarkar, A., 2009. Basal tuffs and contemporaneity of the Chattisgarh and Khariar basins based on new dates and geochemistry: J. Geology, 117, 88–102.

Harnois, L. and Moore, J.M., 1988. Geochemistry and origin of the Ore Chimney formation, a transported paleoregolith in the Grenville Province of southeastern Ontario, Canada. Chem. Geol., 69(3-4), 267-289.

Maignien, R., 1966. Review of research on Laterites. Paris: UNESCO, 1-148.

McFarlane, M.J., 1976. Laterite and landscape. London: Academic Press, 1-164.

Nesbitt, H.W. and Young, G.M., 1982. Early Proterozoic climates and plate motions inferred from major element chemistry of lutites. Nature, 299(5885), p.715.

Patranabis-Deb, S. and Chaudhuri, A.K., 2007. A retreating fan-delta system in the Neoproterozoic Chattisgarh rift basin, central India: Major controls on its evolution: American Association of Petroleum Geologists (AAPG) Bull., 91(6), 785–808.

Price, J.R. and Velbel, M.A., 2003. Chemical weathering indices applied to weathering profiles developed on heterogeneous felsic metamorphic parent rocks. Chem. Geol., 202(3-4), 397-416.

Raychaudhuri, S.P., 1980. The occurrence, distribution, classification and management of laterite and lateritic soils. Cahiers O.R.S.T.O.M., Série Pédologie, 18(3-4), 249-252.

Reddy, R.S., Naidu, L.G.K., Ramesh kumar, S.C., Budhilal, S.L. and Krishnan, P., 2005. Land Resources of Medak District, Andhra Pradesh, NBSS Publ. No. 791, NBSS and LUP, Nagpur.

Schellmann, W., 1981. Considerations on the definition and classification of laterites. In: Proceedings of the International Seminar on Lateritisation Processes, Trivandum, India, 1-10.

Tardy, Y., 1992. Diversity and terminology of laterite profiles. In: Martini, I.P., Chesworth, W., (eds). Weathering, soils and paleosols. Amsterdam: Elsevier, 379-405.

Received on: 29.1.19; Revised on: 8.3.19; Accepted on: 28.3.19

Errata

Tarun Solanki, S. P. Prizomwala and P. M. Solanki, 2018. Geomorphic Expressions of Active Strike-slip faulting (Girnar Fault), Saurashtra, Western India. J. Indian Geophys. Union, 22(4), 399-406.

In the above mention paper, the affiliation of the authors should have been as given below:

Geomorphic Expressions of Active Strike-slip faulting (Girnar Fault), Saurashtra, Western India

Tarun Solanki [1, 2*], S. P. Prizomwala[1], P. M. Solanki[3]

[1]Active Tectonics Group, Institute of Seismological Research, Gandhinagar, India 382009

[2] Research scholar, Gujarat University, Ahmedabad, 380009

[3]Department of Geology, M.G. Science Institute, Navrangpura, Ahmedabad 380009

* Corresponding Author: tarunsolanki86@yahoo.in

GUIDE FOR AUTHORS

The Journal of Indian Geophysical Union (J-IGU), published bimonthly by the Indian Geophysical Union (IGU), is an interdisciplinary journal from India that publishes high-quality research in earth sciences with special emphasis on the topics pertaining to the Indian subcontinent and the surrounding Indian Ocean region. The journal covers several scientific disciplines related to the Earth sciences such as solid Earth geophysics, geology and geochemistry, apart from marine, atmosphere, space and planetary sciences. J-IGU welcomes contributions under the following categories:

- Research papers and short notes reporting new findings.
- Review articles providing comprehensive overview of a significant research field.

In addition, J-IGU also welcomes short communications, after communications and report on scientific activity, book reviews, news and views, etc.

The manuscript should be submitted electronically as a single word format (.doc file) including the main text, figures, tables, and any other supplementary information along with the signed "Declaration Letter". The manuscript should be submitted by email (jigu1963@gmail.com) to the Chief Editor.

After acceptance of the manuscript the corresponding author would be required to submit all source files (text and Tables in word format) and figures in high resolution standard (*.jpg, *.tiff, *.bmp) format. These files may be submitted to J-IGU as a single *.zip file along with the "Copyright Transfer Statement".

IMPORTANT INFORMATION

Ethics in publishing
J-IGU is committed to ensuring ethics in publication and takes a serious view of plagiarism including self-plagiarism in manuscripts submitted to the journal. Authors are advised to ensure ethical values by submitting only their original work and due acknowledgement to the work of others used in the manuscript. Authors must also refrain from submitting the same manuscript to more than one journal concurrently, or publish the same piece of research work in more than one journal, which is unethical and unacceptable. Editor of J-IGU is committed to make every reasonable effort to investigate any allegations of plagiarism brought to his attention, as well as instances that come up during the peer review process and has full authority to retract any plagiarized publication from the journal and take appropriate action against such authors if it is proven that such a misconduct was intentional.

Similarly, Editor and Reviewers are also expected to follow ethical norms of publishing by ensuring that they don't use any unpublished information, communicated to them for editorial or review purpose, in their own research without the explicit written consent of the author. They are also expected to keep manuscript/ data/ observations/ any other information related to the peer review confidential to protect the interest of the authors. Reviewers should refrain from reviewing the manuscripts in which they have conflicts of interest resulting from competitive, collaborative, or other relationships or connections with any of the authors, companies, or institutions connected to the manuscript.

Conflict of interest
All authors are requested to disclose any actual or potential conflict of interest including any financial, personal or other relationships with other people or organizations within three years of beginning the submitted work that could inappropriately influence, or be perceived to influence, their work.

Submission declaration
Submission of a manuscript implies that the work has not been published previously and it is not under consideration for publication elsewhere, and that if accepted it will not be published elsewhere in the same or any other form, in English or in any other language, without the written consent of the publisher. It also implies that the authors have taken necessary approval from the competent authority of the institute/organization where the work was carried out.

Copyright
After acceptance of the manuscript the corresponding author would be required to sign and submit the "Copyright Transfer Statement".

MANUSCRIPT PREPARATION

The corresponding author should be identified (include E-mail address, Phone/Mobile number). Full affiliation and postal address must be given for all co-authors.

Abstract:
An abstract of not more than 300 words must be included.

Text:
The manuscript should be structured to include a front page containing the title, Author(s) name, affiliation and address of the institute, where the work was carried out, a short title, and 5-to-6 Key words. Author(s) present address, if different from the above mentioned address, may be given in the footnote. The corresponding author should be identified with an asterisk and his/her email ID should be provided. This page should be followed by the main text consisting of Abstract, Introduction, Methods/ Techniques/ Area description, Results, Discussion, Conclusions, Acknowledgements, and References. Tables and Figures with captions should be inserted at the end of main text. It should not be inserted in the body of the text.

Figures/ Illustrations:
All figures should be provided in camera-ready form, suitable for reproduction (which may include reduction) without retouching. Figures in high-resolution (at least 300 dpi) standard formats (*.jpg, *.tiff, *.bmp) are acceptable. Figures should be numbered according to their sequence in the text. References should be made in the text to each figure. Each figure should have a suitable caption.

Tables:
Authors should take note of the limitations set by the size and layout of the journal. Table should not exceed the printed area of the page. They should be typed on separate sheets and details about the tables should be given in the text. Heading should be brief. Large tables should be avoided and may be provided as supplementary information, if required.

Equations:
Equations should be numbered sequentially with Arabic numerals and cited in the text. Subscripts and Superscripts should be set off clearly. Equation writing software that presents each equation as an object in MS Word will be accepted. Style and convention adopted for the equations should be uniform throughout the paper.

References:
All references to publications cited in the main text should be presented as a list of references in order following the text and all references in the list must be cited in the text. References should be arranged chronologically, in the text. The list of references should be arranged alphabetically at the end of the paper.

References should be given in the following form:
Kaila, K.L., Reddy P.R., Mall D.M., Venkateswarlu, N., Krishna V.G. and Prasad, A.S.S.S.R.S., 1992. Crustal structure of the west Bengal Basin from deep seismic sounding investigations. Geophys. J. Int., 111,45-66.

REVIEW PROCESS:

All manuscripts submitted to the journal are peer-reviewed. It is advisable to send the contact details of 4 potential reviewers along with the manuscript to expedite the review process. Editor has the option to select reviewers from the list or choose different reviewers. The review process usually takes about 3 months. All enquiries regarding the manuscript may be addressed to the Editor.

GALLEY PROOF:

Technical editing of manuscripts is performed by the editorial board. The author is asked to check the galley proof for typographical errors and to answer queries from the editor. Authors are requested to return the corrected proof within two days of its receipt to ensure uninterrupted processing. The editor will not accept new material in proof unless permission from the editorial board has been obtained for the addition of a "note added in proof". Authors are liable for the cost of excessive alterations to galley proof.

PUBLICATION CHARGES:

There are no page charges for publication and printing charges for b/w figures. However, in view of substantial cost involved in printing of color figures, author will be charged for printing of pages containing color figures @ Rs. 2,500/- per page. The charges may be revised at any time based on cost of printing and production. Author will receive an estimate/ invoice of the color figures reproduction cost along with the galley proof. It is the responsibility of the author to remit the color figures reproduction cost within one month of the receipt of the estimate/invoice.

The corresponding author will receive a soft copy (pdf format) of his/her published article. Should the author desire to purchase reprints of his/her publication, he/she must send the duly signed Reprint Order Form (accompanies the galley proof and contains price details) along with the corrected galley proof to the Editor. The reprint charges must be paid within one month of sending the Reprint Order Form.

Any payment related to printing of color figures and/or purchase of reprints should be made in the form of a Demand Draft in the name of Treasurer, Indian Geophysical Union, payable at Hyderabad.

You may download the pdf file from: http://www.j-igu.in/IGU-Guide-forAuthors.pdf